T.C.

AKDENİZ ÜNİVERSİTESİ

DETECTION OF WATER CONTAMINATION IN FUEL TANKS USING FMCW RADARS

Mohamed Sayed Abdelkhalek AFIFI

INSTITUTE OF SCIENCE

COMPUTER ENGINEERING DEPARTMENT

PhD THESIS

DECEMBER 2025

ANTALYA

T.C.

AKDENİZ ÜNİVERSİTESİ

DETECTION OF WATER CONTAMINATION IN FUEL TANKS USING FMCW RADARS

MOHAMED SAYED ABDELKHALEK AFIFI

GRADUATE SCHOOL OF NATURAL AND APPLIED SCIENCES

COMPUTER ENGINEERING DEPARTMENT

PhD THESIS

DECEMBER 2025

ANTALYA

T.C.

AKDENİZ ÜNİVERSİTESİ

FEN BİLİMLERİ ENSTİTÜSÜ

DETECTION OF WATER CONTAMINATION IN FUEL TANKS USING FMCW RADARS

MOHAMED SAYED ABDELKHALEK AFIFI

INSTITUTE OF SCIENCE

COMPUTER ENGINEERING DEPARTMENT

PhD THESIS

DECEMBER 2025

ANTALYA

T.C.

AKDENİZ ÜNİVERSİTESİ

FEN BİLİMLERİ ENSTİTÜSÜ

DETECTION OF WATER CONTAMINATION IN FUEL TANKS USING FMCW RADARS

MOHAMED SAYED ABDELKHALEK AFIFI

GRADUATE SCHOOL OF NATURAL AND APPLIED SCIENCES

DEPARTMENT OF COMPUTER ENGINEERING

PhD THESIS

This thesis was accepted unanimously by the jury on 05/12/2025.

Prof. Dr. Selçuk HELHEL

Prof. Dr. Melih GÜNAY

Assoc. Prof. Dr. Abdullah GENÇ

Prof. Dr. Ümit Deniz ULUŞAR

Assoc. Prof. Dr. İbrahim Bahadır BAŞYİĞİT

ÖZET

AKARYAKIT TANKLARINDAKİ SU KİRLİLİĞİNİN FMCW RADARLARI KULLANILARAK TESPİTİ

MOHAMED SAYED ABDELKHALEK AFIFI

Doktora Tezi

Fen Bilimleri Enstitüsü
Bilgisayar Mühendisliği Anabilim Dali

Danışman: Prof. Dr. Selçuk HELHEL

Aralik 2025, 137 Sayfa

Dizel yakıt depolarındaki su kirliliği otomotiv, denizcilik ve sanayi sektörlerinde önemli operasyonel ve ekonomik zorluklara yol açmaktadır. Yoğuşma, sızıntı veya yakıt higroskopikliğinden kaynaklanan su varlığı mikrobiyal büyümeye, korozyona ve motor hasarına yol açar. Bakteriler ve mantarlar tarafından kolaylaştırılan mikrobiyal kontaminasyon, filtreleri tıkayan ve yakıt kalitesini düşüren biyofilmler üretir. Ayrıca dizeldeki sülfür bileşikleri suyla reaksiyona girerek aşındırıcı sülfürik asit oluşturur ve tankın bozulmasını hızlandırırken, yüksek basınçlı yakıt sistemlerindeki su damlacıkları enjektörlere zarar verir. Görsel denetimler, kimyasal test şeritleri ve kapasitif sensörler gibi geleneksel tespit yöntemlerinin gerçek zamanlı ve doğru izleme için yetersiz olduğu kanıtlanmıştır.

Geleneksel yöntemlerin sınırlamaları, sağlam bir alternatif olarak Frekans Modülasyonlu Sürekli Dalga (FMCW) radarına olan ilgiyi artırmıştır. FMCW radarı, doğrusal frekans modülasyonlu bir chirp göndererek ve dizel seviyesindeki kirleticilerin mesafesini belirlemek için yansıyan sinyali analiz ederek çalışır. FMCW teknolojisindeki son gelişmeler, gerçek dünyadaki karmaşıklıkların üstesinden gelmek için sinyal işlemeyi geliştirmeye odaklanmıştır. Bu çalışmada ele alınması gereken zorluk, doğru bir 2 seviyeli sıvı tespiti uygulamaktır (hem dizel hem de suda bulunan aşağıdaki kirleticilerin seviyesini tespit etmek).

ANAHTAR KELİMELER: Dizel Yakıt Tankları, FMCW Radar, Su Kirliliği, Sıvı Seviye Ölçümleri.

JÜRİ:

Prof. Dr. Selçuk HELHEL

Prof. Dr. Melih GÜNAY

Doç. Dr. Abdullah GENÇ

Prof. Dr. Ümit Deniz ULUŞAR

Doç. Dr. İbrahim Bahadır BAŞYİĞİT

ABSTRACT

DETECTION OF WATER CONTAMINATION IN FUEL TANKS USING FMCW RADARS

MOHAMED SAYED ABDELKHALEK AFIFI

PhD Thesis in

INSTITUTE OF SCIENCE
COMPUTER ENGINEERING DEPARTMENT

SUPERVISOR: PROF. DR. SELÇUK HELHEL

December 2025, 137 Pages

Water contamination in diesel fuel tanks poses significant operational and economic challenges across automotive, marine, and industrial sectors. The presence of water, whether from condensation, leaks, or fuel hygroscopicity, leads to microbial growth, corrosion, and engine damage. Microbial contamination, facilitated by bacteria and fungi, produces biofilms that clog filters and degrade fuel quality. Additionally, sulfur compounds in diesel react with water to form corrosive sulfuric acid, accelerating tank degradation, while water droplets in high-pressure fuel systems cause injectors. Traditional detection methods, such as visual inspections, chemical test strips, and capacitive sensors, have proven inadequate for real-time, accurate monitoring.

The limitations of conventional methods have spurred interest in Frequency-Modulated Continuous-Wave (FMCW) radar as a robust alternative. FMCW radar operates by transmitting a linear frequency-modulated chirp and analyzing the reflected signal to determine the distance of the diesel level contaminants. Recent advancements in FMCW technology have focused on improving signal processing to handle real-world complexities. The challenge to be addressed by this study is to implement an accurate 2-level liquid detection (detection the level of both the diesel and the below contaminations contained in water)

KEYWORDS: Diesel Fuel Tanks, FMCW Radar, Liquid Level Measurements, Water Contamination.

COMMITTEE:

Prof. Dr. Selçuk HELHEL

Prof. Dr. Melih GÜNAY

Assoc. Prof. Dr. Abdullah GENÇ

Prof. Dr. Ümit Deniz ULUŞAR

Assoc. Prof. Dr. İbrahim Bahadır BAŞYİĞİT

PREFACE

I want to thank the people who helped to make this research possible.

First, my advisors, Prof. Dr. Selçuk HELHEL, Prof. Dr. Melih GÜNAY, Doç. Dr. Abdullah GENÇ, for guiding me and pushing me to think critically.

Thanks also to the facilities in EMUMAM for providing the tools and space to run experiments.

I'm grateful to the support of my teaching staff especially Dr. Atalay KOCAKUCAK, classmates and colleagues for their feedback and support, as well as to the researchers whose earlier work laid the foundation for this project Also great thanks for the members who contributed to preparing the measurements Eng. Khaled Osman, Ercan MENGUC, Emin SAPMAZ, and Umut YILDIZ. Most importantly, thanks my family, my wife and friends including Mahmud HACIZADE for their encouragement and patience during this lengthy process.

This thesis is just one step in solving the problem of water contamination in fuel. There is still more work to be done, like improving the system for different types of fuel or making it cheaper for widespread use. I hope this research helps others continue exploring better ways to keep fuel clean and engines running smoothly.

MOHAMED SAYED ABDELKHALEK AFIFI
DECEMBER 2025

TABLE OF CONTENT

ACADEMIC DECLARATION

I state that this study titled "Detection of Water Contamination in Fuel Tanks Using FMCW Radars", which I submitted as a doctoral thesis, was written in accordance with academic rules and ethical values, and I declared that I have shown the source of all information that does not belong to me in this thesis.

05/12/2025

MOHAMED SAYED ABDELKHALEK AFIFI

SYMBOLS AND ABBREVIATIONS

Symbols

A	: Attenuation Constant (Lossy Media)
B	: Phase Constant / Wave Number
B	: Chirp Bandwidth (FMCW)
C_0	: Velocity of Light in Free Space
D	: Layer Thickness (Multi-Layer Models)
dB, dBi, dBm	: Logarithmic Units (Gain and Power)
$\Delta\varphi$ (or $\Delta\emptyset$)	: Phase Difference / Noise Term in IF Signal
E, H	: Electric and Magnetic Field Vectors (General)
f	: Frequency (General)
f_b	: Beat Frequency (FMCW)
f_c	: Carrier Frequency (FMCW)
GHz	: Giga (10^9) Hertz
Γ, T	: Reflection and Transmission Coefficients at Interfaces
Hz	: Hertz (1/Second)
λ_0	: Wavelength in Free Space
mm	: Millimeter
MHz	: Mega (10^6) Hertz
R(t)	: Range (Time-Dependent) In FMCW Derivation
$\bar{S}$	: Time-Averaged Poynting Vector (Power Density)
S_{11}, S_{21}	: S-Parameters: Input Reflection & Forward Transmission
tan δ	: Dielectric Loss Tangent
τ	: Time Delay (FMCW)
T	: Chirp Time / Sweep Duration (FMCW)
θ_i, θ_r, θ_t	: Angles of Incidence, Reflection, Transmission

θ_B	: Brewster Angle (Parallel Polarization)
θ_c	: Critical Angle for Total Internal Reflection
v_p	: Phase Velocity
$\omega = 2\pi f$	: Angular Frequency
Z_v or Z_w	: (Wave) Intrinsic Impedance of The Medium
ε_0	: Permittivity of Free Space
ε'	: Real Part of Permittivity (Energy Storage)
ε''	: Loss Factor (Dissipation)
ε_r	: Relative Permittivity (Dielectric Constant)
$\eta_0 \approx 377\ \Omega$	: Intrinsic Impedance of Free Space
η_c	: Intrinsic Impedance in Lossy Medium
μ	: Permeability (Generic)
μ_0	: Permeability of Free Space
σ	: Electrical Conductivity
$\gamma = \alpha + j\beta$	: Complex Propagation Constant (Lossy Media)

Abbreviations

ADC	: Analog-To-Digital Converter
AFE	: Analog Front End
ATEX / Ex-Proof / IS	: Intrinsic Safety/Explosion-Proof
CFAR	: Constant False Alarm Rate
MLCT	: Classification Technique in Machine Learning
DAC	: Digital-To-Analog Converter
DEM	: Digital Elevation Model
DOA	: Direction Of Arrival
DSP	: Digital Signal Processing
ECUAV	: Energy Conversion From Underwater Acoustic to Vibration
FFT	: Fast Fourier Transform
FMCW	: Frequency Modulated Continuous Wave
GFFT	: Golden-Section-Based FFT
IAA	: Iterative Adaptive Approach
ISAR	: Inverse SAR
LHCP	: Left-Hand Circular Polarization
LNA	: Low-Noise Amplifier
MIMO	: Multiple-Input Multiple-Output
ML	: Machine Learning
MM-wave	: Millimeter-Wave
MW	: Microwave
NB-IoT	: Narrowband Internet Of Things
OSCA-CFAR	: Ordered-Statistics CA-CFAR
PA	: Power Amplifier
PCB	: Printed Circuit Board

PLL	: Phase-Locked Loop
MLRT	: Regression Technique in Machine Learning
RF	: Radio Frequency
RHCP	: Right-Hand Circular Polarization
RMA	: Range Migration Algorithm
SAR	: Synthetic Aperture Radar
SDR	: Software-Defined Radio
SFCC	: Swept-Frequency Cross-Correlation
SNR	: Signal-To-Noise Ratio
TEM	: Transverse Electromagnetic
UAV	: Unmanned Aerial Vehicle
USRP	: Universal Software Radio Peripheral
VCO	: Voltage Controlled Oscillator
VNA	: Vector Network Analyzer

LIST OF FIGURES

1 INTRODUCTION

1.1 Problem Statement

Water contamination in diesel fuel tanks is a common but serious problem. It can damage engines, cause rust, and lead to costly repairs. Many current methods to detect water in fuel are either unreliable or too expensive for everyday use. This thesis explores a new way to solve this problem using radar technology—specifically **FMCW radar**, which can accurately detect water without touching the fuel.

Old school types start to be contaminated when transported from the refinery and stored over a period of time, during this period temperature humidity and other effects will lead to the contamination. Water content sands and sediments start to accumulate at the bottom of the tank with microorganisms and particles also suspended water particles are formed in full volume. Over a long time both the color and the quality of the fuel start to decline and finally it can lead 2 clogging of the injector of the systems including cars airplanes diesel generators power plant burners, etc.…

In **Figure 1.1**, (Fueltec, 2015)It is clearly illustrated using standard real diesel station tank, there is a cross section that has been made to the tank, and it is indicated that the tank include several layers of different materials starting from air and condensates which include some air and fuel vapor, below the fuel vapor and air layer there is the liquid fuel layer and below this liquid fuel layer there is a layer of water that is mixed with some bacteria and fungi, and finally in the bottom the most dense material which are sludge, sands, other sediments and rocks residuals.

This project started with a simple idea: *Can we use radar, like the kind in cars or airplanes, to find water in diesel tanks?* Over time, we learned how radar signals interact with fuel and water, tested different approaches, and worked to make the system practical for real-world use. Along the way, I faced challenges like precision, exact values of material properties. The result is a method that could help industries monitor fuel quality more effectively and prevent damage caused by water contamination.

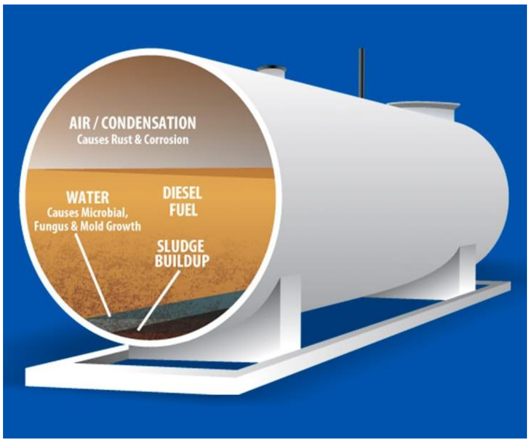

Figure 1.1. Internal content of a real Diesel Station Tank

Considering the dangers , failures and loss mentioned above, food storage facilities owners used to apply several techniques in order to avoid the impact of that contamination, and the first step to avoid this is to take a sample that represent the content of the fuel in an accurate and comprehensive way, something has different techniques which is out of the scope of this study, however in **Figure 1.2** (Fueltec), This sample is represented and it include agreed with different material that can be visually detected in the figure and sort it based on their density starting from sands and sludge on the bottom of the sampling glass, then a layer of dead bacteria and fungus which is covered by a layer of water which act as a medium for the still living bacteria and fungus and in the top of this layer the living bacteria and fungus already there hanging between the interface between the water and the diesel fuel, and above that all the least dense fluid which is the diesel.

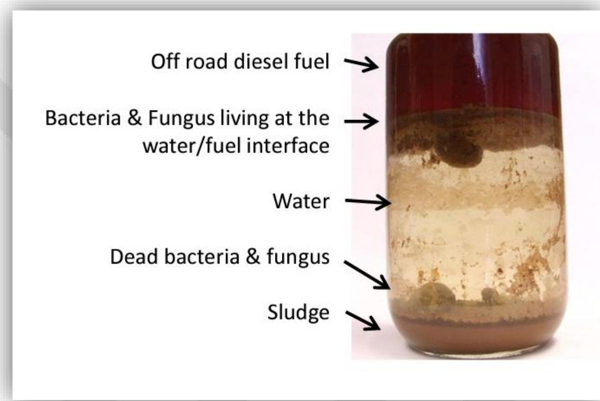

Figure 1.2. Focus on the sample taken from Diesel Tanks

In **Figure 1.3** (Fueltec), the contrast between be clean and the contaminated fuel filter located inside the running vehicles is illustrating how the filtration mission is the hardest when the fuel is contaminated as water is different than the fuel in density and the content it affects the pores of the filter, And also the sludge sand and rock residuals block these pores and accordingly the filter expected lifetime significantly drops which lead to reduced efficiency and unexpected malfunction of the vehicle which could lead to different types of losses.

Figure 1.3. Effect of water contamination on motor spare parts

By looking to the **Figure 1.4** (Fueltec), Which demonstrates the fuel tank diagram inside the car in the above part of the diagram it's clearly shown that the fuel tank consist of a compartment that can include the fuel on the top left there is air refreshing tube, and also fuel level sensors, Mostly the fuel is mechanically measured using a bowl that has less density than the fuel and once the fuel level change it changed its height and accordingly the fuel level sensor can indicate on the dashboard the amount of fuel in the tank, on the top right there is a filler neck, on the bottom right there is a filter and in the bottom of the tank there is a drain. The location of the drain is a double edge on the fuel tank it helps to absorb the fuel inside the tank to the least amount remaining so it can ensure that the car has the most range and mileage possible, however this configuration leads to putting the engine and the other car part in the close interface with all the contaminants that resides in the fuel tank bottom including sand residuals, rock sediments, and also the higher dense liquid which is water.

The understanding how the combustion engine is working provide us more clarity about the danger that could took place once we push water to the combustion chamber , during the combustion process, the engine Pistons changes reciprocally their places between the top dead center and the bottom dead center, which means that inside this combustion chamber there must be a compressible fluid, in normal cases these compressible fluid is a vapor of diesel and air. Bushing water directly to the internal combustion engine the engine in the highest risk possible, because instead of compressing a compressible fluid, the piston must compress an incompressible fluid which is water which will lead to the breaking of the motor.

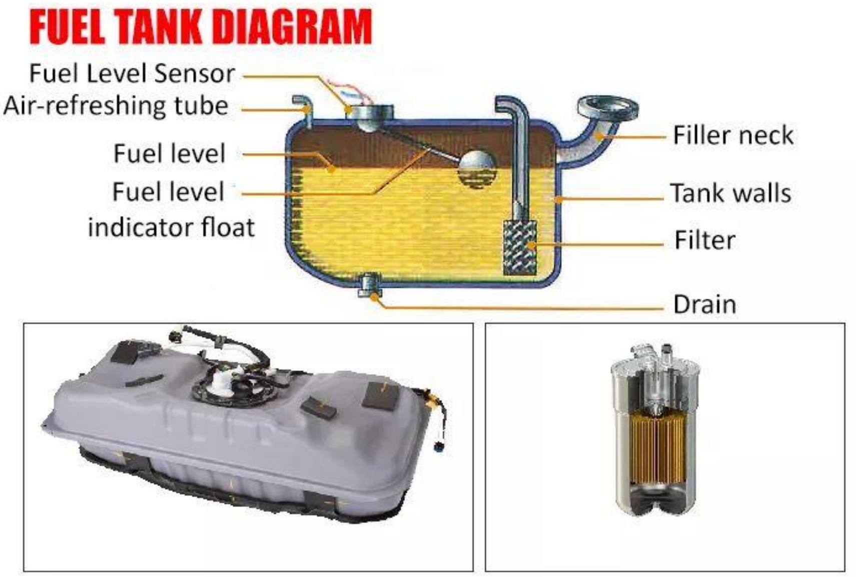

Figure 1.4. Fuel Tank Diagram

2 REFERENCE REVIEW

There are several studies presented in evaluating FMCW radar sensing for similar approaches. Researchers have explored various applications of radar technology in this field, summary about these researches are as follows:

The research conducted by Mun et al (2021) explores the design and application of an 80 GHz Frequency Modulated Continuous Wave (FMCW) radar for the precise measurement of cryogenic fluid levels, with a focus on liquid nitrogen and implications for liquid hydrogen applications. As hydrogen-based energy systems gain traction in fields such as unmanned aerial vehicles (UAVs) and hydrogen fuel cell vehicles, the need for accurate residual fuel monitoring in storage and transport tanks has become critical. Conventional measurement techniques—capacitive, float-type, or pressure-based—struggle under cryogenic conditions due to mechanical difficulties, sensitivity to condensation, and difficulty in dealing with vapor interference. The radar system in this study utilizes FMCW principles to overcome these limitations. FMCW radars operate by transmitting a frequency-modulated signal and capturing the beat frequency generated upon reflection, which is proportional to the target distance. However, for cryogenic media like liquid nitrogen (LN2) and liquid hydrogen (LH2), the minimal impedance contrast between vapor and liquid phases results in poor signal reflection, complicating interface detection. To solve this, the researchers implemented a zoom Fast Fourier Transform (FFT) signal processing technique, enhancing range resolution from 37.5 mm to 5 mm. Performance testing was conducted using three media: metal (STS 304), water, and liquid nitrogen. The metallic surface provided a total reflection reference. Water, with its high relative permittivity ($\varepsilon r \approx 80$), exhibited a stronger signal return and a resolution of 5.5 mm. In contrast, liquid nitrogen, chosen as a proxy for the more hazardous liquid hydrogen, presented challenges due to low dielectric constants and bubble formation during boiling. To mitigate these issues, the radar algorithm was refined to identify and distinguish multiple targets: the bottom of the vessel, the liquid-gas interface, and the upper tank flange. By extracting and analyzing the top three frequency peaks using zoom FFT, the algorithm selected the intermediate peak as the most probable liquid interface. This method improved level detection accuracy in dynamic conditions, such as during tank filling and draining. In conclusion, the study confirms the viability of 80 GHz FMCW radar technology for cryogenic applications, offering significant advantages over traditional sensors in terms of precision, safety, and adaptability. While challenges remain—particularly regarding signal stability in boiling liquids—the radar's performance indicates its strong potential for deployment in cryogenic fuel storage systems, especially for hydrogen applications, given the physical similarity between LN2 and LH2.

The study by J. Zhang & Bai (2011) presents a virtual instrument-based FMCW radar system for high-precision liquid level measurement, achieving <5mm error through innovative signal processing. Using a 26GHz homodyne radar with 1500MHz bandwidth Voltage Controlled Oscillator (VCO), the system features a PCI-16E data acquisition card (1.25MHz sampling rate) to capture intermediate frequency signals from tank reflections. Experimental validation showed the system's effectiveness for marine tank applications, with advantages in anti-interference performance. The graphical programming environment enabled flexible testing of different window functions and real-time parameter adjustments. Funded by Hebei Province science foundations, this work demonstrates how virtual instrumentation can enhance FMCW radar systems when combined with advanced spectral correction techniques, offering a template for industrial level measurement applications requiring millimeter-scale precision.

Menguc et al. (2025) proposed a non-destructive testing (NDT) method using Frequency Modulated Continuous Wave (FMCW) radar for corrosion mapping on metal surfaces. The study utilized S-band FMCW radar with dual helical antennas to collect phase shift data that reflected surface corrosion variations. Unlike traditional range or velocity measurement applications, this approach focused on extracting phase shift patterns to reconstruct corrosion images through advanced signal and image processing techniques.

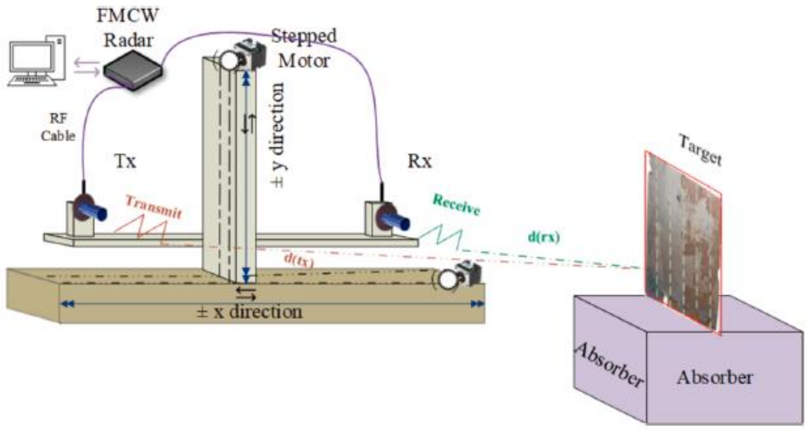

Figure 2.1 Schematic diagram of measurement system

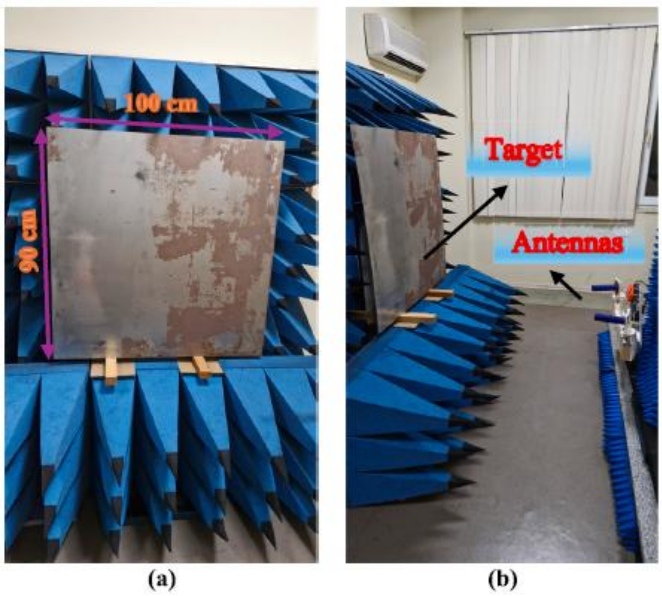

Figure 2.2. Data collection: (a) Corroded metal plate, (b) Antennas and metal plate

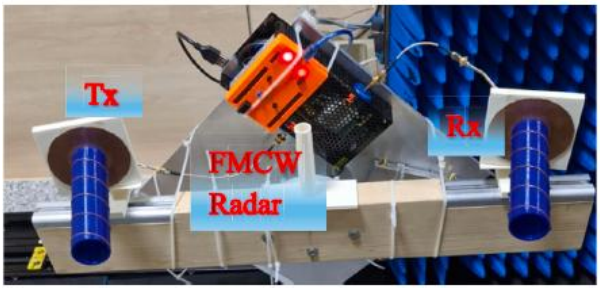

Figure 2.3. Helix antennas and FMCW radar

The imaging algorithm involved several key steps: data preprocessing, grayscale conversion, morphological dilation, adaptive windowing, and bilateral filtering to enhance edge detection and target separation. The study shares deep methodological parallels with the proposed FMCW radar approach for detecting water contamination in diesel tanks, particularly in its use of electromagnetic wave reflection analysis and S-parameter interpretation to characterize material and structural variations. Both investigations employ Frequency-Modulated Continuous Wave (FMCW) radar as a non-destructive testing (NDT) technique, where phase and amplitude changes in the reflected signal reveal critical information about the target medium's physical or dielectric properties. The study concluded that FMCW radar offers a compact, low-power, and cost-effective solution for corrosion detection, capable of distinguishing corroded from non-corroded regions. Future work aims to apply machine learning to enhance detection accuracy and extend the technique to embedded corrosion mapping within concrete structures.

The paper titled "Determination of Olive Oil Purity by S Parameter" by Irmak et al. (2025) presents a non-destructive electromagnetic method to assess the purity of olive oil through S-parameter analysis in the microwave frequency range. The authors emphasize the limitations of traditional chemical methods, which are time-consuming, costly, and require sample preparation, proposing instead a fast and contactless microwave measurement technique. The study employs a Vector Network Analyzer (VNA) and a specially designed coaxial probe setup to measure reflection and transmission coefficients (S_{11} and S_{21}) of olive oil samples at various levels of adulteration with sunflower oil. The frequency range analyzed spans 1 to 10 GHz, a band selected to capture dielectric variations linked to compositional changes. Measurements were performed at controlled temperature and sample volume to ensure repeatability. The electromagnetic interaction between microwaves and oil samples is interpreted in terms of dielectric constant and loss tangent, which directly influence the measured S-parameters.

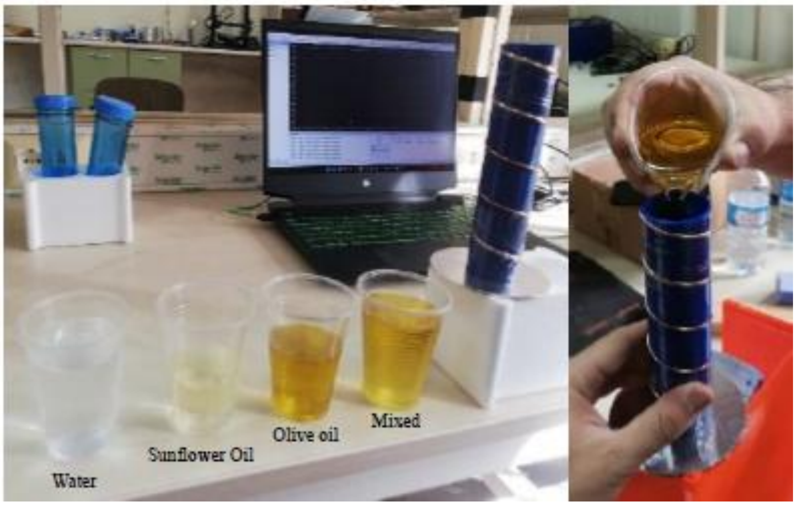

Figure 2.4. Measurement Setup

Results indicate a clear correlation between S-parameter shifts and oil purity levels. Specifically, adulteration with sunflower oil increases the dielectric constant and loss factor, leading to higher reflection (S_{11}) and reduced transmission (S_{21}) magnitudes. By applying polynomial regression and statistical curve fitting, the authors successfully establish a model capable of predicting purity percentage from S-parameter data with a correlation coefficient exceeding 0.95. This paper aligns closely with the underlying principles of FMCW radar-based liquid contamination detection, as both rely on electromagnetic wave interactions with layered or mixed dielectric media. In the olive oil study, the purity level affects the dielectric constant, which in turn alters the reflection (S_{11}) and transmission (S_{21}) parameters — analogous to how water contamination in diesel fuel alters reflection coefficients and phase responses in radar signals. Both systems exploit dielectric contrasts to infer composition changes. While the study uses microwave S-parameter characterization through a VNA rather than a radar front end, the physical principles of electromagnetic reflection, attenuation, and phase shift are identical. The frequency range (1–10 GHz) overlaps with S- and X-band radar frequencies, reinforcing that dielectric sensing in this spectrum is effective for detecting subtle compositional variations. The research thus provides strong experimental support for the FMCW-based approach proposed in our thesis, validating that dielectric-based signal variations can be used to detect and quantify contamination levels in liquid media. This study further underscores the value of non-destructive testing (NDT) using microwave techniques, strengthening the interdisciplinary foundation between food quality assurance and industrial fuel monitoring. Its regression-based interpretation of S-parameter data could also inspire the application of machine learning algorithms in radar signal analysis to improve contamination classification accuracy in diesel-water detection systems. The study's conclusions emphasize that S-parameter-based analysis provides a reliable, rapid, and repeatable method for quality control of edible oils, with potential industrial applications in automated purity monitoring systems. Moreover, since the method is entirely non-invasive and can be extended to other liquid mixtures, it demonstrates high potential for broader use in the food industry and chemical sensing applications.

The paper titled "The Design of FMCW Radar Liquid Level Measuring System Based on FPGA" Zhao Zeng-rong & Qiu Yao-hui (2014) presents a high-precision digital frequency-modulated continuous-wave (FMCW) radar system for liquid level measurement in industrial applications, particularly in the oil industry. The system comprises a K-band radar transceiver (IVS-148) with a voltage-controlled oscillator (VCO), an FPGA chip for signal processing, and A/D and D/A converters. The FPGA is employed to generate modulation signals and process radar data, leveraging its high integration, real-time processing capabilities, and flexibility to improve measurement accuracy and system performance. The FMCW radar emits a sawtooth-modulated signal, and the reflected signal from the liquid surface is mixed with the transmitted signal to produce a beat frequency, which is linearly related to the distance (liquid level). The system utilizes FFT (Fast Fourier Transform) implemented via an IP core in the FPGA to estimate the beat frequency, with additional measures such as high-pass filtering, Hanning windowing, and ping-pong RAM buffering to enhance precision and reduce noise. Key design considerations include filter circuit optimization, impedance matching, and careful gain settings to avoid signal distortion. Experimental results demonstrate the system's suitability for high-accuracy liquid level measurement, with advantages such as low power consumption, strong anti-interference capability, and adaptability to industrial environments. The authors conclude that the FPGA-based FMCW radar system offers significant potential for applications in tank and oil storage monitoring due to its reliability, scalability, and precision.

The paper titled "A Low-Power High-Accuracy Urban Waterlogging Depth Sensor Based on Millimeter-Wave FMCW Radar" Shui et al. (2022) presents a novel system for real-time urban waterlogging monitoring using a 77 GHz frequency-modulated continuous-wave (FMCW) radar. The system addresses the limitations of traditional water depth measurement methods—such as susceptibility to environmental interference—by leveraging mmWave radar technology, which is robust against poor visibility, temperature variations, and other harsh conditions. A key innovation is the proposed Swept Frequency-Cross Correlation (SFCC) algorithm, which significantly enhances distance resolution (reducing measurement error from 4.5 cm to <5 mm) and lowers computational complexity from O(n·log n) to O(n) compared to conventional FFT-based methods. The system integrates edge computing to process data locally, reducing reliance on cloud computing and bandwidth usage. It includes a humidity sensor and an event-driven scheme to dynamically adjust sampling frequency based on environmental conditions, achieving >100× power savings by switching between standby and active modes. A prototype was developed using Texas Instruments' IWR1443Boost radar module, a processor module, and an NB-IoT communication module, demonstrating real-time water depth monitoring with high accuracy (mean error <5 mm) and low cost. The system's advantages include wide detection range, low power consumption, small form factor, and suitability for IoT deployment in urban flood prevention.

The paper titled "River Surface Analysis and Characterization Using FMCW Radar" Mutschler et al. (2022) explores the application of frequency-modulated continuous-wave (FMCW) radar for non-contact monitoring of river surfaces, aiming to enhance flood and drought warning systems. The study utilizes a commercially available 76–81 GHz FMCW radar to measure water surface velocity and level, leveraging chirp sequence modulation and 2D fast Fourier transform (2D-FFT) processing to generate range-Doppler maps. A key innovation is the introduction of an envelope velocity distribution analysis, which extracts features such as maximum mean velocity and peak width to characterize river flow behavior. The methodology includes zero-velocity blanking and constant false alarm rate (CFAR) filtering to reduce noise, followed by time-averaging of envelope velocities to identify reflection centers and distinguish between turbulent and smooth flows. Experiments on four rivers in Southern Germany demonstrate the system's ability to classify flow types, detect stationary influences (e.g., branch movements), and correct radial velocity measurements using trigonometric relationships. The results highlight the radar's potential for real-time river monitoring, with applications in flood prediction and hydrological studies, while addressing challenges such as environmental interference and smooth surface reflections.

In the paper Radar Sensors (24 and 80 GHz Range) for Level Measurement in Industrial Processes M. Vogt (2018) provides a comprehensive technical and comparative study of radar sensor technologies, specifically focusing on Frequency-Modulated Continuous Wave (FMCW) radar systems operating in the 24 GHz and 80 GHz bands. The author contextualizes the relevance of accurate level measurement in industrial processes involving both liquids and bulk solids, emphasizing the complexity due to varying material properties like permittivity, conductivity, and surface structure. A main idea is how these properties impact radar reflection, scattering, and signal attenuation, which in turn determine the choice between 24 GHz and 80 GHz systems. Using theoretical formulations and practical field experiments, the study examines the performance characteristics of radar sensors across both frequency bands. Key advantages of 80 GHz systems include narrower antenna beamwidths that minimize interference from tank walls or internal structures, improved range resolution due to larger permissible bandwidths, and faster decay of internal antenna reflections, all contributing to higher signal clarity and reliability in complex measurement environments. However, the paper also cautions that higher frequency does not always ensure superior results—especially in environments with fog or dust (e.g., in silos or over gasoline tanks), where Rayleigh scattering can distort readings at 80 GHz more severely than at 24 GHz due to reduced contrast between the desired and undesired echoes. The study presents a detailed antenna and MMIC-based RF front-end design comparison, highlighting that 80 GHz systems, enabled by SiGe MMICs, offer significant advantages in miniaturization and bandwidth, but require lens-type antennas that limit design flexibility. Empirical results from field tests using sugar powder silos illustrate that 80 GHz radar achieves superior signal-to-noise ratios (up to 39 dB compared to 18 dB at 24 GHz) and sharper echo profile definition, particularly when assessing heap surfaces during dynamic processes like filling. Additional controlled experiments using reflectors and Rayleigh scattering phantoms further support the frequency-based trade-offs in contrast sensitivity. In conclusion, the paper underscores that while 80 GHz radar level meters outperform in many industrial scenarios, particularly where precision and clutter suppression are essential, application-specific considerations like environmental scatter, target material reflectivity, and hardware constraints should guide the selection between 24 GHz and 80 GHz systems, it is illustrated in **Figure 2.5** below:

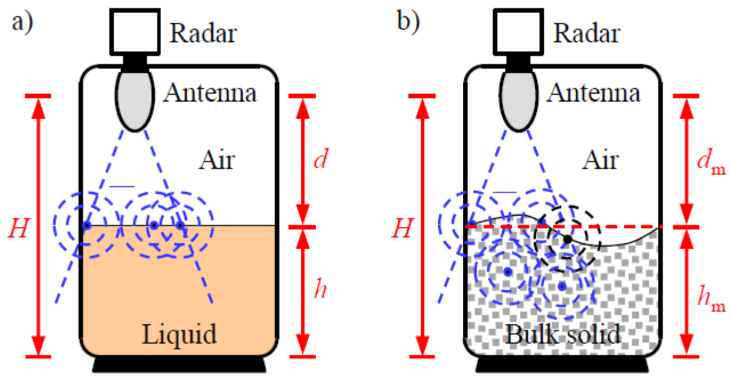

Figure 2.5. Level measurement: a) liquid in the tank, b) bulk solids in a silo

In **Figure 2.5** two tanks are displayed for liquid and bulk solids, Most banks have the same height H, and also has radar fixed on top and antenna is confined inside the tank, on the left we can see the tank dedicated for liquid measurements in (a), The full height of the tank is split between the liquid level and the air space the liquid has a height h, And the distance between the liquid level to the antenna is measured by d, as the liquid has a flat surface all the reflections are made in the same level. We can see the bulk solid tank That include the solids the full height of the tank is split between the solids and the air also but in case of bulk solids as we don't have the flat level like liquids we have the average mean distance h_m that represent the mean height of the solids, And similarly we have d_m as the average distance of air, DM here is obtained from the echo measurements. Due to the irregularity of the surface, multiple reflections take place inside the silo.

The paper titled "Dual Band Signal for more precision in tank gauging radar" by Norouzi et al. (2022). proposes a novel dual-frequency FMCW (Frequency-Modulated Continuous Wave) radar system for tank gauging applications, achieving high precision while operating under narrow bandwidth constraints. Traditional tank level measurement methods, such as mechanical float systems and ultrasonic sensors, face limitations due to environmental factors like temperature and pressure variations. Radar-based systems, particularly FMCW radars, offer superior accuracy as microwave propagation is unaffected by such conditions. However, conventional FMCW radars require wide bandwidths (e.g., 1 GHz) to achieve sub-millimeter accuracy, complicating system design and calibration. The authors address this challenge by introducing a dual-frequency approach, where two FMCW signals with identical bandwidths (100 MHz each) but different carrier frequencies (e.g., 4.5 GHz and 5.5 GHz) are transmitted. By analyzing the phase difference between the two received signals, the system estimates the target range with significantly improved accuracy, independent of the bandwidth. Theoretical analysis shows that the accuracy depends on the frequency separation between the two carriers, enabling narrowband operation without sacrificing precision. **Figure 2.6** Describes the laboratory setup which include a tank with the radar sensor fixed on top, the material below occupy a specific height and the rest of the distance between the level of the material and the sensor dead zone is considered as radar span. The radar dead zone is the depth of the sensor probe.

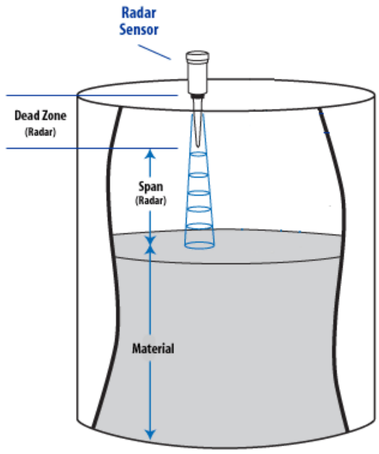

Figure 2.6. Sub-mm accuracy, outperforming conventional wideband FMCW radars

The proposed system achieves sub-millimeter accuracy, outperforming conventional wideband FMCW radars. Simulations in MATLAB demonstrate the method's superiority, showing several-fold accuracy improvements under identical SNR conditions. The dual-frequency design also simplifies implementation using commercial off-the-shelf (COTS) software-defined radio (SDR) systems, reducing cost and calibration complexity. The paper concludes that the proposed method is a viable alternative to conventional tank gauging radars, particularly in industrial settings where narrowband operation and high precision are critical.

The paper titled "Hydrological Information Measurement Using an MM-Wave FMCW Radar" by Ma et al. (2020). explores the application of a 77 GHz millimeter-wave (MMW) FMCW radar for non-contact hydrological monitoring, specifically targeting water level and flow velocity measurements in rivers. Traditional hydrological methods are often costly and hazardous, whereas the proposed radar system offers high precision, operational simplicity, and robustness under varying environmental conditions. The radar leverages FMCW principles to derive range and velocity information from beat signals, with the Doppler frequency shift and time delay providing critical data. To enhance direction-of-arrival (DOA) estimation accuracy, the authors employ the Iterative Adaptive Approach (IAA) instead of conventional algorithms like MUSIC, as IAA outperforms in scenarios with limited snapshots. Experimental validation was conducted using a Texas Instruments AWR1642 radar module at Xiangjiang River, China. The signal processing pipeline included range and azimuth FFTs, clutter suppression via OSCA-CFAR, morphological detection to isolate strong scatterers, and non-coherent accumulation to refine velocity and range estimates. Results demonstrated 95% accuracy in water level measurement and 89% in flow velocity, with IAA providing superior angular resolution compared to MUSIC and CAPON. The study concludes that MMW FMCW radar is a viable tool for hydrological monitoring, with future work aimed at extending its use to unattended stations and river discharge estimation.

In their paper "A Design of the Frequency Modulated Continuous Wave (FMCW) Radar System" Cho & Cho (2014), Yoon Sung Cho and Sung Ho Cho present the design, implementation, and testing of an FMCW radar system specifically tailored for measuring oil levels in tanker environments, prioritizing both economic viability and measurement accuracy. The authors structure the system into two principal segments: an analog front end and a digital signal processing unit. The analog portion employs a horn-type antenna, a hybrid coupler (chosen over a circulator for cost-effectiveness), a mixer, and a voltage-controlled oscillator (VCO), transmitting in the 9.5–10.5 GHz band over a 0.1-second chirp cycle. Notably, the system compensates for the signal loss introduced by the hybrid coupler through antenna gain. The radar is also designed to operate in a ship's dynamic environment, requiring mechanical floating to account for the unstable ground. On the digital side, the authors use a Texas Instruments TMS320C5505 DSP paired with an AIC3204 audio codec to digitize and process the intermediate beat frequency. To improve frequency and thus distance resolution without incurring high computational cost, a Zoom FFT method is implemented, which enhances spectrum detail near the detected peak frequency. During testing in a simulated tank chamber, distance measurements were conducted from 1 m to 17 m at 400 mm intervals, and a peak FFT size of 8192 was employed to extract beat frequency information. The experimental system successfully achieved sub-centimeter resolution, with most errors under 10 mm, although a few reached up to 20 mm due to manual positioning inaccuracies during the test. The system calculates range by analyzing the difference between adjacent frequency samples, corrected using an empirically derived beat frequency of 0.06412 Hz. The results confirm the system's feasibility for real-world level monitoring, with the added benefit of real-time data acquisition and hardware-in-the-loop performance. The paper concludes with plans to integrate both analog and digital components into a single PCB and develop an improved signal processing algorithm for higher precision. The proposed design demonstrates how low-cost, high-resolution radar systems based on DSP and Zoom FFT can serve as reliable non-contact level measurement tools for industrial applications such as oil tankers, where existing optical or mechanical sensors may be less effective or cost-prohibitive.

The paper titled "FMCW Radar for Life-Sign Detection" by Anitori et al. (2009), Ardjan de Jong, and Frans Nennie investigate the use of Frequency Modulated Continuous Wave (FMCW) radar technology to detect vital signs such as breathing and heartbeat in humans, particularly for applications in ambient assisted living (AAL) environments. The study was conducted under the EU-funded SOPRANO project, which aimed to develop next-generation systems for monitoring elderly individuals at home. The authors first determined the optimal radar frequency for life-sign detection by testing four FMCW radars operating at 2.4 GHz, 5.7 GHz, 9.4 GHz, and 24 GHz. Measurements were performed on six volunteers in four positions (front, back, left, and right views) to assess the radar's ability to capture small physiological movements (e.g., chest displacement due to breathing or arterial pulsations). The results indicated that frequencies between 2.4 GHz and 24 GHz were viable, with 9.6 GHz selected as the optimal choice due to bandwidth availability, minimal interference with other devices, and technological feasibility. A compact X-band FMCW radar was designed and built at TNO, featuring dimensions of 8.2 × 6.3 × 1 cm and operating at 9.6 GHz with a linear frequency sweep. The radar system included patch antennas, an ADC card, and USB connectivity for data transfer to a PC. The authors developed five output parameters to quantify life signs: estimated breathing frequency, its reliability measure, estimated heartbeat frequency, its reliability measure, and a binary Life Sign indicator (1 for movement, 0 for no detection). Signal processing techniques, including Fast Fourier Transform (FFT) and autocorrelation, were applied to raw radar data to isolate breathing (0.1–0.4 Hz) and heartbeat (0.8–1.5 Hz) signals. Challenges arose in separating heartbeat signals from harmonics of the stronger breathing signal, but the study demonstrated successful detection of both metrics when measured independently. Validation was performed using an electrocardiogram (ECG) device and visual inspection. The paper concludes that FMCW radar is effective for non-contact life-sign monitoring, particularly for breathing, while heartbeat detection requires further refinement due to spectral overlap with breathing harmonics. Future work will explore advanced signal processing methods (e.g., nonlinear techniques) to improve accuracy. The study highlights the potential of radar technology in healthcare applications, such as remote patient monitoring, while emphasizing the need for robustness in real-world scenarios.

The paper titled "Development of 24GHz FMCW Level Measurement Radar System" by Eugin Hyun et al. (2014), Young-Seok Jin, and Jonghun Lee presents the design and implementation of a low-cost, high-accuracy 24 GHz Frequency Modulated Continuous Wave (FMCW) radar system for industrial level measurement applications, such as monitoring bulk materials (e.g., powdered chemicals, grain) and volatile liquids in storage tanks. Traditional FMCW systems rely on expensive Direct Digital Synthesizers (DDS) to achieve high linearity in frequency modulation, but this study proposes a cost-effective alternative using a frequency synthesizer (Analog Devices ADF4158) to generate a linear frequency sweep over a 2 GHz bandwidth. The system aims to meet stringent requirements for range accuracy (±1% at 30 meters) and resolution (4.578 cm per range step), leveraging a Phase-Locked Loop (PLL) to compensate for voltage-controlled oscillator (VCO) nonlinearities. Key design parameters include a 1 ms ramp interval (PRI), 5 MHz ADC sampling rate, and 8,192-point FFT for signal processing. The authors highlight challenges in achieving high accuracy, such as spectral broadening due to zero-padding in FFT processing and demonstrate through simulations that wider bandwidths (2 GHz) yield better resolution than narrower ones (200 MHz). The hardware architecture includes a transceiver module with a synchronized control signal for power-efficient operation and a signal processing module combining FPGA and DSP for data acquisition and real-time processing. Experimental results validate the system's performance, showing clear beat signals and antenna radiation patterns (24.7 dBi gain, 4.1° beamwidth). Field tests at 10 meters confirm the superiority of the 2 GHz bandwidth in resolving target ranges compared to narrower bandwidths. Future work involves implementing advanced algorithms and adapting the system for noisy, multipath industrial environments.

The paper titled "Design and Evaluation of C-Band FMCW Radar System" by Tushar Yuvaraj Gite et al. (2018). Bazil Raj presents a cost-effective and simplified design of a C-Band Frequency Modulated Continuous Wave (FMCW) radar system for target velocity measurement. The system leverages a Field Programmable Gate Array (FPGA) Spartan 3E board to control the Analog Front End (AFE), including a Voltage Controlled Oscillator (VCO) tuned via a Digital-to-Analog Converter (DAC). The Intermediate Frequency (IF) signal from the AFE is amplified and digitized using an Analog-to-Digital Converter (ADC), with real-time signal processing performed in MATLAB via UART serial communication. The radar operates in the C-Band, utilizing commercially available RF components from Mini-Circuits, and is designed to overcome the high costs and complexity of traditional FMCW systems. Key components include a power amplifier, splitter, transmitting/receiving antennas, Low Noise Amplifier (LNA), and mixer, which collectively enable the generation and processing of linear frequency-modulated signals. The working principle of the FMCW radar is based on measuring the beat frequency between transmitted and received signals to determine target range and velocity via Doppler frequency. Experimental results demonstrate the system's ability to detect moving targets, with the FPGA facilitating real-time data acquisition and MATLAB enabling spectral analysis (FFT) to extract Doppler shifts (e.g., 3 kHz corresponding to 87.3 m/s). The paper highlights the radar's advantages, such as low probability of interception, high reliability, and superior resolution for short-range applications (e.g., automotive and meteorological uses). Future work includes integrating optical sources for RF signal generation and enhancing the system for turbulence-resistant free-space optical communication.

The paper titled "The Risk of Static Electricity at Handling Diesel Fuel" by Părăian et al. (2021), Dan Gabor, and Sorin Iuliu Mangu investigates the hazards of static electricity during diesel fuel handling, particularly in industrial settings such as loading tankers. The study highlights that diesel fuel, despite its relatively high flash point (55°C), can generate static charges when transported through pipes, filtered, or agitated, which may discharge and ignite explosive atmospheres under certain conditions. The authors analyze a case study involving an explosion during diesel loading, attributing the incident to residual gasoline vapors from prior transport (a practice known as "switch-loading") combined with high flow rates (3.92 m/s) and low fuel conductivity (9.1 pS/m). Key factors influencing static charge accumulation include fuel properties (conductivity, sulfur content), flow velocity, pipe diameter, and equipment grounding. The paper categorizes hydrocarbons by conductivity (high: >10,000 pS/m; medium: 50–10,000 pS/m; low: <50 pS/m) and emphasizes the risks of brush and spark discharges, especially in low-sulfur diesel (ULSD). Mitigation strategies include bonding/grounding conductive parts, limiting flow rates (e.g., $\leq$0.38 m²/s for ULSD), ensuring 30-second residence times post-filtration, and avoiding switch-loading without compartment cleaning. The study concludes with recommendations for procedural and technical measures, such as using static dissipater additives (SDAs) and revising safety protocols to align with standards like IEC TS 60079-32-1 and API RP 2003, to prevent similar accidents.

The paper titled "Educational Low-Cost C-Band FMCW Radar System Comprising Commercial Off-the-Shelf Components for Indoor Through-Wall Object Detection" by Jeong & Kim (2021), Kim presents a cost-effective, educational Frequency-Modulated Continuous Wave (FMCW) radar system designed for indoor through-wall detection of metallic objects. Operating in the C-band (5.83–5.94 GHz), the system integrates commercial off-the-shelf (COTS) components, including a voltage-controlled oscillator (VCO), two-stage power amplifier (PA), low-noise amplifier (LNA), mixer, and custom cylindrical horn antennas with a gain of 6.8–7.8 dB. The radar's RF front-end is synchronized using a modulator generating triangular waves for frequency modulation, while an Arduino UNO samples the backscattered signal at 4.5 kHz for processing in MATLAB. The system achieves a detection range of 56.3 meters indoors and can penetrate 4 cm plywood walls with an accuracy of <10 cm, despite a theoretical range resolution of 1.36 m due to its 110 MHz bandwidth. Key innovations include a dominant-mode antenna design, DC offset removal for signal clarity, and a piecewise cubic Hermite interpolating polynomial (PCHIP) algorithm to enhance range estimation. The total cost is under USD 100, making it accessible for educational and IoT applications, such as indoor positioning and remote sensing. The study validates the system's performance through experiments, demonstrating its scalability and potential for low-cost radar technology development.

The paper titled "Software-defined Calibration for FMCW Phased-Array Radar" by Li et al. (2010), Jeffrey Krolik presents a novel calibration method for Frequency-Modulated Continuous Wave (FMCW) phased-array radars, addressing both temporal and spatial distortions caused by hardware imperfections. The proposed approach leverages software-defined techniques to compensate for nonlinearities in the voltage-controlled oscillator (VCO) and inter-channel phase/amplitude variations in low-cost commercial-off-the-shelf (COTS) S-band radar systems (2.1–2.7 GHz). For temporal calibration, a dynamic closed-loop method estimates VCO nonlinearities by modeling the transmitted signal's phase, then applies inverse correction via non-uniform resampling, achieving a 99.97% reduction in phase error (from 100% to 0.03% DON). Spatial calibration corrects inter-channel delays and amplitudes by comparing each channel to a reference, applying frequency shifts and phase ramps to align outputs. Experimental results on an 8-element array demonstrate near-theoretical performance: 1-foot range resolution and 16° azimuthal beamwidth, with sidelobes reduced to -13 dB. The method is validated through closed-loop tests using a 3.8-meter coaxial delay line and beamforming experiments, showing accurate pattern steering (e.g., at ±25° and 35°). The calibration framework is computationally efficient, compatible with field deployments using strong target returns, and enhances the viability of low-cost COTS radars for precision applications.

The paper titled "An FMCW MIMO Radar Calibration and Mutual Coupling Compensation Approach" by Christian M. Schmid (2013), Reinhard Feger, and Andreas Stelzer presents a novel calibration method for Frequency-Modulated Continuous Wave (FMCW) Multiple-Input Multiple-Output (MIMO) radar systems, addressing channel gain/phase variations and mutual coupling effects that degrade beam patterns and direction-of-arrival (DOA) estimation. Unlike existing methods requiring precise sub-millimeter alignment of calibration targets, the proposed approach relaxes calibration setup constraints by only requiring targets at known angular positions without exact range knowledge. The method constructs an ideal signal model from measured data of the first receive channel, preserving relative phase differences across other channels. A least-squares optimization then derives a transformation matrix to compensate mutual coupling and channel mismatches. Simulations using an 8-channel virtual array (36 RX channels) with random coupling magnitudes (0.7–1.3) and phases (−40 dB off-diagonal) demonstrate a significant reduction in side-lobe levels (SLL), approaching theoretical limits. Experimental validation on a 77 GHz FMCW MIMO system with a rotatable platform and corner reflector showed SLL improvement despite coarse platform alignment (centimeter-level accuracy). The method's key advantage is its practicality for applications like automotive radar, where phase information is often discarded post-beamforming, enabling robust performance with relaxed calibration requirements.

The paper titled "Modern FMCW Radar - Techniques and Applications" by Stove (2004), A. G. Stove provides a comprehensive review of advancements in Frequency-Modulated Continuous Wave (FMCW) radar technology, highlighting its growing applications and technical innovations over the past decade. The author traces the historical development of FMCW radar, from early uses in World War II bomb-aiming systems to modern digital signal processing (DSP)-enabled implementations, emphasizing its advantages such as simple architecture, low peak power compatibility with solid-state transmitters, and Low Probability of Intercept (LPI) characteristics. Key applications discussed include automotive radars for Autonomous Cruise Control (ACC), where FMCW's efficiency and scalability are critical, and military uses like battlefield surveillance and missile seekers, leveraging LPI properties. Technical advancements covered include Direct Digital Synthesis (DDS) for precise, linear sweep generation, though its quantization noise challenges are noted, and improvements in YIG-tuned oscillators for reduced phase noise. The paper also explores Moving Target Indication (MTI) processing for clutter suppression in military radars and the development of active phased arrays using FMCW modulation, exemplified by Thales' Dual Linear Array (DLA), which combines separate transmit/receive modules for optimized performance. Challenges such as AM noise measurement and the evolving "LPI battle" between radars and Electronic Support Measures (ESM) are addressed, alongside future research directions. The review concludes that FMCW radar has matured into a versatile technology with proven utility in both civilian and defense sectors, supported by innovations in waveform generation and system design.

The paper titled "Correcting Nonlinear Modulation Error in Linear FMCW Radar Systems" by Grosch (2017). Theodore Grosch addresses the challenge of nonlinear modulation errors in frequency-modulated continuous-wave (FMCW) radar systems, which degrade range and Doppler resolution. The author highlights that ideal FMCW radar performance relies on perfectly linear frequency modulation, but practical systems often suffer from nonlinearities due to imperfections in voltage-controlled oscillators (VCOs) or other components. These nonlinearities introduce phase errors in the baseband intermediate-frequency (IF) signal, leading to distorted range profiles and reduced target detection accuracy. The paper presents a calibration technique that leverages data from a single calibration target to estimate and correct these phase errors, employing an autofocus method. The author derives the mathematical relationship between modulation errors and phase distortions, showing that the phase error can be expressed as a power series dependent on time and target range. By measuring the phase error from a calibration target at a known distance, the method scales this error to correct signals from targets at other ranges, effectively compensating for nonlinear modulation across the entire detection range. Experimental results demonstrate the technique's effectiveness: using a trihedral reflector as a calibration target, the author corrects severe nonlinearities in the IF signal, achieving sharp focus in the range profile after correction. The paper also discusses limitations, such as the need for phase unwrapping and the computational cost of applying corrections across all range bins. The proposed method offers a low-cost, hardware-free solution for improving FMCW radar performance, making it suitable for systems where precise linear modulation is difficult to achieve. The work concludes by validating the approach through real-world measurements, showing significant improvements in target focus and range resolution.

The paper titled "A Method of Fast and Simultaneous Calibration of Many Mobile FMCW Radars Operating in a Network Anti-Drone System" by Nowak et al. (2019). Aleksander Nowak, Krzysztof Naus, and Dariusz Maksimiuk addresses the critical challenge of calibrating multiple mobile frequency-modulated continuous-wave (FMCW) radars in anti-drone systems to ensure accurate azimuth alignment with true north. The authors highlight the growing threat posed by drones, including privacy violations and security risks, and emphasize the need for mobile anti-drone solutions that can operate effectively in dynamic environments. Traditional calibration methods, such as geodetic techniques or magnetic compasses, are insufficient due to their low accuracy (often exceeding 20°) or impracticality for mobile systems. The proposed method leverages a "friend" drone flying a predefined route to collect synchronized measurements from multiple radars, enabling the estimation and correction of constant azimuth errors. The approach involves formulating a system of equations based on radar measurements (azimuth and distance) and solving it iteratively using least squares optimization to derive corrections for each radar. The method was validated through 95,000 numerical simulations, demonstrating significant improvements in azimuth alignment. The authors conclude that the method is highly practical for mobile anti-drone networks, as it requires no specialized hardware, operates autonomously, and significantly enhances system performance by minimizing ghost targets and misclassification errors. Future work will focus on optimizing the calibration flight route and refining the initial drone position estimation to further improve accuracy.

In his 2013 study titled "Ground Penetrating Radar Simulations of Non-Homogeneous Soil with CST Studio Suite" by Zych (n.d.), Mariusz Zych explores the simulation and signal processing pipeline for imaging subsurface structures using ground-penetrating radar (GPR) in non-homogeneous soil environments. Utilizing CST Studio Suite’s transient solver, Zych models a complex soil structure composed of dry sand, loamy soil, bone fragments, and forty-year-old concrete, arranged as prisms within a defined geometry. A wideband horn antenna operating just 10 cm above the surface is used to transmit and receive linearly frequency-modulated (LFM) pulses, with data collected from 145 spatial points along a 1.45-meter scan path. The simulation employs a 2 GHz bandwidth and a 5 ns pulse duration, yielding high temporal resolution but significant sidelobe levels (~–13 dB) typical of LFM signals. These sidelobes are mitigated via Hamming windowing. The signal data produced by CST features irregular time sampling—common in electromagnetic solvers—necessitating interpolation using MATLAB's interp1 function before matched filtering can be performed. Noise removal is addressed through Burg’s lattice filter, which subtracts the reflection component (S11) from the system response, improving the visibility of true subsurface reflections. Demodulation and low pass filtering of the signal further isolate the meaningful radar returns. Range compression reveals echo delays corresponding to major permittivity boundaries within the soil, although not all structures are clearly resolved due to signal attenuation, multipath effects, and mismatches in dielectric constant assumptions. To enhance spatial resolution in the movement (azimuth) direction, Zych applies a focused Synthetic Aperture Radar (SAR) filtering algorithm. The process involves blockwise 2D matched filtering with Hamming-weighted convolution, tuned for depth and dielectric assumptions. While SAR improves target clarity, its effectiveness is limited by challenges such as distorted reflections, oblique layer geometry, and variations in propagation velocity. The study highlights the critical role of accurate permittivity models in subsurface imaging, revealing how even slight mismatches can cause shifts and artifacts in the reconstructed image. Zych concludes that while CST Studio Suite is a powerful platform for simulating realistic GPR environments, achieving full subsurface clarity requires enhanced signal designs (e.g., FMCW or NLFM), accurate dielectric profiling, and advanced post-processing techniques like focused SAR rather than traditional hyperbolic fitting methods such as the Hough Transform.

The paper titled "Underground Target Objects Detection Simulation Using FMCW Radar with SDR Platform" by MacAsero et al. (2018). Jesrey Martin S. Macasero, Olga Joy L. Gerasta, Daryl P. Pongcol, Vrian Jay V. Ylaya, and Aileen B. Caberos explores the implementation of a Frequency Modulated Continuous Wave (FMCW) radar system on a Software Defined Radio (SDR) platform for detecting underground targets. The researchers utilized National Instruments' Universal Software Radio Peripheral (USRP) and LabVIEW™ to develop a flexible, cost-effective alternative to commercial ground-penetrating radar systems. The FMCW radar transmits a linear chirp signal, and the received echo signal is correlated with the reference signal to determine the target's distance by analyzing the phase shift and beat frequency. The system was tested using a simulated soil strata model with layers of silt, gravel, clay, and bedrock, demonstrating successful signal penetration and target detection at depths of 1, 2, and 3 meters. Key challenges included limited penetration depth due to the USRP's operating frequency range (400 MHz–4.4 GHz) and computational constraints of the host PC, which affected real-time signal processing accuracy. Despite these limitations, the study validated the feasibility of using SDR-based FMCW radar for underground detection, highlighting its potential for further refinement in precision and depth mapping. The paper concludes that this approach offers a scalable, software-driven solution for non-invasive subsurface surveying, with future work focusing on optimizing signal processing algorithms and hardware configurations for real-world applications.

The paper titled "Ranging and SAR Imaging of Underground Targets Using Laptop-based FMCW RADAR" by Bordoloi et al. (2017). Sudipto Bordoloi, Bikram Singh, Roshan Dhakal, and Sagar Dutta present a portable, cost-effective Frequency Modulated Continuous Wave (FMCW) radar system for detecting and imaging underground targets. The system operates at 2.4 GHz and utilizes a bi-static radar topology with cylindrical metal antennas, a Voltage Controlled Oscillator (VCO) for generating FMCW signals, and a laptop for signal recording and processing. Key components include a modulator (XR-2206), a baseband amplifier (MAX412), and a mixer to derive the beat frequency from reflected signals. The researchers implemented Synthetic Aperture Radar (SAR) imaging using the Range Migration Algorithm (RMA), which involved estimating soil permittivity through an iterative auto-calibration method to correct for mismatches in the matched filters. Experimental results demonstrated successful detection of buried objects at depths of 0.12 m, 0.45 m, 0.85 m, and 1.5 m, with SAR images generated from sub-beams merged to form a final composite image. Challenges included noise interference and the need for precise permittivity estimation, which was addressed using an Auto ESP algorithm. The paper highlights the system's potential for geophysical surveys and military applications, while suggesting future improvements such as real-time data processing, FPGA-based signal acquisition, and mechanical stabilization for enhanced accuracy. The study concludes that laptop-based FMCW radar is a viable, low-cost alternative to commercial Ground Penetrating Radar (GPR) systems, with scalability for educational and hobbyist applications.

In their paper "Study on Signal Processing of FMCW Ground Penetrating Radar" by Liang & He (2009), Huaqing Liang and Zhiqiang present an advanced signal processing strategy for Frequency-Modulated Continuous-Wave (FMCW) Ground Penetrating Radar (GPR) systems, aiming to enhance the detection and measurement of thin underground layers such as asphalt and concrete in road and airport pavements. The authors identify a key limitation of traditional FFT-based methods in FMCW GPR: weak reflections from deep or thin subsurface layers are often masked by strong reflections from surface layers due to side-lobe leakage and limited frequency resolution. To address this, they propose a two-step enhancement strategy combining Adaptive Noise Cancellation (ANC) and a Modified Frequency Estimation Method (MFEM). ANC is used to suppress the dominant surface echo by exploiting the correlation between delayed versions of the beat signal, minimizing the mean square error via a Least Mean Squares (LMS) algorithm. This step significantly boosts the signal-to-noise ratio of weaker echoes without requiring a priori knowledge of layer depths. Following this, MFEM compensates for the frequency resolution loss inherent to short data windows in FFTs. The method estimates the main-lobe center using a weighted interpolation between adjacent FFT bins, improving accuracy even when signal frequencies fall between spectral lines. Simulation experiments with synthetic signals confirm that ANC effectively suppresses surface reflections, revealing otherwise submerged deeper echoes. MFEM then achieves sub-Hertz resolution improvements, outperforming direct FFT peak detection. For example, in test cases with signals at 810 Hz and 980 Hz buried in noise, MFEM reduced frequency estimation errors from over 10 Hz (FFT) to under 0.5 Hz. These enhancements are critical for resolving layers with minor dielectric contrast and minimal thickness differentials. The paper also provides mathematical derivations, practical implementation steps, and quantitative results demonstrating the efficacy of both techniques. The authors conclude that the combined use of ANC and MFEM enables high-resolution thickness measurements in layered media, extending the practical range and precision of FMCW GPR systems for applications in transportation infrastructure and geotechnical analysis.

In their paper "FMCW Radar Near Field Three-Dimensional Imaging," by Yang et al. (2012), Jungang Yang, John Thompson, Xiaotao Huang, Tian Jin, and Zhimin Zhou introduce a computationally efficient 3D range migration imaging algorithm tailored for near-field Frequency-Modulated Continuous Wave (FMCW) radar systems, particularly in applications such as concealed weapon detection at security checkpoints. The authors build on the conventional two-dimensional range migration algorithm (2D-RMA) and extend it into the third spatial dimension by incorporating a 3D version of Stolt interpolation and leveraging the principle of stationary phase (POSP) for fast convolution in the Fourier domain. The system employs a millimeter-wave FMCW radar operating with a 94 GHz center frequency and a 6 GHz bandwidth, using a planar 2D synthetic aperture to collect backscatter data across spatial (X, Z) and frequency (range) domains. The 3D imaging geometry captures reflect signals across sampled aperture points and construct a full volumetric image by matching frequency components to range profiles and performing inverse Fourier transforms in all three dimensions. The authors thoroughly derive the signal model, starting with the transmitted signal, echo formation, mixing, and range compensation, followed by range wavenumber transformation and matched filtering. Notably, only one-dimensional interpolation (in the range direction) is needed, reducing computational burden compared to full-angle compression or back-projection techniques. The authors validate their approach through simulations with eight equidistant point targets, showing that the achieved spatial resolution in the X and Z directions is 0.92 cm and in the Y direction is 2.65 cm—very close to the theoretical limits of 1 cm (X, Z) and 2.5 cm (Y). The simulation output includes three orthogonal slices (X-Z, Y-Z, Y-X) and amplitude profiles, all indicating high-fidelity focusing. The paper concludes by emphasizing that the proposed method achieves accurate 3D imaging without assuming far-field conditions, which is vital for confined detection spaces like airport security zones or scanning systems integrated into compact enclosures. By combining analytic modeling, frequency-domain transformation, and efficient signal processing, this research significantly contributes to real-time, high-resolution FMCW radar imaging.

The paper titled "Sea Surface Imaging with a Shortened Delayed-Dechirp Process of Airborne FMCW SAR for Ocean Monitoring on Emergency" by Hwang & Kim (2020), Ji-hwan Hwang and Duk-jin Kim presents a novel technique for sea surface imaging using a ready-made airborne Frequency Modulated Continuous Wave Synthetic Aperture Radar (FMCW SAR) system, optimized for emergency maritime monitoring. Traditional high-resolution SAR systems for ocean observation are costly and require precise 3D gimbal systems to control radio wave incidence angles, making them impractical for urgent disaster response. The authors propose an alternative approach using a compact, cost-effective FMCW SAR system with a fixed incidence angle of 45°, originally designed for ground observation. By leveraging the delayed-dechirp signal processing technique, the system indirectly adjusts the effective incidence angle to near-nadir, enabling the collection of sea clutter signals at low angles where backscattering is stronger. Theoretical analysis using the Integral Equation Model (IEM) and experimental data confirmed that sea clutter signals attenuate rapidly beyond 20° incidence angles, necessitating adjustments to the system's sampling process. Flight experiments demonstrated that manually shortening the dechirp-delay time allowed the system to acquire raw data at near-nadir angles, which were then reconstructed into SAR images using the Range-Doppler Algorithm (RDA). Performance validation using dual-channel along-track interferometry (ATI) images revealed coherence and phase difference metrics, confirming the feasibility of sea surface imaging within a 35° incidence angle. The study concludes that the proposed method offers a viable, albeit limited, solution for emergency maritime monitoring, such as detecting oil spills or ship movements, when high-performance systems are unavailable.

The paper titled "UAV-Borne FMCW InSAR for Focusing Buried Objects" by Burr et al. (2022), Ralf Burr et al. presents an innovative approach for detecting buried antipersonnel landmines using a UAV-mounted Frequency Modulated Continuous Wave (FMCW) radar system with interferometric synthetic aperture radar (InSAR) capabilities. Traditional ground-penetrating radar (GPR) systems face challenges in subsurface imaging due to the unknown topography of the air-soil interface, which degrades image quality when approximated as a flat plane. To address this, the authors propose a two-step method leveraging dual-frequency bands (1–4 GHz for subsurface imaging and 6–9 GHz for surface mapping) in time-division multiplex mode. The higher-frequency band generates a digital elevation model (DEM) via InSAR, while the lower-frequency band uses this DEM to improve subsurface focusing accuracy. The system employs a circular flight trajectory to enhance resolution and employs a backprojection algorithm that incorporates refraction laws and DEM data to correct for soil permittivity effects ($\varepsilon_r = 8$). Experimental validation on a meadow with buried can lids demonstrated a DEM accuracy of ±4 cm, enabling clear detection of targets at 5 cm depth with an 18 dB signal-to-clutter ratio. The study highlights that DEM-based correction significantly improves target localization and amplitude focus, with errors in surface height estimation reducing detection performance by 5–10 dB. This UAV-borne system offers a scalable, autonomous solution for humanitarian demining, combining high-resolution surface mapping with robust subsurface detection.

The paper titled "Design and validation tests for compact FMCW C-band Analog-Front-End for radar imaging applications" by Gromek et al. (2016), Damian Gromek presents the development and testing of a compact, low-cost C-band (5.5 GHz center frequency) analog-front-end (AFE) for Frequency Modulated Continuous Wave (FMCW) radar systems, designed for applications such as synthetic aperture radar (SAR), moving target indication (MTI), and short-range imaging. The AFE, built using commercial off-the-shelf (COTS) RF components, features a homodyne architecture with a 480 MHz bandwidth, enabling a range resolution of 30 cm and cross-range resolution of 15 cm. The system utilizes a 12× frequency multiplier to upconvert a 460 MHz intermediate frequency (IF) signal generated by a Universal Software Radio Peripheral (USRP) to the C-band, followed by amplification, mixing, and filtering to produce a beat signal for target detection. Key challenges addressed include leakage cancellation, harmonic suppression, and phase noise mitigation, with high-pass and low-pass filters employed to isolate the beat signal and minimize interference. Laboratory tests demonstrated successful MTI operation, detecting a running human at 80 m with velocity resolution, while ground-based SAR trials using a car-mounted system achieved imaging of urban and natural terrain. Airborne SAR tests on a small aircraft (PZL-104 Wilga) further validated the system's capability to produce high-resolution images, corroborated by optical satellite comparisons. The AFE's compact size (20 × 15 × 5 cm^3), lightweight (5.2 kg), and modular design (later adapted to SMD technology) make it suitable for UAV integration. The authors conclude that the system's cost-effectiveness, flexibility, and performance in real-world scenarios position as a viable solution for academic and practical radar applications, with future work planned for multi-channel interferometric enhancements.

In the paper "Modeling Small UAV Micro-Doppler Signature Using Millimeter-Wave FMCW Radar" by Passafiume et al. (2021), Passafiume propose and validate a compact analytical model to describe the micro-Doppler signatures of small unmanned aerial vehicles (UAVs) using millimeter-wave frequency-modulated continuous-wave (FMCW) radar systems, with the goal of classifying UAV types based on the number of rotors. Recognizing the growing demand for UAV detection in security and surveillance due to potential misuse, and the challenge posed by their small radar cross-sections (RCS), low flying altitudes, and speeds, the authors focus on micro-Doppler effects produced by vibrating and rotating parts (particularly rotor blades). The model accounts for vibrational components corresponding to pitch, roll, and yaw dynamics of multiple rotors, and mathematically expresses the composite frequency modulation generated by UAV structural vibrations. Simulations are derived using a deterministic equation with 13N parameters, where N is the number of motors, allowing differentiation among UAV classes based solely on vibrational patterns. To verify this, they implement experimental measurements using a 77 GHz MIMO FMCW radar platform and UAV prototypes in an anechoic chamber, comparing the measured radar images with those synthesized from the model. The match is evaluated using a correlation-based confusion matrix and a genetic algorithm to fit the model parameters. The key result is that while variations in motor speed had limited influence on classification, the number of motors produced clear, distinguishable micro-Doppler patterns. Therefore, the model reliably classifies UAVs by motor count, which significantly reduces the training dataset size needed for machine learning applications and can help form the basis for unsupervised or deterministic classification schemes. This is a valuable contribution toward UAV fingerprinting using radar, avoiding the need for exhaustive real-world data collection and enabling robust UAV detection under various operating conditions.

The paper titled "Development and Preliminary Results of Small-Size UAV-Borne FMCW SAR" by X. Zhang et al. (2018), Xiangkun Zhang presents the design, development, and experimental validation of a compact Frequency Modulated Continuous Wave Synthetic Aperture Radar (FMCW SAR) system for small unmanned aerial vehicles (UAVs). The study addresses the challenges of miniaturizing SAR systems for UAV payload constraints while maintaining high resolution and reliability. Unlike traditional pulsed SAR, FMCW SAR employs continuous low-power transmissions, reducing system size and cost but introducing challenges such as transmitter-receiver isolation and motion-induced phase distortion. The authors detail a three-stage development process: (1) prototype validation, (2) miniaturization (<3 kg), and (3) achieving higher resolution (0.3 m). Key innovations include a two-antenna design to improve isolation (58 dB vs. 25 dB with circulators) and a modified frequency scaling algorithm to correct phase errors from UAV motion during long signal sweeps. Flight experiments using a conveyor aircraft and multi-rotor UAVs demonstrated successful imaging, with results validated against optical references. Indoor and inverse SAR (ISAR) tests further confirmed resolution capabilities (0.3 m) and short-range performance. The paper concludes with plans for a next-generation 0.1 m-resolution system, emphasizing trade-offs between weight, stability, and imaging quality for UAV integration.

The paper titled "Calibration of Wideband FMCW Polarimetric Radars Operating at Millimeter-Wave Frequencies" by Nashashibi et al. (2022). Adib Y. Nashashibi, Mani Kashanianfard, and Kamal Sarabandi presents a comprehensive technique for calibrating wideband Frequency-Modulated Continuous-Wave (FMCW) polarimetric radars, which are critical for high-resolution imaging and sensing applications at millimeter-wave (MMW) frequencies. The authors address the challenges posed by systematic distortions in polarimetric FMCW radars, including nonlinearities in the transmitted and received chirp signals and channel imbalances in polarimetric measurements. The paper begins by introducing the growing importance of MMW radars in applications such as autonomous vehicles, robotics, and security due to their compact size, high resolution, and all-weather capabilities. However, these radars suffer from distortions that degrade performance, necessitating robust calibration methods. The authors develop a detailed distortion model that accounts for both polarimetric distortions (e.g., channel imbalances and polarization leakage) and nonlinear phase errors in the chirp signals. A key contribution of the paper is the proposed three-step calibration technique. First, nonlinear phase errors are estimated and corrected using measurements from two-point targets at known distances. This step addresses range-dependent phase distortions, enabling the radar to achieve its ideal range resolution. Second, channel imbalances in the polarimetric radar are corrected using a metallic sphere (for co-polarized calibration) and a depolarizing target (for cross-polarized calibration). The authors simplify the model by assuming high cross-polarization isolation, reducing the complexity of the calibration process. Finally, additional losses in the receiver channels are accounted for to ensure accurate scattering matrix retrieval. The paper validates the calibration technique through numerical simulations and experimental measurements using a polarimetric FMCW radar operating at 76.5–82 GHz. Simulations demonstrate the effectiveness of the phase-error removal technique in restoring range resolution, while experimental results confirm the accuracy of the calibrated radar responses for both co-polarized and cross-polarized targets. The proposed method is shown to outperform simpler calibration approaches, particularly for targets at varying ranges. In conclusion, the paper provides a robust and practical calibration framework for wideband polarimetric FMCW radars, addressing critical challenges in high-frequency radar systems. The techniques presented are essential for applications requiring precise polarimetric measurements and high-resolution imaging, such as autonomous navigation and remote sensing.

The paper by Tokieda et al. (2005) presents a high-precision FMCW radar water level gauge to operate under strict bandwidth limitations imposed by license-free radio regulations in Japan. Conventional water level measurement methods like float-based or ultrasonic sensors have significant limitations - contact methods are prone to pollution and damage, while ultrasonic systems are affected by atmospheric conditions. Radar-based solutions offer non-contact operation but typically require wide bandwidths, for sufficient accuracy. The authors address the challenge of developing a practical system under Japan's 76MHz bandwidth restriction (theoretical resolution limit: 197cm) while achieving centimeter-level accuracy required for water level monitoring. The developed system operates at 24.15GHz with 75MHz bandwidth, incorporating several key innovations to overcome three primary disturbance factors: multiple reflections (mitigated through separate horn antennas and internal reflecting plates), image frequency interference (addressed via quadrature detection and IQ imbalance correction), and latent circuit noise (handled through switchable RF amplifiers for noise sampling). The signal processing chain features sophisticated preprocessing (noise removal and IQ correction), frequency estimation (using zero-padded FFT for sub-resolution accuracy), and postprocessing (moving average filtering). Experimental validation demonstrated impressive performance: measurement deviations were <3cm within 4m range and <1cm beyond 4m, with water level monitoring in a test pool showing errors within ±3cm across 1.5-9.5m range. The system showed particular robustness from 4.5-6m with only ±1cm error, though a 2.5cm discontinuity at 4m (related to window function switching between rectangular and Hanning windows) remains unexplained. The achieved accuracy of 1.5% of theoretical resolution represents a significant advancement for license-free radar applications, making the system suitable for river monitoring and disaster prevention while complying with regulatory constraints.

The paper by Vincenti Gatti et al. (2024) presents a novel dual-mode FMCW-Doppler radar system with frequency scanning capability designed specifically for river monitoring applications. The system addresses the critical need for accurate measurement of river discharge parameters (water level and surface velocity) using non-contact sensing technology. The radar operates at 24 GHz and features a unique frequency-scanning planar array antenna implemented in substrate integrated waveguide (SIW) technology, which enables beam steering across ±30° in azimuth without mechanical movement or complex phased array electronics. The antenna design leverages frequency squint effects through a custom feeding network with delay lines, allowing direction-of-arrival estimation through frequency selection while maintaining a compact form factor. The system operates in both FMCW mode (for static target detection and water level measurement) and Doppler mode (for surface velocity measurement), with all signal processing implemented on a Raspberry Pi for edge computing applications. Key innovations include: 1) A passive frequency scanning antenna array with 6°×9° beamwidth that achieves 60° angular coverage from 23-25 GHz; 2) Dual-mode operation enabling both range/position measurement (FMCW) and velocity measurement (Doppler) with the same hardware; 3) Low-power implementation (9 dBm transmit power) capable of detecting targets up to 80m away. Experimental validation demonstrated successful static target detection in a campus environment (18-71m range) and accurate water level measurement (±10cm) on the Tiber River compared to reference ultrasonic sensors. Doppler mode measurements provided surface velocity profiles across river transects (2.2-2.3 m/s) during high flow events. The system's performance represents a significant advancement over previous frequency scanning radars, offering improved range (80m vs typical <40m), dual-mode capability, and specialized river monitoring functionality while maintaining simple signal processing requirements suitable for edge deployment.

The paper titled "Acoustic Signal Reconstruction Across Water-Air Interface Through Millimeter-Wave Radar Micro-Vibration Detection" by Du et al. (2024), explores a novel method for cross-media communication between underwater and aerial environments using acoustic and millimeter-wave technologies. The authors propose an Acoustic Electromagnetic Wave-based Information Transmission (AEIT) system that leverages the interaction between underwater acoustic waves and water surface micro-amplitude waves (WSMWs). When underwater acoustic waves propagate to the water-air interface, they induce minute vibrations on the water surface with frequencies identical to the acoustic source. These vibrations are detected using a millimeter-wave radar that transmits a frequency-modulated continuous wave (FMCW) and measures the phase shift in the reflected signal, which encodes the displacement information of the water surface. The study introduces an Energy Conversion from Underwater Acoustic to Vibration (ECUAV) model to predict the amplitude of WSMWs based on the sound source level (SL) and frequency, demonstrating a direct relationship between SL and surface vibration amplitude. Experimental validation in a controlled water tank environment confirmed the model's accuracy, showing peak vibration amplitudes at specific frequencies (e.g., 1.89 μm at 135 Hz). The system successfully reconstructed dual-band binary frequency shift keying (BFSK) modulated signals, achieving a transmission rate of 3 bps with minimal error. **Figure 2.7** and **Figure 2.8** below describe the experiment setup and results respectively.

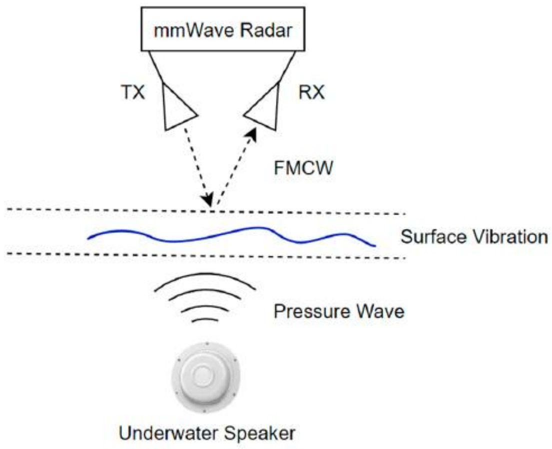

Figure 2.7. Underwater Acoustic to Vibration (ECUAV) model

In **Figure 2.7** Above, the experiment setup consists of an underwater Speaker, This speaker emits sound waves under the water. Above this speaker there is the surface of the water that Demonstrates the surface vibrations. On the top of the surface of the water there are the TX and RX antennas of the millimeter wave radar.

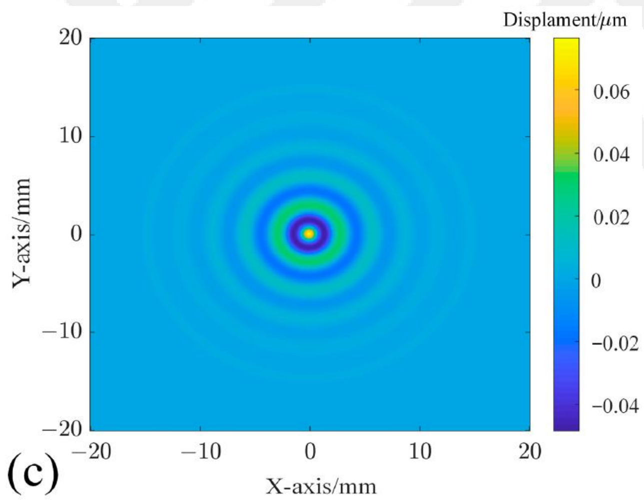

Figure 2.8. Prediction of amplitude based on sound source level and frequency

In Figure 2.8 above, a graphical representation from dark blue to yellow, the author used dark blue to represent-0.04 micrometer and the yellow for more than 0.06 micrometer, the representation is in a square 40 x 40mm, both axes are in scale of millimeter and the origin point is in the center. The findings highlight the potential of millimeter-wave radar for efficient cross-media communication, offering advantages such as anti-interference capabilities and applicability in complex marine environments. However, challenges remain, including the need for further testing in larger, dynamic water bodies and the development of more robust modulation techniques to mitigate multipath interference, The paper titled "Microwave Dielectric Properties of Plant Materials" by Ulaby & Jedlicka (1984), Fawwaz T. Ulaby and R. P. Jedlicka investigates the dielectric properties of vegetation, such as corn and wheat leaves and stalks, as a function of moisture content and microwave frequency (1.1–8.4 GHz). The study employs waveguide transmission systems to measure the complex dielectric constant, revealing that the dielectric behavior of vegetation is dominated by the water content, which includes both free and bound water, with the latter exhibiting ice-like properties. The extracted liquid from vegetation was found to have a salinity of about 10 per mil, significantly affecting dielectric loss at frequencies below 5 GHz. The authors explore various dielectric mixing models to relate the measured dielectric constants to the volume fractions of constituent components (bulk vegetation, air, bound water, and free water), though no single model provided a universally accurate fit. The study also includes field measurements of canopy attenuation at 10.2 GHz for corn and soybean canopies, demonstrating that absorption and scattering losses vary with canopy growth stages and moisture content. The findings highlight the challenges in modeling vegetation dielectric properties due to the complex factors like salinity, and canopy structure. The research highlights the need for further experiments to refine models for microwave remote sensing applications.

The paper titled "Remote Material Characterization with Complex Baseband FMCW Radar Sensors" by Hegazy et al. (2023), Ahmed M. Hegazy presents a novel technique for remotely characterizing materials using a low-cost, commercial FMCW radar with a complex baseband architecture. The authors develop theoretical models—transmission line and multiple reflections—to derive the complex reflection coefficient Γ_{in} of a material slab, which encodes dielectric properties (ε_r, $\tan\delta$), thickness (d), and layer configuration. By leveraging both magnitude and phase information from the radar's complex baseband signal, the method achieves high accuracy despite multipath interference and long measurement distances (2 m). The experimental setup uses a Texas Instruments AWR2243 radar (77 GHz, 5 GHz bandwidth) with a custom 3D-printed hyperbolic lens to correct beam alignment. Two extraction methods are proposed: (1) the maxima and minima method, suitable for lossless materials, which analyzes periodic features in Γin to compute ε_r and d (e.g., ε_r=2.44 for HDPE); and (2) nonlinear curve fitting, applicable to lossy materials, which fits Γ_{in} magnitude/phase to theoretical models (e.g., PMMA: ε_r=2.5, $\tan\delta$=0.0099). A calibration process de-embeds system errors using metal-short and matched-load measurements. Results show strong agreement with literature values (e.g., HDPE thickness error <3%), outperforming traditional methods (e.g., VNA-based) in cost, portability, and tolerance to non-anechoic environments. The work highlights the potential of FMCW radar for industrial applications like quality control and non-destructive testing.

The paper by Barowski et al. (2018) presents a method for characterizing dielectric materials in the millimeter-wave (mm-wave) range (200–250 GHz) using calibrated frequency-modulated continuous-wave (FMCW) radar transceivers. The authors propose two measurement setups: one with a high-gain dielectric lens antenna for collimated wavefronts and another with an elliptical mirror for focused beam measurements. Both setups enable fast and accurate material property extraction, including complex permittivity and loss tangent. The calibration process adapts vector network analyzer (VNA) techniques to FMCW systems, addressing challenges such as phase accuracy and systematic errors. A model-based optimization algorithm extracts material parameters by minimizing discrepancies between measured and theoretical reflection coefficients. The method is validated using well-known materials (e.g., PTFE, PVC, acrylic glass) and 3D-printed polylactide (PLA), demonstrating agreement with literature values. The mirror-based setup achieves higher dynamic range and accuracy by reducing multiple reflections. The study highlights the potential of FMCW radar for industrial applications, particularly where compact, cost-effective solutions are preferred over traditional VNAs.

The paper by Abouzaid et al. (2022) presents a deep learning-based method for characterizing dielectric materials using frequency-modulated continuous-wave (FMCW) radar, enhanced by open-set recognition (OSR) techniques. The authors propose a calibrated FMCW radar system operating in the D-band (126–182 GHz) to measure complex-valued reflection coefficients, offering a cost-effective alternative to vector network analyzers (VNAs). The calibration process involves compensating for systematic errors, waveguide dispersion, and signal distortions using MATCH and SHORT measurements. To address the complexity of material parameter extraction (thickness d, permittivity ε_r, and loss tangent tanδ), the authors employ KK-means clustering to reduce the classification space, grouping similar reflection coefficient curves into clusters. A neural network (NN) model is developed, combining a modified Class Anchor Clustering (CAC) loss function for OSR—enabling rejection of unknown materials—and a regression layer for tanδ prediction. The model's architecture includes complex-valued convolutional layers to process magnitude and phase data. Experimental validation on materials like polyethylene (PE), acrylic, and PVC demonstrates high accuracy, with results closely matching VNA-based references. The proposed approach outperforms traditional regression models, which struggle with generalization and require extensive training data. Key innovations include the integration of OSR for robustness, clustering to simplify classification, and a hybrid NN design that balances precision and computational efficiency. This method is particularly valuable for industrial applications, such as quality control in additive manufacturing, where rapid, non-destructive material characterization is critical.

The paper by Baer et al. (2015) presents a contactless method for detecting state parameter fluctuations (concentration, pressure, and temperature) in gaseous media using a millimeter-wave (mm-wave) frequency-modulated continuous-wave (FMCW) radar system. The authors derive dielectric mixing equations to relate gas permittivity to concentration and pressure, demonstrating that temperature has a negligible influence on permittivity due to the counteracting effects of displacement and orientation polarization. A pressure-resistant test container was designed to validate the theory, equipped with borosilicate glass windows, heating elements, and precision sensors for controlled experiments. The radar system operates at 80 GHz with a 25 GHz bandwidth, achieving micrometer-level accuracy in time-of-flight (TOF) measurements. Key innovations include a pseudotransmission technique using a transpolarizing reflector to isolate the gas permittivity signal and a phase-based approach for high-sensitivity detection of small permittivity changes. Experimental results confirm linear permittivity-pressure dependence (0.5% error) and distinct permittivity-concentration responses for gases like CO_2, N_2, and Ar, while temperature-induced permittivity variations were below detectable limits. The system's theoretical sensitivity for pressure fluctuations is 2.6 millibar, making it suitable for industrial applications such as gas flow metering and leakage detection in hazardous environments. The study establishes mm-wave radar as a robust, non-invasive tool for monitoring gas state parameters, with potential extensions to multiphase flow and process control.

The paper by Charvat et al. (2010) presents a through-dielectric radar imaging system based on a low-power, ultrawideband (UWB) frequency-modulated continuous-wave (FMCW) radar operating at S-band (1.926–4.069 GHz). The system addresses the challenge of imaging targets behind lossy dielectric slabs (e.g., concrete, drywall) by employing a modified FMCW architecture that range-gates out the dominant air-slab reflection, enabling high dynamic range and sensitivity for detecting low radar cross-section (RCS) targets. The radar uses long-duration (10 ms) chirps for pulse compression, and is mounted on a 2.44 m linear rail for synthetic aperture radar (SAR) imaging. A key innovation is the use of high-Q IF bandpass filters to isolate target returns behind the slab, overcoming ADC dynamic range limitations. Theoretical models and simulations validate the approach, showing minimal image distortion from the slab at stand-off ranges (≥6 m), with primary signal degradation arising from two-way attenuation. Experimental results demonstrate successful imaging of small targets (e.g., 0.95 cm diameter rods) behind a 10 cm concrete slab, as well as free-space imaging with transmit power as low as 5 pW. The system's performance is comparable to UWB pulsed radars but with lower hardware complexity (16-bit ADC at 200 KSPS) and power requirements (10 mW peak). Applications include through-wall surveillance, RCS measurements, and low-probability-of-detection radar.

The paper titled "Smoke Detection and Combustion Analysis Using Millimeter-Wave Radar Measurements" by Schenkel et al. (2024). It explores the application of frequency-modulated continuous-wave (FMCW) radar sensors operating in the millimeter-wave (mmWave) range (70–90 GHz) for detecting smoke and analyzing combustion processes. Traditional smoke detectors, which rely on optical sensors, are prone to high false alarm rates, especially in environments with dust or humidity. The authors propose radar-based detection as a robust alternative, capable of functioning effectively in smoke-obscured environments where optical systems fail. The study is grounded in dielectric models of smoke, which is treated as a gas-particle mixture with minimal variations in dielectric properties at mmWave frequencies. The authors employ phase-based radar signal processing to detect these subtle changes, leveraging the high sensitivity of phase measurements to small dielectric perturbations. The paper is structured into several sections. Section I introduces the challenges of fire detection, highlighting the limitations of optical systems and the potential of radar sensors for imaging, material characterization, and life-sign detection in smoke-filled environments. Section II delves into the dielectric properties of smoke, breaking it down into three components: gas mixtures, particulates, and temperature. The authors use the Debye equation and electromagnetic mixing formulas to model the refractive index of smoke, accounting for polar and nonpolar molecules, particle inclusions, and temperature effects. Simulations demonstrate how refractivity changes with gas composition (e.g., O_2, CO_2, H_2O) and temperature, showing that humid air significantly impacts refractivity due to water vapor's polar nature. Section III describes the experimental setups, including a laminar flow smoke duct compliant with the EN54-7 standard, a turbulent flow scenario using a smoke generator in an open room, and realistic test fires (TF4 and TF5) in a fire detection laboratory. The radar sensor, operating at 70–90 GHz with a range resolution of 7.5 mm, uses combined frequency- and phase-based signal processing to achieve high sensitivity. The phase difference between reference (clean air) and smoke-affected measurements is used to calculate changes in the refractive index, enabling precise smoke detection. Section IV presents the results. In laminar flow experiments, the radar phase measurements correlate well with optical extinction values, confirming the method's accuracy. Turbulent flow measurements reveal fluctuating phase patterns, reflecting the dynamic nature of smoke dispersion. Test fires (TF4: polyurethane foam; TF5: n-heptane) show distinct phase patterns corresponding to combustion behavior, with TF5 exhibiting larger phase shifts due to higher heat output. The radar's ability to detect ventilation-induced smoke redistribution is also demonstrated. The paper concludes that mm Wave radar sensors offer significant advantages for smoke detection and fire characterization, particularly in harsh environments where optical systems fail. While not replacing traditional smoke detectors, radar complements them by providing real-time insights into fire dynamics, such as flame spread and smoke density changes. The authors suggest future work on integrating radar with other sensors to enhance emergency response systems. The study underscores the potential of radar technology for improving fire safety through advanced, reliable detection and analysis.

The paper titled "A Study of FMCW Radar For the Detection of Water Level Inside a Wine Jar" by Min Wang et al. (2012). investigates the feasibility of using Frequency-Modulated Continuous-Wave (FMCW) radar to measure liquid levels in wine jars sealed with wooden covers, eliminating the need for manual inspection or intrusive sensors. The study focuses on modeling the electromagnetic interactions between radar waves and the layered media (air, wood, and wine) by analyzing reflection, transmission loss, and attenuation effects. The authors derive key equations for attenuation loss and reflection coefficients to quantify signal degradation through the wooden cover and wine. Simulations reveal that while high-frequency waves (>100 MHz) experience significant attenuation in wine (3 dB loss), the wooden cover introduces minimal loss (~0.08 dB), making FMCW radar viable for this application. A radar system model (10 GHz center frequency, 4 GHz bandwidth) demonstrates clear distinction between reflections from the wooden cover and liquid surface, though the former dominates the echo signal. In **Figure 2.9** below the experiment setup is shown:

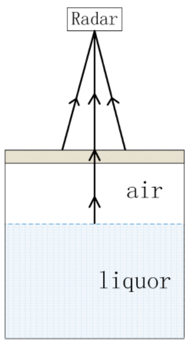

Figure 2.9. FMCW for the level detection inside a wine jar through wood cover

In **Figure 2.9** above, We can see at the top the radar is mounted to transmit and receive the electromagnetic wave, below that radar a tank is placed and covered with a

wooden cover and inside that tank there is liquor layer on the bottom and a space of air above.
The study concludes that FMCW radar can effectively penetrate wooden covers to measure liquid levels, providing a non-invasive solution for industrial wine storage monitoring.

3 MATERIAL AND METHOD

3.1 Wave Propagation and Polarization

3.1.1 Introduction

The foundation for this section rests on the vector wave equations derived for lossless and lossy media. The primary goal is the derivation of expressions for TEM waves traveling along principal axes and at oblique angles, along with the associated field parameters

3.1.2 Transverse Electromagnetic Modes

TEM modes are characterized by the electric field (E) and magnetic field (H) lying entirely in the plane transverse to the direction of propagation.

3.1.2.1 Uniform Plane Waves in an Unbounded Lossless Medium—Principal Axis

The analysis of a uniform plane wave traveling in an unbounded, lossless medium begins by satisfying Maxwell's equations for time-harmonic fields or the corresponding wave equations.

3.1.2.1.1 Electric and Magnetic Fields

Assuming an electric field polarized along the $\hat{x}$ direction and propagating along the $\hat{z}$ direction, the general expression for the complex electric field is given as

$$E_x(z) = E_0^+ e^{-j\beta z} + E_0^- e^{+j\beta z} \tag{3.1}$$

The corresponding magnetic field components (H) must be determined such that E, H, and the direction of propagation form a right-hand triplet. For the component traveling in the +z direction, H^+ is along $\hat{y}$, and for the component traveling in the $-z$ direction, H^- is along $-\hat{y}$. The total magnetic field is:

$$H_y(z) = H^+ + H^- = \frac{1}{\eta_0}\left(E_0^+ e^{-j\beta z} - E_0^- e^{+j\beta z}\right) \tag{3.2}$$

3.1.2.1.2 Wave Impedance

The wave impedance (Z_w) for a TEM wave is defined as the ratio of the orthogonal electric field component to the magnetic field component. For a lossless medium, the wave impedance is equal to the intrinsic impedance (η) of the medium:

$$Z_w = \eta = \sqrt{\frac{\mu}{\varepsilon}} \tag{3.3}$$

In the case of free space, the intrinsic impedance (η_0) is approximately 377 ohms:

$$\eta_0 = \sqrt{\frac{\mu_0}{\varepsilon_0}} \approx 377 \text{ ohms} \tag{3.4}$$

3.1.2.1.3 *Phase and Energy (Group) Velocities, Power, and Energy Densities*

The expressions for the electric and magnetic fields, as presented in equations (3.1) and (3.2), describe the spatial variations of the field intensities. The instantaneous electric field can be written as

$$\mathcal{E}_x(z,t) = \mathcal{E}_x^+(z,t) + \mathcal{E}_x^-(z,t) \tag{3.5}$$

$$\mathcal{E}_x(z,t) = E_0^+ \cos(\omega t - \beta z) + E_0^- \cos(\omega t + \beta z) \tag{3.6}$$

Similarly, the instantaneous magnetic field is expressed as

$$H_y(z,t) = H_y^+(z,t) + H_y^-(z,t) \tag{3.7}$$

$$H_y(z,t) = \frac{1}{\sqrt{\mu/\varepsilon}}[E_0^+ \cos(\omega t - \beta z) - E_0^- \cos(\omega t + \beta z)] \tag{3.8}$$

In both field expressions, equations (3.7) and (3.8), the first term represents a wave propagating in the ($+z$) direction, while the second term represents a wave propagating in the ($-z$) direction. the velocity must satisfy

The quantity (v_p^+) is known as the phase velocity, representing the velocity required to

$$v_p^+ = \frac{dz}{dt} = \frac{\omega}{\beta} = \frac{1}{\sqrt{\mu\varepsilon}} \tag{3.9}$$

remain in phase with a constant phase front of the wave.

It should be noted that for obliquely propagating waves, the phase velocity may exceed the velocity of light; however, this is a purely hypothetical speed.

3.1.3 Transverse Electromagnetic Modes in Lossy Media

In lossy media, electromagnetic waves experience attenuation in addition to phase accumulation. To account for this, the propagation constant is represented as a complex quantity $\gamma = \alpha + j\beta$, where α is the attenuation constant and β is the phase constant

3.1.3.1 Uniform Plane Waves in an Unbounded Lossy Medium—Principal Axis

The electric field of a uniform plane wave traveling in the $\pm z$ direction in a lossy medium takes the form derived from (3.1):

(3.10)

$$\boldsymbol{E} = E_0^+ e^{-\alpha z} e^{-j\beta z} + \hat{\boldsymbol{x}} E_0^- e^{+\alpha z} e^{+j\beta z}\ \hat{a}_x \tag{3.11}$$

The wave impedance (Z_w) is equal to the intrinsic impedance of the lossy medium (η_c):

(3.12)

$$Z_w = \sqrt{\frac{j\omega\mu}{\sigma + j\omega\varepsilon}} = \eta_c \quad (3.13)$$

The average power density (S_a^+) for the positive traveling wave is given by:

(3.14)

$$\boldsymbol{S}_a^+ = \frac{1}{2}\mathrm{Re}(\boldsymbol{E}^+ \times \boldsymbol{H}^+) \quad (3.15)$$

The relative magnitudes of conduction current density ($J_c = \sigma E$) and displacement current density ($J_d = j\omega\varepsilon E$) are critical for classifying the medium.

3.1.3.1.1 Good Dielectrics [$(\sigma/\omega\varepsilon)^2 \ll 1$]

For good dielectrics, displacement current density (J_d) is much greater than conduction current density (J_c). The phase constant (β) is approximated by:

(3.16)

$$\beta \approx \omega\sqrt{\mu\varepsilon} \quad (3.17)$$

The wave intrinsic impedance (η_c) simplifies the lossless form:

(3.18)

$$Z_w = \eta_c \approx \sqrt{\frac{\mu}{\varepsilon}} \quad (3.19)$$

The skin depth (δ) is approximated by:

(3.20)

$$\delta = \frac{1}{\alpha} \approx \frac{2}{\sigma}\sqrt{\frac{\varepsilon}{\mu}} \quad (3.21)$$

3.1.3.1.2 Good Conductors [$(\sigma/\omega\varepsilon)^2 \gg 1$]

For good conductors, where ($(\sigma/\omega\varepsilon)^2 \gg 1$), the exact expression for the attenuation constant given by equation (3.21) can be expanded using the binomial theorem. This yields

$$\alpha = \omega\sqrt{\mu\varepsilon}\left[\frac{1}{2}\left(\sqrt{1 + \left(\frac{\sigma}{\omega\varepsilon}\right)^2} - 1\right)\right]^{1/2} \quad (3.22)$$

Applying a binomial expansion for large ($\sigma/\omega\varepsilon$) which finally can be approximated by

$$\alpha \approx \omega\sqrt{\mu\varepsilon}\left(\frac{1}{2}\frac{\sigma}{\omega\varepsilon}\right)^{1/2} = \sqrt{\frac{\omega\mu\sigma}{2}} \quad (3.23)$$

Following a similar procedure, the corresponding phase constant of equation (4-28d) can be approximated as

$$\beta \approx \sqrt{\frac{\omega\mu\sigma}{2}} \quad (3.24)$$

which is identical in form to the approximate expression for the attenuation constant given by equation (4-40a).

For good conductors, the wave impedance or intrinsic impedance from equation (4-30) can be approximated as

$$Z_w = \eta_c = \sqrt{\frac{j\omega\mu}{\sigma + j\omega\varepsilon}} \approx \sqrt{\frac{j\omega\mu}{\sigma}} = (1+j)\sqrt{\frac{\omega\mu}{2\sigma}} \quad (3.25)$$

The real and imaginary parts of this impedance are equal in magnitude.

Under the same conditions, the skin depth (δ) is defined as the reciprocal of the attenuation constant, i.e.,

$$\delta = \frac{1}{\alpha} \approx \sqrt{\frac{2}{\omega\mu\sigma}} \quad (3.26)$$

This is the most widely recognized and commonly used expression for the skin depth in good conductors.

3.1.4 Polarization

Polarization refers to the curve traced at a given observation point, as a function of time, by the tip of the arrow representing the instantaneous electric field vector. The field must be observed along the direction of propagation. Polarization may be classified into three fundamental categories: (linear, circular and elliptical). If the electric field vector at a fixed point in space remains directed along a single straight line that is perpendicular to the direction of propagation, the wave is said to be (linearly polarized).

In the general case, however, the tip of the electric field vector traces an ellipse over time, and the field is said to be (elliptically polarized). The rotation of the electric field vector may occur in either a clockwise (CW) or counterclockwise (CCW) sense when viewed in the direction of propagation.

3.1.4.1 Linear Polarization

Consider a harmonic plane wave with components of the electric field, propagating in the positive $(+z)$ direction (into the page), The instantaneous electric and magnetic fields can be expressed as:

$$\boldsymbol{E} = \widehat{\boldsymbol{a}_x \mathcal{E}_x} + \widehat{\boldsymbol{a}_y \mathcal{E}_y} = \mathrm{Re}\{\widehat{\boldsymbol{a}_x} E_x^+ e^{j(\omega t - \beta z)} + \widehat{\boldsymbol{a}_y} E_y^+ e^{j(\omega t - \beta z)}\} \tag{3.27}$$

$$\boldsymbol{H} = \widehat{\boldsymbol{a}_y \mathcal{H}_y} + \widehat{\boldsymbol{a}_x \mathcal{H}_x} = \mathrm{Re}\left\{\widehat{\boldsymbol{a}_y} \frac{E_x^+}{\eta} e^{j(\omega t - \beta z)} - \widehat{\boldsymbol{a}_x} \frac{E_y^+}{\eta} e^{j(\omega t - \beta z)}\right\} \tag{3.28}$$

where (E_x^+) and (E_y^+) are complex phasor amplitudes, and (E_{x0}^+) and (E_{y0}^+) are their corresponding real magnitudes. Thus, the instantaneous form of the electric field can be written as:

$$\boldsymbol{E} = \widehat{\boldsymbol{a}_x} E_{x0}^+ \cos(\omega t - \beta z + \phi_x) + \widehat{\boldsymbol{a}_y} E_{y0}^+ \cos(\omega t - \beta z + \phi_y) \tag{3.29}$$

To examine the time variation of the instantaneous electric field vector (E), we consider the plane $(z = 0)$ for convenience. Other planes may be analyzed similarly.

Let

$$[E_{y0}^+ = 0] \tag{3.30}$$

Then,

$$\mathcal{E}_x = E_{x0}^+ \cos(\omega t + \phi_x) \tag{3.31}$$

$$\mathcal{E}_y = 0 \tag{3.32}$$

Hence, the locus of the instantaneous electric field vector is:

$$\boldsymbol{E} = \widehat{\boldsymbol{a}_x} E_{x0}^+ \cos(\omega t + \phi_x) \tag{3.33}$$

which represents a straight line directed along the (x) axis at all times, Therefore, the field is said to be linearly polarized in the (x) direction. It follows from the above discussion that a time-harmonic field is linearly polarized at a given point in space if the electric (or magnetic) field vector at that point is oriented along the same straight line at every instant of time.

3.1.4.2 Circular Polarization

A wave is said to be circularly polarized if the tip of its electric field vector traces a circular locus in space. At any instant of time, the electric field intensity of such a wave has a constant magnitude, while its orientation in space changes continuously with time to describe a circular path.

3.1.4.2.1 Right-Hand (Clockwise) Circular Polarization

A wave is said to have right-hand circular polarization (RHCP) if its electric field vector rotates in a clockwise sense when viewed along the direction of propagation.

For the wave to be circularly polarized, the electric field vector must maintain a constant magnitude and describe a circular trajectory in space.

Consider again the instantaneous electric field vector (E) at the $(z = 0)$ plane

For this example, let the following conditions hold:

$$[\phi_x = 0, \quad \phi_y = -\frac{\pi}{2}, \quad E_{x0}^{+} = E_{y0}^{+} = E_R] \tag{3.34}$$

Then, the instantaneous field components are

$$\mathcal{E}_x = E_R \cos(\omega t) \tag{3.35}$$

$$\mathcal{E}_y = E_R \cos\left(\omega t - \frac{\pi}{2}\right) = E_R \sin(\omega t) \tag{3.36}$$

The magnitude of the total electric field vector is therefore

$$\mathcal{E} = \sqrt{\mathcal{E}_x^2 + \mathcal{E}_y^2} = E_R\sqrt{\cos^2(\omega t) + \sin^2(\omega t)} = E_R \tag{3.37}$$

Thus, the amplitude of the electric field remains constant, and the tip of the vector describes a circle of radius (E_R).

The instantaneous direction of the electric field vector makes an angle (ψ) with the (x) axis, given by:

$$\psi = \tan^{-1}\left(\frac{\mathcal{E}_y}{\mathcal{E}_x}\right) = \tan^{-1}\left(\frac{E_R \sin(\omega t)}{E_R \cos(\omega t)}\right) = \tan^{-1}[\tan(\omega t)] = \omega t \tag{3.38}$$

If the locus of (E) is plotted for successive instants of time at the $(z = 0)$ plane, it forms a circle of radius (E_R) rotating clockwise with angular frequency (ω). Hence, the wave is said to have right-hand circular polarization. Note that the rotation is always viewed from the rear of the wave—i.e., looking in the direction of propagation, since the wave propagates in the $(+z)$ direction (into the page), the rotation appears clockwise to an observer looking into the page. It is evident that there exists a $(90°)$ phase difference between the two orthogonal components of the electric field vector, and their equal amplitudes produce a uniform circular rotation of the resultant field.

3.1.4.2.2 Left-Hand (Counterclockwise) Circular Polarization

A wave is said to have left-hand circular polarization (LHCP) if the tip of its electric field vector rotates in a counterclockwise sense when viewed along the direction of propagation. Consider again the instantaneous electric field vector (E) at the $(z = 0)$ plane, For this example, let the following conditions hold:

$$[\phi_x = 0, \quad \phi_y = \frac{\pi}{2}, \quad E_{x0}^{+} = E_{y0}^{+} = E_L] \tag{3.39}$$

Then, the instantaneous components of the electric field are

$$\mathcal{E}_x = E_L \cos(\omega t) \tag{3.40}$$

$$\mathcal{E}_y = E_L \cos\left(\omega t + \frac{\pi}{2}\right) = -E_L \sin(\omega t) \tag{3.41}$$

The magnitude of the electric field vector is constant:

$$|\boldsymbol{E}| = \sqrt{\mathcal{E}_x^2 + \mathcal{E}_y^2} = E_L\sqrt{\cos^2(\omega t) + \sin^2(\omega t)} = E_L \tag{3.42}$$

The instantaneous angle (ψ) of the electric field vector with respect to the (x) axis is

$$\psi = \tan^{-1}\left(\frac{\mathcal{E}_y}{\mathcal{E}_x}\right) = \tan^{-1}\left(\frac{-E_L \sin(\omega t)}{E_L \cos(\omega t)}\right) = -\omega t \tag{3.43}$$

Thus, the tip of the electric field vector traces a circle of radius (E_L) and rotates counterclockwise with angular frequency (ω). Hence, the wave is said to have left-hand circular polarization.

The instantaneous electric field vector may also be expressed in complex form as

$$\mathcal{E} = \mathrm{Re}[\widehat{\boldsymbol{a}_x} E_L e^{j(\omega t - \beta z)} + \widehat{\boldsymbol{a}_y} E_L e^{j(\omega t - \beta z + \pi/2)}] = E_L \mathrm{Re}\left(\widehat{\boldsymbol{a}_x} + j\widehat{\boldsymbol{a}_y}\right) e^{j(\omega t - \beta z)} \tag{3.44}$$

In equation (3.44), there is a (90°) phase advance of the $(\mathcal{E}_y)$ component relative to the $(\mathcal{E}_x)$ component, which results in counterclockwise rotation of the electric field vector.

From the previous discussion, we see that left-hand circular polarization (LHCP) is achieved if and only if the two orthogonal components of the electric field have equal amplitudes and a phase difference equal to an odd multiple of (90°) between one component and the other. The sense of rotation (counterclockwise for LHCP) is determined by the rotation of the phase-leading component. The rotation of the field must always be observed in the direction away from the observer, i.e., along the propagation of the wave. The necessary and sufficient conditions for circular polarization are therefore:

1. The electric field must have two orthogonal, linearly polarized components.
2. The two components must have equal magnitudes.

3. The two components must have a time-phase difference equal to odd multiples of $(90°)$.

The sense of rotation is always determined by rotating the phase-leading component toward the phase-lagging component and observing the rotation as the wave propagates away from the observer.

The rotation should follow the angular separation between the two components that is less than $(180°)$.

3.2 Reflection and Transmission

3.2.1 Introduction

In the previous section, we discussed solutions for TEM waves in unbounded media.

In practical problems, however, the fields encounter boundaries, scatterers, and other discontinuities. Therefore, the fields must be determined by taking into account these interfaces and obstacles. In this section, we focus on TEM field solutions in two semi-infinite media (both lossless and lossy) separated by a planar boundary of infinite extent. Reflection and transmission coefficients will be derived to account for the partial reflection and transmission of fields at the boundary These coefficients are functions of:

1. The constitutive parameters of the two media ((ε, μ, σ)),
2. The direction of wave propagation (angle of incidence),
3. The direction of the electric and magnetic fields (wave polarization).

In general, the reflection and transmission coefficients are complex quantities.

It will be shown that both their magnitudes and phases can be controlled by varying the angle of incidence of the wave. For a particular wave polarization (known as parallel polarization), the reflection coefficient can be made equal to zero. The corresponding angle of incidence is referred to as the Brewster angle. This principle is widely used in the design of optical instruments, such as binoculars and anti-reflection coatings. Conversely, the magnitude of the reflection coefficient can be made equal to unity by selecting an appropriate angle of incidence. This angle is known as the critical angle, which is independent of the wave polarization. For the critical angle to exist, the incident wave must propagate in the denser medium. This concept plays a crucial role in the design of transmission lines and waveguiding structures, including:

- Optical fibers,
- Slab waveguides,
- Coated conductors, and
- Microstrip lines.

3.2.2 Reflection and Transmission at a Planar Interface: Normal Incidence

We begin the discussion of wave reflection and transmission at planar boundaries of lossless media by considering a plane wave incident normally (perpendicular) to the interface between two semi-infinite, lossless media.

The media are characterized by their constitutive parameters (ε_1, μ_1) and (ε_2, μ_2).

When the incident wave encounters the interface, part of the wave is reflected into medium 1, and part is transmitted into medium 2. Assuming the incident electric field has amplitude (E_0) and is polarized along the (x) axis, the incident, reflected, and transmitted electric fields can be expressed as:

$$E_i = \widehat{a_x} E_0 e^{-j\beta_1 z} \tag{3.45}$$

$$E_r = \widehat{a_x} \Gamma E_0 e^{j\beta_1 z} \tag{3.46}$$

$$E_t = \widehat{a_x} T E_0 e^{-j\beta_2 z} \tag{3.47}$$

Here, (Γ) and (T) are the reflection and transmission coefficients, respectively, which are initially unknown. Since the incident field is linearly polarized and the interface is planar, the reflected and transmitted fields will also be linearly polarized along the same axis. Any difference in direction or sign will be accounted for by the appropriate sign of the coefficients. Using the right-hand rule or Maxwell's equations, the corresponding magnetic field components are

$$H_i = \widehat{a_y} \frac{E_0}{\eta_1} e^{-j\beta_1 z} \tag{3.48}$$

$$H_r = -\widehat{a_y} \frac{\Gamma E_0}{\eta_1} e^{j\beta_1 z} \tag{3.49}$$

$$H_t = \widehat{a_y} \frac{T E_0}{\eta_2} e^{-j\beta_2 z} \tag{3.50}$$

The reflection and transmission coefficients are determined by enforcing the continuity of the tangential components of the electric and magnetic fields at the interface $((z = 0))$:

$$E_i + E_r = E_t \quad \Rightarrow \quad E_0 + \Gamma E_0 = T E_0 \tag{3.51}$$

$$H_i + H_r = H_t \quad \Rightarrow \quad \frac{E_0}{\eta_1} \frac{\Gamma E_0}{\eta_1} = \frac{T E_0}{\eta_2} \tag{3.52}$$

Solving for (Γ) and (T) yields:

$$\Gamma = \frac{\eta_2 - \eta_1}{\eta_2 + \eta_1} = \frac{E_r}{E_i} \tag{3.53}$$

a

$$T = \frac{2\eta_2}{\eta_1 + \eta_2} = \frac{E_t}{E_i} \quad (3.54)$$

Thus, the reflection and transmission coefficients for a planar interface under normal incidence depend only on the intrinsic impedances of the two media.

The reflection coefficient is zero only if ($\eta_2 = \eta_1$), which for most dielectrics implies ($\varepsilon_2 = \varepsilon_1$) assuming ($\mu_1 = \mu_2$).At distances ($z_1$) and ($z_2$) away from the interface in media 1 and 2, respectively, the reflected and transmitted fields are

$$E_r(z_1) = \Gamma E_0 e^{j\beta_1 z_1}, \quad z_1 > 0 \quad (3.55)$$

$$E_t(z_2) = T E_0 e^{-j\beta_2 z_2}, \quad z_2 > 0 \quad (3.56)$$

The corresponding time-averaged Poynting vectors are

$$S_{i,\mathrm{a}} = \frac{1}{2}\mathrm{R}\{E_i \times H_i^*\} = \widehat{a_z}\frac{|E_0|^2}{2\eta_1} \quad (3.57)$$

$$S_{r,\mathrm{a}} = \frac{1}{2}\mathrm{R}\{E_r \times H_r^*\} = -\widehat{a_z}\frac{|\Gamma|^2|E_0|^2}{2\eta_1} \quad (3.58)$$

$$S_{t,\mathrm{a}} = \frac{1}{2}\mathrm{R}\{E_t \times H_t^*\} = \widehat{a_z}\frac{|T|^2|E_0|^2}{2\eta_2} = \widehat{a_z}\frac{\eta_1}{\eta_2}|T|^2\frac{|E_0|^2}{2\eta_1} \quad (3.59)$$

It is important to note:

- The ratio of reflected to incident power densities equals ($|\Gamma|^2$).
- The ratio of transmitted to incident power densities is not simply ($|T|^2$), but is weighted by the intrinsic impedances of the media ((η_1, η_2)).
- While the transmitted field magnitude may exceed the incident field, the transmitted power cannot exceed the incident power due to conservation of energy.

3.2.3 Oblique Incidence — Lossless Media

To analyze reflection and transmission at oblique wave incidence, we introduce the plane of incidence, defined as the plane formed by the unit vector normal to the reflecting interface and the wave vector of incidence. For a wave incident in the xz plane on an interface parallel to the xy plane, the plane of incidence is the xz plane.

For general wave polarization, it is convenient to decompose the electric field into components perpendicular and parallel to the plane of incidence, and analyze each individually.The total reflected and transmitted fields are obtained as the vector sum of these components.

3.2.3.1 Perpendicular (Horizontal or E) Polarization

If the electric field is perpendicular to the plane of incidence, the polarization is called perpendicular (or horizontal, E-polarization). The incident electric and magnetic fields can be expressed as:

$$E_i^{\perp} = \widehat{a_y} E_0 e^{-j\beta_i \cdot r} = \widehat{a_y} E_0 e^{-j\beta_1 (x \sin\theta_i + z\cos\theta_i)} \tag{3.60}$$

$$H_i^{\perp} = (-\widehat{a_x}\cos\theta_i + \widehat{a_z}\sin\theta_i)\frac{E_0}{\eta_1} e^{-j\beta_1 (x \sin\theta_i + z\cos\theta_i)} \tag{3.61}$$

Similarly, the reflected fields are

$$E_r^{\perp} = \widehat{a_y}\Gamma_{\perp} E_0 e^{-j\beta_1 (x \sin\theta_r - z\cos\theta_r)} \tag{3.62}$$

$$H_r^{\perp} = (\widehat{a_x}\cos\theta_r + \widehat{a_z}\sin\theta_r)\frac{\Gamma_{\perp} E_0}{\eta_1} \tag{3.63}$$

The transmitted fields are

$$E_t^{\perp} = \widehat{a_y} T_{\perp} E_0 e^{-j\beta_2 (x \sin\theta_t + z\cos\theta_t)} \tag{3.64}$$

$$H_t^{\perp} = (-\widehat{a_x}\cos\theta_t + \widehat{a_z}\sin\theta_t)\frac{T_{\perp} E_0}{\eta_2} \tag{3.65}$$

Applying boundary conditions on the tangential components at $z = 0$, we obtain

$$E_i^{\perp} + E_r^{\perp} = E_t^{\perp} \tag{3.66}$$

$$H_i^{\perp} + H_r^{\perp} = H_t^{\perp} \tag{3.67}$$

Solving for the Fresnel coefficients gives:

$$\Gamma_{\perp} = \frac{\eta_2\cos\theta_i - \eta_1\cos\theta_t}{\eta_2\cos\theta_i + \eta_1\cos\theta_t} \tag{3.68}$$

$$T_{\perp} = \frac{2\eta_2\cos\theta_i}{\eta_2\cos\theta_i + \eta_1\cos\theta_t} \tag{3.69}$$

where $\theta_r = \theta_i$ and $\beta_1\sin\theta_i = \beta_2\sin\theta_t$ (Snell's laws of reflection and refraction).

The total electric field in medium 1 is

$$E_1^{\perp} = E_i^{\perp} + E_r^{\perp} \tag{3.70}$$

$$= \widehat{a_y} E_0 e^{-j\beta_1 (x \sin\theta_i + z\cos\theta_i)}\left[1 + \Gamma_{\perp} e^{j2\beta_1 z\cos\theta_i}\right] \tag{3.71}$$

3.2.3.2 Parallel (Vertical or H) Polarization

If the electric field is parallel to the plane of incidence, the polarization is called parallel (or vertical, H-polarization). The incident fields are

$$E_i^{\parallel} = (\widehat{a_x}\cos\theta_i - \widehat{a_z}\sin\theta_i)E_0\Gamma^{\parallel}\, e^{-j\beta_1(x\sin\theta_i + z\cos\theta_i)} \tag{3.72}$$

$$H_i^{\parallel} = \widehat{a_y}\frac{E_0}{\eta_1}e^{-j\beta_1(x\sin\theta_i + z\cos\theta_i)} \tag{3.73}$$

The reflected and transmitted fields are

$$E_r^{\parallel} = (\widehat{a_x}\cos\theta_r + \widehat{a_z}\sin\theta_r)b_{\parallel}E_0e^{-j\beta_1(x\sin\theta_r - z\cos\theta_r)} \tag{3.74}$$

$$H_r^{\parallel} = -\widehat{a_y}\frac{b_{\parallel}E_0}{\eta_1} \tag{3.75}$$

$$E_t^{\parallel} = (\widehat{a_x}\cos\theta_t - \widehat{a_z}\sin\theta_t)T_{\parallel}E_0e^{-j\beta_2(x\sin\theta_t + z\cos\theta_t)} \tag{3.76}$$

$$H_t^{\parallel} = \widehat{a_y}\frac{T_{\parallel}E_0}{\eta_2} \tag{3.77}$$

Solving the boundary conditions at $z = 0$ yields the Fresnel coefficients:

$$\Gamma_{\parallel} = \frac{\eta_2\cos\theta_t - \eta_1\cos\theta_i}{\eta_2\cos\theta_t + \eta_1\cos\theta_i} \tag{3.78}$$

$$T_{\parallel} = \frac{2\eta_2\cos\theta_i}{\eta_2\cos\theta_t + \eta_1\cos\theta_i} \tag{3.79}$$

The total electric field in medium 1 is

$$E_1^{\parallel} = E_i^{\parallel} + E_r^{\parallel} \tag{3.80}$$

$$= (\widehat{a_x}\cos\theta_i - \widehat{a_z}\sin\theta_i)E_0e^{-j\beta_1(x\sin\theta_i + z\cos\theta_i)}\left[1 + \Gamma_{\parallel}e^{j2\beta_1 z\cos\theta_i}\right] \tag{3.81}$$

3.2.3.3 Brewster and Critical Angles

For parallel polarization, the reflection coefficient vanishes at a specific incident angle θ_B, called the Brewster angle, which increases with the ratio $\varepsilon_2/\varepsilon_1$. The critical angle θ_c occurs when the wave propagates from a denser to a rarer medium, and total internal reflection occurs for $\theta_i > \theta_c$. This angle is independent of polarization, although the reflection and transmission coefficients differ for perpendicular and parallel polarizations.

3.2.3.3.1 Perpendicular (Horizontal) Polarization}

For perpendicular polarization, the reflection coefficient $\Gamma_{\perp}$ vanishes if

$$\Gamma_{\perp} = \frac{\eta_2 \cos\theta_i - \eta_1 \cos\theta_t}{\eta_2 \cos\theta_i + \eta_1 \cos\theta_t} = 0 \tag{3.82}$$

which leads to

$$\eta_2 \cos\theta_i = \eta_1 \cos\theta_t \tag{3.83}$$

Using Snell's law, $\beta_1 \sin\theta_i = \beta_2 \sin\theta_t$, we can write

$$\cos\theta_i = \frac{\mu_1}{\mu_2}\cos\theta_t\,, \quad \text{or equivalently,} \quad 1 - \sin^2\theta_i = \frac{\mu_1^2}{\mu_2^2}(1 - \sin^2\theta_t) \tag{3.84}$$

Since $\sin\theta_i \leq 1$, this condition exists only if

$$\frac{\varepsilon_2}{\varepsilon_1} \leq \frac{\mu_1}{\mu_2} \tag{3.85}$$

However, for most dielectric materials (excluding ferromagnetic), $\mu_1 \approx \mu_2 \approx \mu_0$, and therefore indicating that no real incidence angle exists for which the reflection coefficient vanishes for perpendicular polarization.

3.2.3.3.2 Parallel (Vertical) Polarization

For parallel polarization, the reflection vanishes if

$$\Gamma_{\parallel} = \frac{\eta_2 \cos\theta_t - \eta_1 \cos\theta_i}{\eta_2 \cos\theta_t + \eta_1 \cos\theta_i} = 0 \tag{3.86}$$

which gives the condition

$$\eta_2 \cos\theta_t = \eta_1 \cos\theta_i \tag{3.87}$$

Applying Snell's law, this reduces to

$$\sin\theta_i = \sqrt{\frac{\varepsilon_2}{\varepsilon_1} \cdot \frac{\mu_2}{\mu_1}(1 - \sin^2\theta_t)} \tag{3.88}$$

For most dielectrics, $\mu_1 = \mu_2$, and the Brewster angle exists only for parallel polarization:

$$\theta_i = \theta_B = \tan^{-1}\left(\sqrt{\frac{\varepsilon_2}{\varepsilon_1}}\right) \tag{3.89}$$

Alternative forms of the Brewster angle include:

$$\theta_B = \cos^{-1}\left(\frac{\varepsilon_1}{\varepsilon_1 + \varepsilon_2}\right) \tag{3.90}$$

$$\theta_B = \tan^{-1}\left(\frac{\varepsilon_2}{\varepsilon_1}\right) \tag{3.91}$$

Thus, the Brewster angle exists only for parallel (vertical) polarization, while it does not exist for perpendicular (horizontal) polarization under normal dielectric conditions.

3.2.3.4 Total Reflection – Critical Angle

We found the angles that allow total transmission for perpendicular and parallel polarizations. When the permeabilities of the two media are equal ($\mu_1 = \mu$), only parallel polarized fields can achieve total transmission at the Brewster angle θ_B. We now consider the conditions for total reflection, where the magnitude of the reflection coefficient is unity, $|b| = 1$.

3.2.3.4.1 Perpendicular (Horizontal) Polarization

For perpendicular polarization, the reflection coefficient magnitude is

$$|\Gamma_\perp| = \left|\frac{\eta_2 \cos\theta_i - \eta_1 \cos\theta_t}{\eta_2 \cos\theta_i + \eta_1 \cos\theta_t}\right| = 1 \tag{3.92}$$

This occurs if the second term in the numerator and denominator is imaginary. Using Snell's law,

$$\cos\theta_t = \sqrt{1 - \sin^2\theta_t} = \sqrt{1 - \frac{\mu_1\varepsilon_1}{\mu_2\varepsilon_2}\sin^2\theta_i} \tag{3.93}$$

The condition for total reflection defines the critical angle θ_c:

$$\theta_i \geq \theta_c = \sin^{-1}\sqrt{\frac{\mu_2\varepsilon_2}{\mu_1\varepsilon_1}} \tag{3.94}$$

For media with identical permeabilities ($\mu_1 = \mu_2$), this reduces to

$$\theta_i \geq \theta_c = \sin^{-1}\sqrt{\frac{\varepsilon_2}{\varepsilon_1}}, \quad \text{valid if } \varepsilon_2 \leq \varepsilon_1 \tag{3.95}$$

3.2.3.4.2 Parallel (Vertical) Polarization at the Critical Angle

The procedure used to derive the critical angle for perpendicular polarization can also be applied to parallel polarization. It can be shown that the critical angle is independent of polarization and exists for both parallel and perpendicular polarizations.

The only requirement is that the wave propagates from a denser to a less dense medium, i.e., $\mu_2\varepsilon_2 < \mu_1\varepsilon_1$ or $\varepsilon_2 < \varepsilon_1$ when $\mu_1 = \mu_2$

The critical angle for parallel polarization is the same as that for perpendicular polarization:

$$\theta_c = \sin^{-1}\sqrt{\frac{\varepsilon_2}{\varepsilon_1}} \quad (\mu_1 = \mu_2) \tag{3.96}$$

Wave propagation phenomena for $\theta_i < \theta_c$, $\theta_i = \theta_c$, and $\theta_i > \theta_c$ are identical to those described for perpendicular polarization. Although the specific formulas for the reflection and transmission coefficients, $b_{\parallel}$ and $T_{\parallel}$, and transmitted average power density $S_{t,\parallel}$ differ from their perpendicular counterparts, the underlying principles remain the same. The derivation of the parallel polarization formulas is left as an end-of-chapter exercise.

3.2.4 Lossy Media

Previously, wave reflection and transmission were examined under normal and oblique incidence assuming both media were lossless. Now we consider the case where one or both media are lossy. In some cases, the formulas are similar to the lossless case, but differences arise especially for oblique incidence.

3.2.4.1 Reflection Coefficient of a Single Slab Layer

For normal incidence at a single interface, the reflection coefficient is

$$\Gamma = \frac{\eta_2 - \eta_1}{\eta_2 + \eta_1} \tag{3.97}$$

At a distance $z = -d$ from the boundary, the reflection coefficient becomes

$$\Gamma(z = -d) = \Gamma e^{-j2\beta_1 d} \tag{3.98}$$

Just to the right of the boundary, the input impedance is

$$Z_{\text{in}}(z = 0^+) = \eta_2 \tag{3.99}$$

At $z = -d$, using the total fields,

$$E_{\text{total}}|_{z=-d} = E_i + E_r = E_0 e^{j\beta_1 d}\left(1 + \Gamma e^{-j2\beta_1 d}\right) \tag{3.100}$$

$$H_{\text{total}}|_{z=-d} = \frac{E_0}{\eta_1} e^{j\beta_1 d}\left(1 - \Gamma e^{-j2\beta_1 d}\right) \tag{3.101}$$

so that the input impedance at $z = -d$ is

$$Z_{\text{in}}|_{z=-d} = \eta_1 \frac{1 + \Gamma e^{-j2\beta_1 d}}{1 - \Gamma e^{-j2\beta_1 d}} = \eta_1 \frac{\eta_2 + j\eta_1 \tan(\beta_1 d)}{\eta_1 + j\eta_2 \tan(\beta_1 d)} \tag{3.102}$$

This is analogous to the well-known impedance transfer equation in transmission line theory.

3.2.4.2 Multiple Layer Interfaces

For multiple layers, the input impedance at $z = 0^+$ is equal to the intrinsic impedance of medium 3:

$$Z_{\text{in}}(z = 0^+) = \eta_3 \tag{3.103}$$

and the input reflection coefficient is

$$\Gamma_{\text{in}}(0^-) = \frac{\eta_3 - \eta_2}{\eta_3 + \eta_2} \tag{3.104}$$

At $z = -d$,

$$Z_{\text{in}}(z = -d^+) = \eta_2 \frac{(\eta_3 + \eta_2) + (\eta_3 - \eta_2)e^{-j2\beta_2 d}}{(\eta_3 + \eta_2) - (\eta_3 - \eta_2)e^{-j2\beta_2 d}} \tag{3.105}$$

$$\Gamma_{\text{in}}(z = -d^-) = \frac{Z_{\text{in}}(z = -d^+) - \eta_1}{Z_{\text{in}}(z = -d^+) + \eta_1} \tag{3.106}$$

Using the intrinsic reflection coefficients at each boundary, Γ_{12}, Γ_{23}, etc., the total input reflection coefficient can be written as a geometric series:

$$\Gamma_{\text{in}}(z = -d^-) = \Gamma_{12} + \frac{T_{12}T_{21}\Gamma_{23}e^{-j2\theta}}{1 - \Gamma_{21}\Gamma_{23}e^{-j2\theta}}, \quad \theta = \beta_2 d \tag{3.107}$$

Where:

$$\Gamma_{21} = -\Gamma_{12}, \quad T_{12} = 1 + \Gamma_{21}, \quad T_{21} = 1 + \Gamma_{12} \tag{3.108}$$

For small intrinsic reflection coefficients ($|\Gamma_{12}|, |\Gamma_{23}| \ll 1$), the approximation

$$\Gamma_{\text{in}}(z = -d^-) \approx \Gamma_{12} + \Gamma_{23}e^{-j2\beta_2 d} \tag{3.109}$$

gives accurate results with errors ≤ 4\% when $|\Gamma_{12}| = |\Gamma_{23}| \leq 0.2$, and is convenient for analyzing multiple interfaces.

The bandwidth of the response curve can be increased by flattening the curve near the center frequency f_0. This can be accomplished by increasing the number of layers bounded between the two semi-infinite media. For lossy media, the overall reflection and transmission coefficients can be expressed as

$$\Gamma_{\text{in}} = \frac{E_r}{E_i}, \qquad T = \frac{E_t}{E_i}, \qquad Z_{ij} = \frac{\mu_i \gamma_j}{\mu_j \gamma_i} \tag{3.110}$$

$$\gamma_k = \pm j\omega\mu_k(\sigma_k + j\omega\varepsilon_k), \quad i,j = 1,2,3. \tag{3.111}$$

These equations are valid for lossless, lossy, or mixed media.

3.2.4.3 Reflection Coefficient of Multiple Layers

For normal wave incidence, a single dielectric layer exhibits narrowband characteristics around f_0, similar to a single-section bandstop filter or quarter-wavelength transformer. To broaden the bandwidth, multiple dielectric slabs with different dielectric constants can be inserted between the semi-infinite media. Such multiple-section layers are widely used in dielectric filters or radar target coatings. For N layers of thicknesses $d_1, d_2, \dots, d_N$ and intrinsic impedances $\eta_1, \eta_2, \dots, \eta_N$, the input reflection coefficient at the leading interface can be approximated as:

$$\Gamma_{\text{in}} \approx \Gamma_0 + \Gamma_1 e^{-j2\beta_1 d_1} + \Gamma_2 e^{-j2(\beta_1 d_1 + \beta_2 d_2)} + \cdots + \Gamma_N e^{-j2(\beta_1 d_1 + \cdots + \beta_N d_N)} \tag{3.112}$$

where the intrinsic reflection coefficients are:

$$\Gamma_0 = \frac{\eta_1 - \eta_0}{\eta_1 + \eta_0}, \Gamma_1 = \frac{\eta_2 - \eta_1}{\eta_2 + \eta_1}, \Gamma_2 = \frac{\eta_3 - \eta_2}{\eta_3 + \eta_2}, \dots \Gamma_N = \frac{\eta_L - \eta_N}{\eta_L + \eta_N} \tag{3.113}$$

3.2.4.3.1 Quarter-Wavelength Transformer

For a single lossless dielectric slab of thickness $\lambda_0/4$ at frequency f_0 between two semi-infinite media, the input reflection coefficient at f_0 is zero if:

$$\eta_1 = \sqrt{\eta_0 \eta_L} \tag{3.114}$$

where η_1 is the intrinsic impedance of the dielectric slab, and η_0, η_L are the impedances of the input and load media, respectively. To increase bandwidth, multiple $\lambda/4$ sections can be used. The number of sections N and the intrinsic impedance of each section can be designed such that the reflection coefficient follows prescribed variations over the desired frequency range.

3.2.4.3.2 Binomial (Maximally Flat) Design

One method to design an N-section $\lambda/4$ transformer is to achieve a maximally flat passband. The junction reflection coefficients Γ_n are derived using the binomial expansion:

$$\Gamma_{\text{in}}(f) = \sum_{n=0}^{N} \Gamma_n e^{-j2n\theta} = e^{-jN\theta} \frac{\eta_L - \eta_0}{\eta_L + \eta_0} \tag{3.115}$$

$$\Gamma_n = 2^{-N}\binom{N}{n}\frac{\eta_L - \eta_0}{\eta_L + \eta_0} \tag{3.116}$$

Where:

$$\theta = \beta_n d_n = \frac{2\pi}{\lambda_n}\frac{\lambda_{n0}}{4} = \frac{\pi}{2}\frac{f_m}{f_0} \tag{3.117}$$

For a symmetrical transformer ($\Gamma_0 = \Gamma_N$, $\Gamma_1 = \Gamma_{N-1}$, etc.), the input reflection coefficient reduces to:

$$\Gamma_{\text{in}}(f) = 2e^{-jN\theta}[\Gamma_0 \cos N\,\theta + \Gamma_1 \cos(N-2)\,\theta + \Gamma_2 \cos(N-4)\,\theta + \cdots] \tag{3.118}$$

The fractional bandwidth f/f_0 corresponding to a maximum tolerable reflection coefficient Γ_m is given by:

$$\frac{f}{f_0} = 2\cos^{-1}[(\eta_L - \eta_0)/(\eta_L + \eta_0)]^{1/N} \tag{3.119}$$

The design procedure involves specifying:

- Load intrinsic impedance η_L
- Input intrinsic impedance η_0
- Number of sections N

Maximum tolerable reflection coefficient Γ_m or fractional bandwidth f/f_0

From these specifications, the intrinsic impedances of each section and the fractional bandwidth can be determined.

3.2.4.3.3Oblique-Wave Incidence

For oblique incidence on N layers of planar slabs, the reflection and transmission coefficients for perpendicular (horizontal) and parallel (vertical) polarizations are:

$$\Gamma_\perp = \frac{E_{r\perp}}{E_{i\perp}}, \qquad T_\perp = \frac{E_{t\perp}}{E_{i\perp}} \tag{3.120}$$

$$\Gamma_\parallel = \frac{E_{r\parallel}}{E_{i\parallel}}, T_\parallel = \frac{E_{t\parallel}}{E_{i\parallel}} \tag{3.121}$$

The recursive formulas for A_j, B_j, C_j, D_j are:

$$A_j = e^{\psi_j/2}\left[A_{j+1}\left(1 + Y_{j+1}\right) + B_{j+1}\left(1 - Y_{j+1}\right)\right] \tag{3.122}$$

$$B_j = e^{-\psi_j/2}\left[A_{j+1}\left(1 - Y_{j+1}\right) + B_{j+1}\left(1 + Y_{j+1}\right)\right] \tag{3.123}$$

$$C_j = e^{\psi_j/2}\left[C_{j+1}\left(1 + Z_{j+1}\right) + D_{j+1}\left(1 - Z_{j+1}\right)\right] \tag{3.124}$$

$$D_j = e^{-\psi_j/2}\left[C_{j+1}\left(1 - Z_{j+1}\right) + D_{j+1}\left(1 + Z_{j+1}\right)\right] \tag{3.125}$$

With

$$A_{N+1} = C_{N+1} = 1, \quad B_{N+1} = D_{N+1} = 0 \tag{3.126}$$

$$Y_{j+1} = \frac{Z_{j+1}\cos\theta_{j+1}}{\cos\theta_j} \tag{3.127}$$

$$Z_{j+1} = \frac{\varepsilon_{j+1}\left(1 - j\tan\delta_{j+1}\right)\mu_j}{\varepsilon_j\left(1 - j\tan\delta_j\right)\mu_{j+1}} \tag{3.128}$$

$$\psi_j = d_j\gamma_j\cos\theta_j \tag{3.129}$$

$$\gamma_j = \pm j\omega\mu_j\left(\sigma_j + j\omega\varepsilon_j\right) \tag{3.130}$$

$$\theta_j = \text{complex angle in layer } j \tag{3.131}$$

3.2.5 Polarization Characteristics on Reflection

- Linearly polarized fields maintain linear polarization when reflected from flat surfaces. Curved or rough surfaces induce a cross-polarized component.
- Circularly polarized waves maintain circular polarization but may reverse rotation upon reflection from PEC surfaces or transform to elliptical polarization on dielectric surfaces.
- Elliptically polarized waves maintain or alter their axial ratio and sense of rotation depending on the reflecting surface type.

For an elliptically polarized wave incident on a flat surface, the incident fields are:

$$E_{i\parallel} = \widehat{a_x}E_{0\parallel}e^{-j\beta_i\cdot r} \tag{3.132}$$

$$E_{i\perp} = \widehat{a_y}E_{0\perp}e^{-j(\beta_i\cdot r - \phi_{i\perp})} \tag{3.133}$$

The Poincaré sphere angles of the incident wave are:

$$\gamma_i = \tan^{-1}\frac{|E_{0\perp}|}{|E_{0\parallel}|} \tag{3.134}$$

$$\delta_i = \phi_{i\perp} - \phi_{i\parallel}, \qquad \epsilon_i = \cot^{-1}(AR_i), \quad \tau_i = \text{tilt angle} \tag{3.135}$$

From these, the Poincaré sphere angles of the reflected and transmitted fields are:

$$\gamma_r = \tan^{-1}\frac{|E_{r\perp}|}{|E_{r\parallel}|}, \tag{3.136}$$

$$\delta_r = \phi_{r\perp} - \phi_{r\parallel} \tag{3.137}$$

$$\epsilon_r = \cot^{-1}(AR_r), \quad \tau_r = \text{tilt angle} \tag{3.138}$$

$$\gamma_t = \tan^{-1}\frac{|E_{t\perp}|}{|E_{t\parallel}|} \tag{3.139}$$

$$\delta_t = \phi_{t\perp} - \phi_{t\parallel} \tag{3.140}$$

$$\epsilon_t = \cot^{-1}(AR_t), \quad \tau_t = \text{tilt angle} \tag{3.141}$$

These equations allow the determination of polarization characteristics of reflected and transmitted fields given the incident wave polarization.

3.2.6 Introduction to FMCW Radar

Phase shift (PS) plays a vital role in FMCW radar systems for determining the distance to a target. It arises from the time delay (τ) experienced by the radar signal as it travels to the target and back. This delay causes a phase difference between the sent and received signals, which carries information about both the range and the characteristics of the reflecting material. Compared to amplitude, which is more prone to environmental effects, phase data offers greater accuracy and consistency. Typically, FMCW radar uses PS to estimate range, making it suitable for high-precision applications like autonomous driving, object tracking, and industrial monitoring. However, this study utilizes the PS for a different goal—detecting diesel fuel contamination caused by water.

The FMCW radar technique is based on a continuous signal that changes frequency linearly over time. When this signal reflects off a target, it returns with a delay. The radar mixes the delayed signal with the current transmission, generating a beat frequency that reflects both the delay and phase change. This information is then processed to identify patterns. For a wave moving in the z-direction through a lossless medium ($\sigma = 0$), the electric field (E) is described mathematically using a complex exponential function, incorporating parameters such as the wave number (β), angular frequency (ω), time (t), and phase constant (φ).

Equation (1) includes a phase factor expressed as a complex exponential term. This factor has three parts: spatial dependence (βz), time dependence (ωt), and a constant initial phase ($\emptyset$). Spatial coherence measures how waveforms relate across different points in space, while temporal coherence assesses their phase alignment over time. High coherence is essential for clear signal interpretation in radar systems. When a wave reflects off a target, it introduces a time delay, resulting in a phase shift and causing the received signal to be incoherent with the transmitted one.

The setup comprises a voltage-controlled oscillator, signal splitter, transmit and receive antennas, a mixer, an amplifier, filtering stages, an analog-to-digital converter

(ADC), and processing units. The phase Ø(t) varies with frequency, and for simplicity, signal amplitude (A) and Doppler effects are held constant. Equations (3) and (4) describe the transmitted and received signals. The received signal is delayed by τ, resulting in a phase difference due to the distance traveled. Other relevant parameters include signal duration (t), chirp bandwidth (B), modulation rate (γ), chirp time (T), and initial phase Øi(t).

$$S_i = Ae^{-i\emptyset(t)} \tag{3.142}$$

$$e^{[i2\pi f_c(t)+i\pi\gamma(t)^2+\emptyset_i(t)]} \tag{3.143}$$

$$e^{[i2\pi f_c(t-\tau)+i\pi\gamma(t-\tau)^2+\emptyset_i(t-\tau)]} \tag{3.144}$$

When the radar receives the reflected signal, it passes through an amplifier and is then mixed with the currently transmitted waveform. The signals from Equations (3) and (4) are multiplied in the mixer, producing a beat frequency f_b as shown in Equation (5). This frequency results from the delay τ and is influenced by the distance R(t) and the speed of light ccc. Equation (6) details the output signal's phase: the first term shows a linear time-dependent phase due to delay, the second is a constant phase offset from the carrier, the third is minimal, and the last represents random noise. The critical phase shift originates mainly from the second term. When combining Equations (5) and (6), the interference signal phase $\Delta\phi_{IF}$, described in Equation (7), is derived. This phase shift reflects the total round-trip distance and is scaled by the modulation rate. The ADC captures this data, and the signal processing unit uses it to extract useful measurements.

$$f_b = \gamma\tau = \frac{B}{T}\frac{2R}{c} \tag{3.145}$$

$$e^{[i2\pi f_b t+i2\pi f_c\tau+i\pi\gamma(\tau)^2+\Delta\emptyset]} \tag{3.146}$$

$$\Delta\emptyset_{interf} = \emptyset_{Tx}(t)-\emptyset_{Rx}(t) = 4\pi\gamma\frac{R(t)}{c} \tag{3.147}$$

According to Equation (7), the combination of the transmitted and received signals produces a phase shift due to their frequency mismatch. This phase difference is conventionally used to extract the beat frequency, which is associated with measuring distance and motion. In this work, however, the focus shifts from range or velocity detection to evaluating the contamination level. The proposed algorithm interprets the phase shift to determine a level value, offering a novel application of FMCW radar signal analysis.

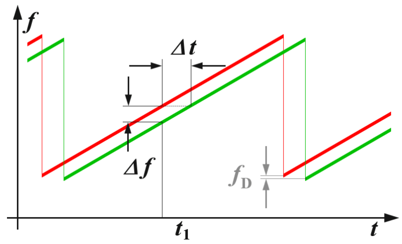

Figure 3.1. A typical FMCW radar waveform (Frequency against Time)

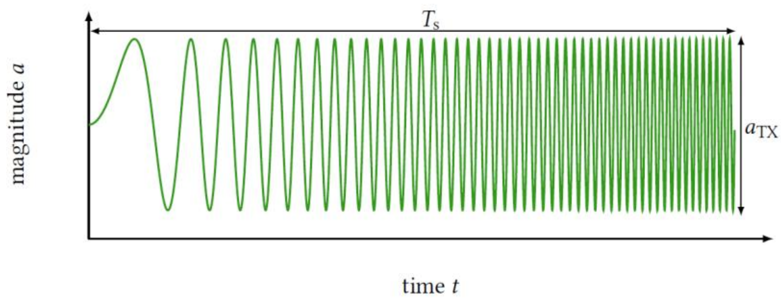

Figure 3.2. A typical FMCW radar waveform (Magnitude against Time)

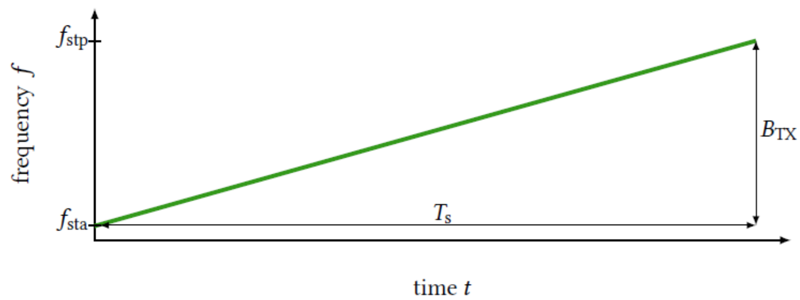

Figure 3.3. FMCW Radar Beat Frequency

FMCW Radar in Liquid Level Measurements

The application of FMCW radar in liquid level measurement has been extensively studied due to its precision, reliability, and adaptability to harsh environments. Several key studies highlight the performance and design considerations for FMCW radars in measuring liquid levels:

1. **High-Resolution Liquid Level Measurement**
   - This study explores the implementation of FMCW radar for millimeter-level precision in industrial tanks.
2. **Dual-Liquid Interface Measurement**

- Researchers developed an FMCW radar to detect interfaces in dual-liquid systems, such as water beneath oil.

Defining Mathematical Models

To analyze the level measurement of two liquids (diesel and water) layered above each other using an FMCW radar, we need to consider how the electromagnetic (EM) waves propagate through different media, as their speed changes based on the material's dielectric permittivity. The radar will detect reflections from each interface where there is a change in material properties.

While standard FMCW radar systems are often designed for single-material level measurements, detecting multiple liquid layers, especially in a tank, requires complicated signal processing methods. This is because the velocity of the electromagnetic wave changes as it passes through each liquid, influencing the relationship between the measured beat frequency and the actual physical distance.

The speed of an electromagnetic wave (V) in a non-magnetic dielectric medium is slower than the speed of light in a vacuum (c), and is related to the medium's relative permittivity, this means that for the same physical distance, the time delay will be longer in a medium with a higher permittivity.

3.3 Machine Learning

3.3.1 Introduction

In essence, according to Kim (2017) and Micheli-Tzanakou (2000), Machine Learning (ML) is a modeling approach that relies on data. While this description may appear overly simplistic, a deeper explanation clarifies its essence. Machine Learning refers to a technique that derives a model from data. The term data encompasses various forms of information, including documents, audio, and images. The model, in turn, represents the final outcome of the Machine Learning process.

Interestingly, the definition emphasizes data and model but does not explicitly mention learning. The concept of "learning" arises because the system autonomously analyzes data to generate a model—analogous to how a human learns from experience. Consequently, the data used in this process is termed training data. **Figure 3.4** illustrates the workflow of the Machine Learning process.

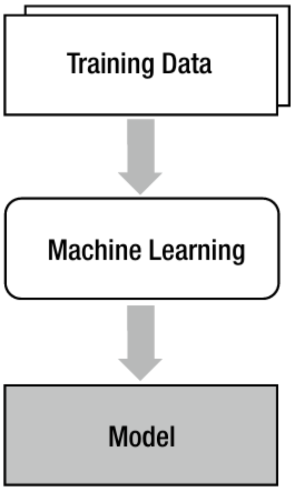

Figure 3.4. Workflow of Machine Learning Process

The model itself represents the end goal of the process. For example, in developing an automated spam detection system, the spam filter constitutes the model. In this sense, the model functions as the practical application of Machine Learning outcomes. Some scholars refer to this as a hypothesis, a term familiar to those with a background in statistics. Machine Learning is one of several modeling methodologies. In physics, for instance, models are developed using Newton's laws to describe motion through equations of motion. In Artificial Intelligence, expert systems are another example, built upon the knowledge and reasoning of human experts to replicate their decision-making capabilities. However, for domains such as image recognition, speech recognition, and natural language processing—where explicit laws and reasoning are insufficient—Machine Learning provides an effective alternative.

3.3.1.1 Classification Technique

Classification is a "supervised machine learning' approach designed to predict categorical labels based on input data. Its objective is to assign each observation to one of several predefined classes, for example, distinguishing between spam and non-spam emails or identifying patients as healthy or diseased. A simple illustration involves training a classification model on an image dataset labeled as "dogs" and "cats." Once trained, the model can predict the class of new, unseen images based on distinguishing features such as color, texture, and shape.

In a two-dimensional representation of classification, the horizontal axis may combine color and texture features, while the vertical axis represents shape and size. Each colored dot corresponds to an image sample, with color indicating the predicted label. The shaded areas represent "decision boundaries", which define how the model separates one class from another.

3.3.1.1.1 Types of Classification

Classification tasks vary depending on the number and nature of categories involved:

3.3.1.1.1.1 Binary Classification

The simplest form, where data are classified into two mutually exclusive categories (e.g., spam vs. non-spam).

3.3.1.1.1.2 Multiclass Classification

Involves more than two classes, such as an image classifier that identifies cats, dogs, or birds.

3.3.1.1.1.3 Multi-Label Classification

A data instance can belong to multiple categories simultaneously (e.g., a movie tagged as both "action" and "comedy"), as illustrated in **Figure 3.5**.

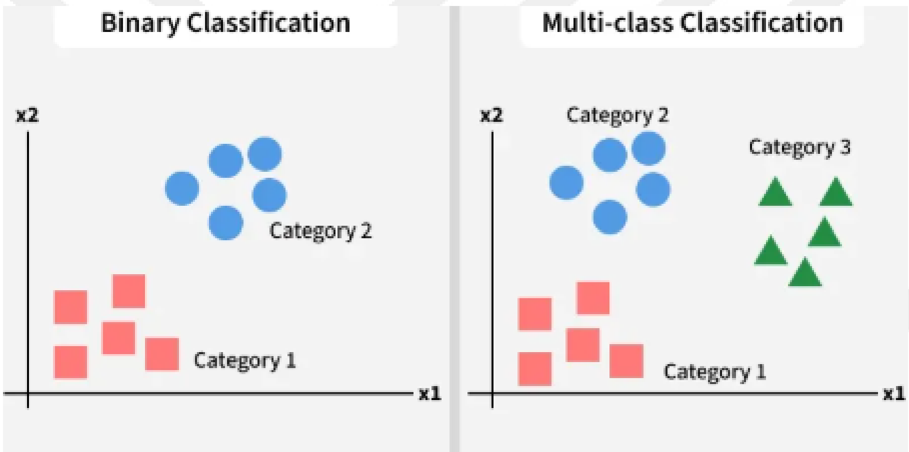

Figure 3.5. Binary and Multi Class Classification

3.3.1.1.2 How Classification Works

Classification relies on training a model using labeled data—datasets in which each input is paired with the correct output label. The process involves:

1. Data Collection : Gathering labeled examples.
2. Feature Extraction : Identifying characteristics (e.g., color, shape) that differentiate classes.
3. Model Training : Using algorithms to learn the mapping between features and labels.
4. Evaluation : Testing performance on unseen data.
5. Prediction : Classifying new data based on learned patterns.
6. Model Evaluation : Evaluating a classification model, check how well the model performs and how good it is at handling new data.

If model accuracy is unsatisfactory, algorithms or hyperparameters can be fine-tuned and retrained iteratively until optimal performance is achieved.

3.3.1.1.3 Classification Algorithms

Common classification algorithms include:

1. Linear Classifiers:
   a. Logistic Regression
   b. Linear SVM
   c. Single-Layer Perceptron
   d. SGD Classifier.
2. Non-Linear Classifiers:
   a. K-Nearest Neighbors
   b. Kernel SVM
   c. Naïve Bayes
   d. Decision Trees.
   e. Ensemble and Advanced Models
   f. Random Forests
   g. AdaBoost
   h. Bagging
   i. Voting Classifiers
   j. Extra Trees
   k. Multi-Layer Neural Networks.

3.3.1.1.4 Real-World Applications

Classification techniques are applied in:

a. Email Spam Filtering: Distinguishing spam from legitimate messages.
b. Credit Risk Assessment: Predicting loan default risk.
c. Medical Diagnosis: Identifying diseases from clinical data.
d. Image Classification: Enabling facial recognition and autonomous driving.
e. Sentiment Analysis: Assessing opinions in text data.
f. Fraud Detection: Identifying anomalous transaction patterns.
g. Recommendation Systems: Suggesting content or products to users.
h. engineers or developers).

3.3.1.2 Regression Technique

Regression in machine learning is a supervised learning technique used to predict a continuous numerical value based on one or more input variables (features). The objective of regression is to model the relationship between the dependent variable (target), the quantity to be predicted, and one or more independent variables (features) that influence it. For example, when estimating house prices, the dependent variable is the price, while the independent variables may include location, number of rooms, and lot size. Regression problems are characterized by continuous outputs such as salary, temperature, or weight. Among the various regression models available, linear regression is the simplest and most widely used.

3.3.1.2.1 Types of Regression

3.3.1.2.1.1 Simple Linear Regression

Assumes a linear relationship between the dependent and independent variable. For instance, predicting house prices based solely on size.

3.3.1.2.1.2 Multiple Linear Regression

Extends the simple model to multiple predictors, such as predicting house prices using size, location, and number of rooms.

3.3.1.2.1.3 Polynomial Regression

Used when relationships are non-linear. Polynomial terms are added to the model to capture curvature in the data, such as modeling population growth over time.

3.3.1.2.1.4 Ridge and Lasso Regression

Regularized forms of linear regression that add penalties to prevent overfitting, particularly useful when dealing with many correlated features.

3.3.1.2.1.5 Support Vector Regression (SVR)

A regression adaptation of the Support Vector Machine (SVM) algorithm that fits an optimal hyperplane minimizing prediction errors.

3.3.1.2.1.6 Decision Tree Regression

Utilizes a tree-like structure where branches represent decisions and leaves represent outcomes, such as predicting customer behavior from demographic data.

3.3.1.2.1.7 Random Forest Regression

An ensemble learning method that combines multiple decision trees trained on different data subsets. The final output is the average of all trees' predictions, improving robustness and accuracy.

3.3.1.2.2 Evaluation Metrics

Model performance in regression tasks is assessed using several statistical metrics:

3.3.1.2.2.1 Mean Absolute Error (MAE):

Average of absolute prediction errors.

3.3.1.2.2.2 Mean Squared Error (MSE):

Average of squared prediction errors.

3.3.1.2.2.3 Root Mean Squared Error (RMSE):

Square root of MSE, providing error in original units.

3.3.1.2.2.4 Huber Loss:

A hybrid metric combining MAE and MSE to balance robustness and sensitivity to outliers.

3.3.1.2.2.5 R^2 Score:

Model evaluation is a critical step in any machine learning workflow. Various evaluation metrics exist, and the appropriate choice depends on the type of predictive problem—regression, classification, or otherwise. In the context of regression analysis, one of the most widely used metrics is the coefficient of determination, commonly referred to as R-squared (R^2).

R-squared is a statistical indicator that measures how well a regression model explains the variability of the dependent variable. Its value ranges from 0 to 1. An R^2 value of 1 indicates a perfect fit, where predicted values match the observed values exactly. Conversely, an R^2 value of 0 implies that the model fails to capture any variability in the dependent variable and does not learn a meaningful relationship between the predictors and the target.

R-squared quantifies the proportion of variance in the dependent variable Ythat is explained by the independent variables X_i. The metric is computed as follows:

1. Compute the mean of the dependent variable, denoted by $\bar{y}$.
2. Calculate the **total sum of squares**,

$$SS_{\text{tot}} = \sum_{i=1}^{n} (y_i - \bar{y})^2$$

Fit an appropriate regression model (e.g., Linear Regression, SVM Regression) and obtain predictions $\hat{y}_i$.

3. Compute the **regression sum of squares**,

$$SS_{\text{reg}} = \sum_{i=1}^{n} (\hat{y}_i - \bar{y})^2$$

4. Compute the **residual sum of squares**,

$$SS_{\text{res}} = \sum_{i=1}^{n} (y_i - \hat{y}_i)^2 \tag{3.148}$$

5. Derive R-squared using either formulation:

$$R^2 = \frac{SS_{\text{reg}}}{SS_{\text{tot}}}, \text{or } R^2 = 1 - \frac{SS_{\text{res}}}{SS_{\text{tot}}} \tag{3.149}$$

Goodness of Fit

R-squared compares the unexplained variation (SS_{res}) with the total variation in the data (SS_{tot}). Higher R^2 values indicate greater explanatory power, with values closer to 1 reflecting stronger model performance. Although R^2 typically ranges between 0 and 1, it can be negative when the model performs worse than a naive prediction based solely on the mean.

Limitations

A key limitation of R-squared is that it **never decreases** when additional predictors are included, regardless of whether those predictors are meaningful. Since SS_{tot}remains constant and adding variables often decreases SS_{res}, R^2 may increase even for non-informative predictors. This may lead to overly complex models with inflated performance estimates.

Adjusted R-Squared

To address this limitation, **Adjusted R-squared** incorporates the number of predictors into the calculation, penalizing unnecessary model complexity. It is defined as:

$$\text{Adjusted } R^2 = 1 - (1 - R^2)\frac{n-1}{n-k-1},$$

where

- $R^2$is the coefficient of determination,
- $n$is the number of observations, and
- $k$is the number of independent variables.

Adjusted R^2 increases only when new variables improve model performance and decreases when they do not, making it more suitable for comparing models with different numbers of predictors.

3.3.1.2.3 Applications of Regression

- Price Prediction: Estimating property or product prices.

- Trend Forecasting: Predicting future sales or demand.
- Risk Analysis: Identifying medical or financial risk factors.
- Decision Support: Guiding investment or operational decisions.

3.3.1.2.4 Advantages

- Easy to interpret and implement.
- Effective for linear relationships.
- Computationally efficient.

3.3.1.2.5 Disadvantages

- Assumes linearity between variables.
- Sensitive to multicollinearity among features.
- May not handle complex, non-linear relationships well.

3.3.2 Challenges with Machine Learning

Machine Learning (ML) is fundamentally a technique designed to derive or "learn" a model from data. It is particularly suitable for problems requiring intelligent interpretation, such as image or speech recognition, where physical laws or explicit mathematical formulations are insufficient. While the approach that ML adopts enables such capabilities, it also introduces inherent challenges. This section discusses the essential issues associated with Machine Learning.

Once a model has been developed using training data, it is applied to real-world or field data, as illustrated in Figure 3.6. The vertical flow represents the learning phase, whereas the horizontal flow denotes the inference phase, where the trained model is utilized. It is important to note that the data used during training differs from the data encountered in actual applications. To highlight this distinction, Figure 3.7 introduces an additional conceptual block.

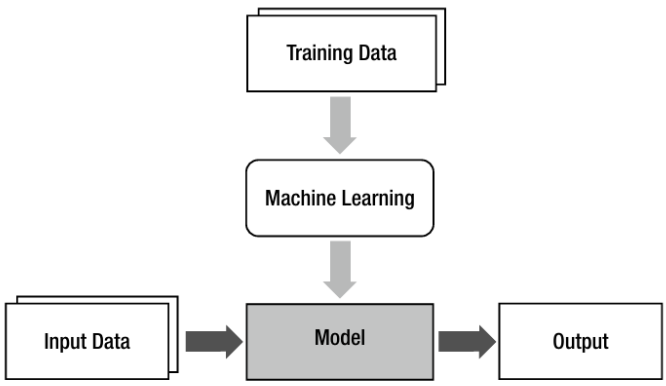

Figure 3.6. Model Based on Field Data

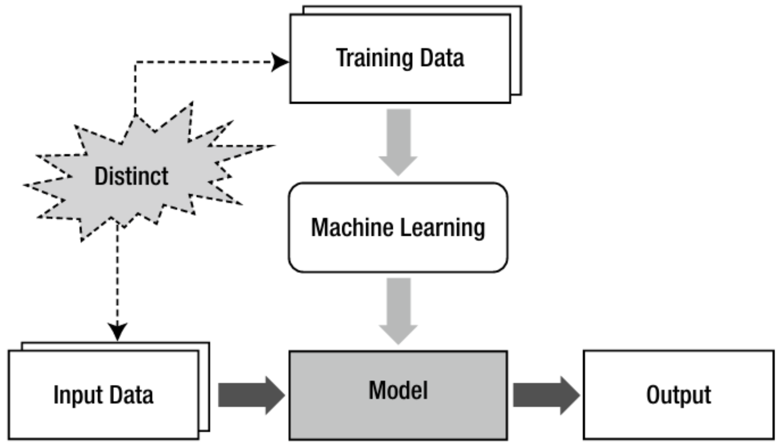

Figure 3.7. Training and Input Data sometimes Distinct

The difference between training and field data forms the central structural challenge of ML. In fact, most of the difficulties encountered in Machine Learning originate from this very distinction. For instance, a model trained exclusively on handwritten samples from a single individual may perform poorly when recognizing handwriting from others. Therefore, it is crucial that ML systems are trained on unbiased, representative datasets that accurately reflect the characteristics of real-world data. The process that ensures consistent model performance regardless of data variations is known as *generalization*, and the effectiveness of Machine Learning largely depends on how well this is achieved.

3.3.2.1 Overfitting

One of the main factors that deteriorate the generalization capability of a Machine Learning model is overfitting. Although the term may seem new, the concept itself is straightforward and can be best understood through an illustrative example.

Consider a classification problem, as shown in **Figure 3.8**, where the goal is to separate data points into two distinct groups based on their coordinates. These points represent the training data. The task is to determine an appropriate boundary curve that divides the groups effectively. As seen in **Figure 3.9**, despite the presence of several outliers, the chosen curve provides a reasonable separation between the two clusters, although a few points remain misclassified.

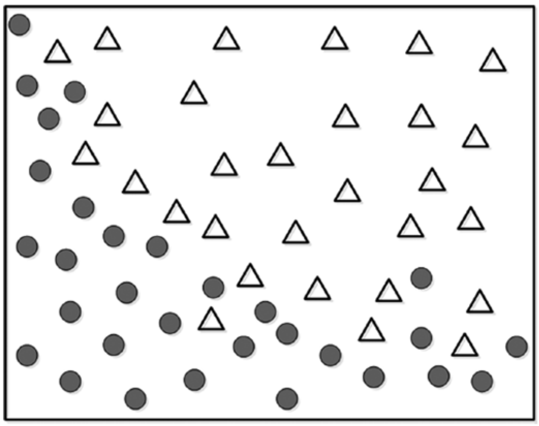

Figure 3.8. Raw Data Representation before Curve Fitting

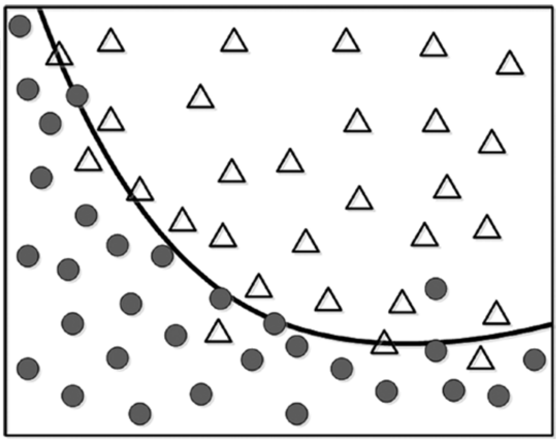

Figure 3.9. Simple Curve for Fitting and Differentiation

Now imagine constructing a more complex curve, as shown in **Figure 3.10**, which perfectly separates all the training data points. While this model achieves 100% accuracy on the training set, it fails to represent the general pattern of the data. When tested with new input data (symbolized by ■ in **Figure 3.11**), the model misclassifies the sample, despite the broader trend suggesting otherwise.

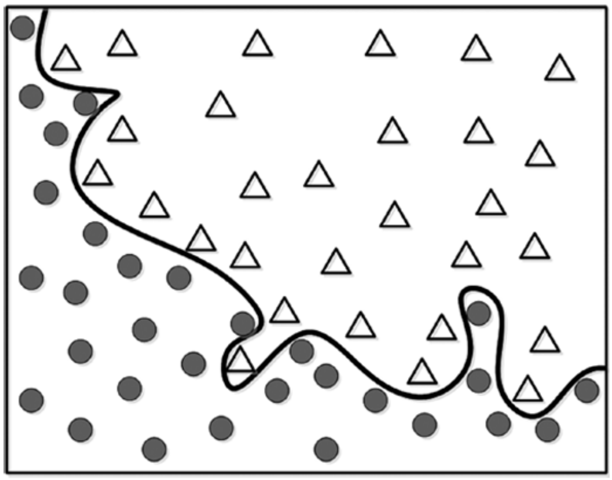

Figure 3.10. Better Grouping at Higher Cost

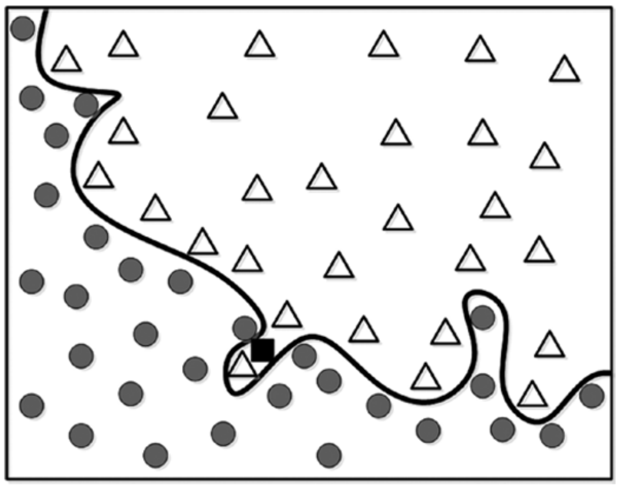

Figure 3.11. New Input to the Data Model

This problem arises because the training data often contains noise or irregularities, and Machine Learning algorithms typically treat all data as equally valid. As a result, the model overfits—learning not only the true structure but also the random fluctuations of the dataset. Consequently, while the model performs exceptionally well on the training data, it generalizes poorly to unseen data. Overfitting, therefore, represents a fundamental trade-off: minimizing training error too aggressively can lead to reduced adaptability in real-world applications. The challenge lies in striking a balance—achieving high accuracy without compromising generalization. The next section introduces techniques developed to mitigate overfitting and enhance model robustness.

3.3.2.2 Confronting Overfitting

Overfitting has a substantial impact on the overall performance of Machine Learning models. The ability to effectively handle overfitting often distinguishes experienced practitioners from novices. This section introduces two fundamental techniques commonly employed to address this issue: regularization and validation.

3.3.2.2.1 Regularization

Regularization is a mathematical approach designed to construct a model that is as simple as possible without significantly compromising accuracy. A simpler model tends to reduce the influence of overfitting, even if it slightly decreases performance. Referring to the grouping problem discussed earlier, the complex curve represents an overfitted model, whereas the simpler curve—though it misclassifies a few points—better reflects the general trend of the data. Further discussion of regularization will be provided in Chapter Three, in the section titled "Cost Function and Learning Rule."

In some cases, overfitting can be easily identified through visualization, particularly when the data is low-dimensional. However, in high-dimensional datasets, visual assessment is impractical. Therefore, an additional technique, known as validation, is necessary to determine whether a trained model is overfitted.

3.3.2.2.2 Validation:

Validation involves setting aside a portion of the training data that is not used during the learning process. This reserved subset, known as the validation set, is utilized to evaluate the model's generalization capability. If the model performs well on the training data but poorly on the validation data, it indicates overfitting. In such cases, model adjustments are required to improve generalization. **Figure 3.12** illustrates the partitioning of training data for the validation process.

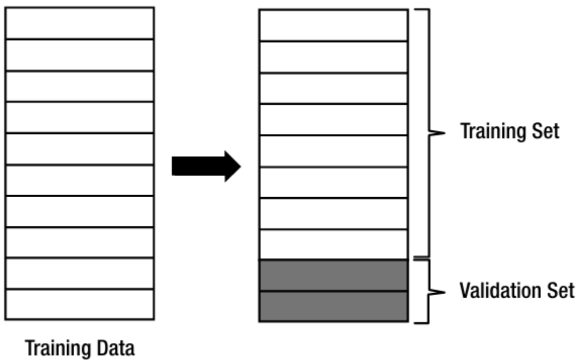

Figure 3.12. Dividing Data for Training and Validation Sets

When the validation process is incorporated, the training procedure in Machine Learning generally follows these steps:

3.3.2.2.2.1 Data Partitioning:

Divide the dataset into two subsets — one for training and the other for validation. As a general guideline, the training-to-validation ratio is typically 8:2.

3.3.2.2.2.2 Model Training (Step 2):

Train the model using the training subset.

3.3.2.2.2.3 Performance Evaluation:

Assess the model's performance on the validation subset.

a. If the model demonstrates satisfactory performance, the training process is complete.

b. If the performance is inadequate, modify the model's parameters or structure, and repeat the process starting from Step 2.

A slight variation of this method is known as cross-validation. In cross-validation, the dataset is still divided into training and validation subsets; however, these subsets are systematically changed during each iteration. Instead of using a fixed validation set, the data is repeatedly partitioned in different ways throughout the process. The primary purpose of cross-validation is to prevent the model from overfitting to a specific validation set. By continuously varying the validation data, the method maintains randomness and provides a more reliable estimate of the model's generalization performance. **Figure 3.13** illustrates the concept of cross-validation, where the dark-shaded sections represent the validation data randomly selected during each training iteration.

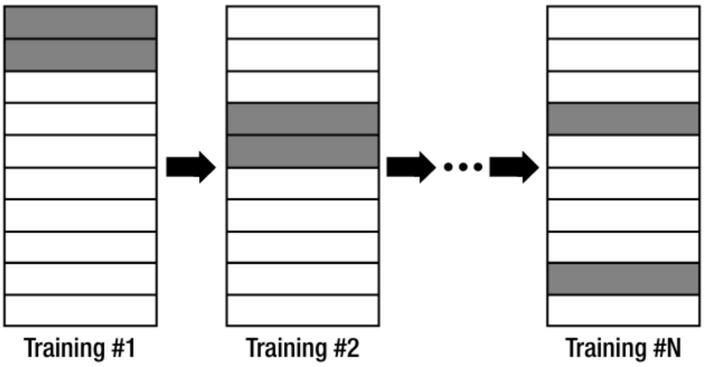

Figure 3.13. Cross Validation Process

3.4 Simulations and Measurements

3.4.1 Simulation using MATLAB

3.4.1.1 Description of the Code and Its Purpose

The MATLAB script models the electromagnetic behavior of a Frequency-Modulated Continuous Wave (FMCW) radar signal as it interacts with a layered medium composed of air, diesel, contaminated water, and steel. The primary goal is to analyze how different water contamination levels within the diesel layer affect the reflected radar signal, particularly focusing on the S11 reflection coefficient and its phase response across frequency. The program simulates both parallel and perpendicular polarizations of the incident electromagnetic wave and allows user interaction for various physical parameters like incidence angle, material thicknesses, and frequency range. Applications include radar-based level sensing in storage tanks (e.g., fuel tanks with water contamination) and dielectric layer detection in harsh industrial environments. In **Figure 3.14**, a flowchart shows how this program was structured.

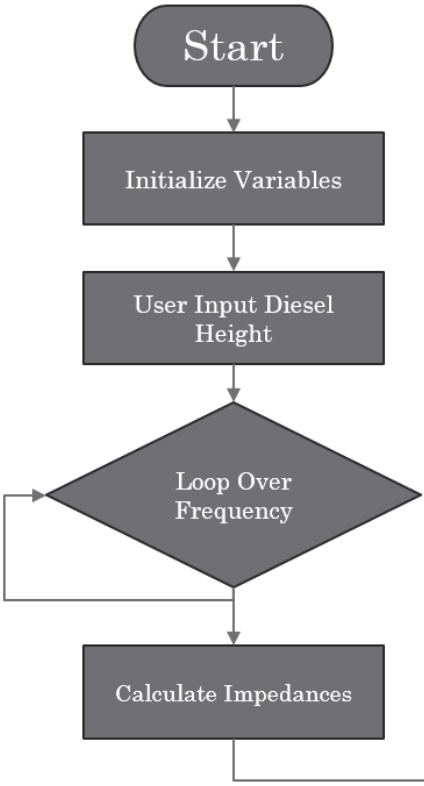

Figure 3.14. Flowchart indicating the flow of MATLAB code program

3.4.1.2 Key Equations:

Propagation Constant:

$$\gamma = \sqrt{\left(i\omega\mu_0\mu_r(\sigma + i\omega\varepsilon_r\varepsilon_0)\right)} \tag{3.150}$$

Intrinsic Impedance:

$$\eta = \sqrt{\left((i\omega\mu_0\mu_r)/(\sigma + i\omega\varepsilon_r\varepsilon_0)\right)} \tag{3.151}$$

Snell's Law:

$$\theta_t = \arcsin\left(\sqrt{(\varepsilon_i/\varepsilon_t)\backslash cdotsin}(\theta_i)\right) \tag{3.152}$$

3.4.1.3 Step-by-Step Approach

1. User Inputs: Frequency range, diesel height, water contamination step, polarization type, and angle of incidence.
2. Initialization: Define physical constants and construct frequency sweep vector.
3. Material Properties Setup: Assign dielectric properties to air, diesel, water, and steel.
4. Loop Over Water Depths: Calculate propagation constants, impedance, angles, and electric fields. Derive total reflected field and S11.
5. Post-Processing: Convert the phase of the reflected signal to degrees and plot the phase vs frequency for varying contamination levels.

3.4.1.4 Applied Example

Inputs:
- Minimum Frequency: 0.8 GHz
- Maximum Frequency: 0.9 GHz
- Diesel Height: 100 cm
- Water Contamination Step: 2 mm
- Polarization: Parallel

Output:
The script simulates 10 contamination levels from 2 mm to 20 mm and displays a plot of S11 phase shift vs frequency for each level.
The phase plot helps identify changes in reflection behavior due to water content in the diesel layer.

1. Frequency and Angular Frequency

$$f = \text{linspace}(0.8\,\text{GHz}, 10\,\text{MHz}, N) \tag{3.153}$$

Angular frequency:

$$\omega = 2\pi f \tag{3.154}$$

2. Relative Permittivity for Each Medium

Air:

$$-\varepsilon_r^{(\mathrm{air})} = 1 \tag{3.155}$$

Diesel:

$$-\varepsilon_r^{(\mathrm{diesel})} = 2.1 - 0.001i \tag{3.156}$$

Water:

$$-\varepsilon_r^{(\mathrm{water})} = 78 - 10i \tag{3.157}$$

Steel (conductor, modeled with complex permittivity):

$$\varepsilon_r^{(\mathrm{steel})} = -1000 - 1000i \tag{3.158}$$

3. Absolute Permittivity

$$\varepsilon = \varepsilon_r \cdot \varepsilon_0 \tag{3.159}$$

Where:

$$\varepsilon_0 = 8.854 \times 10^{-12}\ \mathrm{F/m} \tag{3.160}$$

4. Wave Number

$$-k = \omega\sqrt{\mu_0 \varepsilon} \tag{3.161}$$

Where:

$$-\mu_0 = 4\pi \times 10^{-7}\ \mathrm{H/m} \tag{3.162}$$

5. Reflection Coefficients Between Layers

At the air–diesel interface:

$$\mathrm{r}_{12} = \frac{\mathrm{k}_1 - \mathrm{k}_2}{\mathrm{k}_1 + \mathrm{k}_2} \tag{3.163}$$

At the diesel–water interface:

$$\mathrm{r}_{23} = \frac{\mathrm{k}_2 - \mathrm{k}_3}{\mathrm{k}_2 + \mathrm{k}_3} \tag{3.164}$$

At the water–steel interface:

$$\mathrm{r}_{34} = \frac{\mathrm{k}_3 - \mathrm{k}_4}{\mathrm{k}_3 + \mathrm{k}_4} \tag{3.165}$$

6. Phase Shift in Each Layer

For layer thickness and wave number:

$$\phi = 2\,\mathrm{k}\,\mathrm{d} \tag{3.166}$$

7. Recursive Reflection Coefficient Calculation

Total reflection at water–steel interface:

$$\mathrm{r}_{34}^{\mathrm{total}} = \mathrm{r}_{34} \tag{3.167}$$

Total reflection at diesel–water interface:

$$\mathrm{r}_{23}^{\mathrm{total}} = \frac{\mathrm{r}_{23} + \mathrm{r}_{34}^{\mathrm{total}} e^{-2i\mathrm{k}_3\mathrm{d}_3}}{1 + \mathrm{r}_{23}\mathrm{r}_{34}^{\mathrm{total}} e^{-2i\mathrm{k}_3\mathrm{d}_3}} \tag{3.168}$$

Total reflection at air–diesel interface (final S11):

$$\Gamma = r_{12}^{total} = \frac{r_{12} + r_{23}^{total} e^{-2ik_2 d_2}}{1 + r_{12} r_{23}^{total} e^{-2ik_2 d_2}} \tag{3.169}$$

8. Return Loss / Reflection Magnitude in dB

$$|\Gamma|_{dB} = 20 \log_{10} |\Gamma| \tag{3.170}$$

3.4.2 Simulation using CST Software

To visualize the theoretical model, a 3D electromagnetic simulation was carried out using CST Studio. The model consisted of a tank structure with transmission and reception antennas placed above it. Layers of diesel and water were digitally recreated, and material properties were defined using estimated or library-based permittivity values.

The simulation mesh focused on a cross-section of the tank, incorporating discrete probes to capture electric field magnitudes at various depths. A frequency-swept sinusoidal signal mimicked the FMCW waveform. Results confirmed that distinct reflection patterns were observable at the interfaces between different fluids, providing theoretical support for practical experiments. In **Figure 3.15**, **Figure 3.16**, and **Figure 3.17**, it is shown the model, probes locations and meshing respectively.

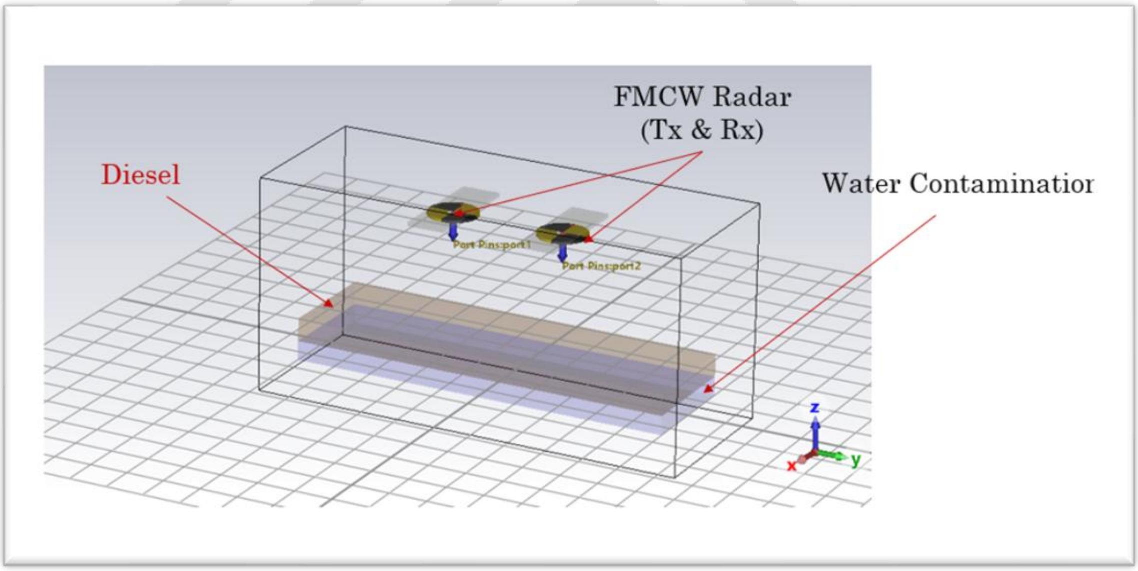

Figure 3.15. Simulation Model in CST 3-D

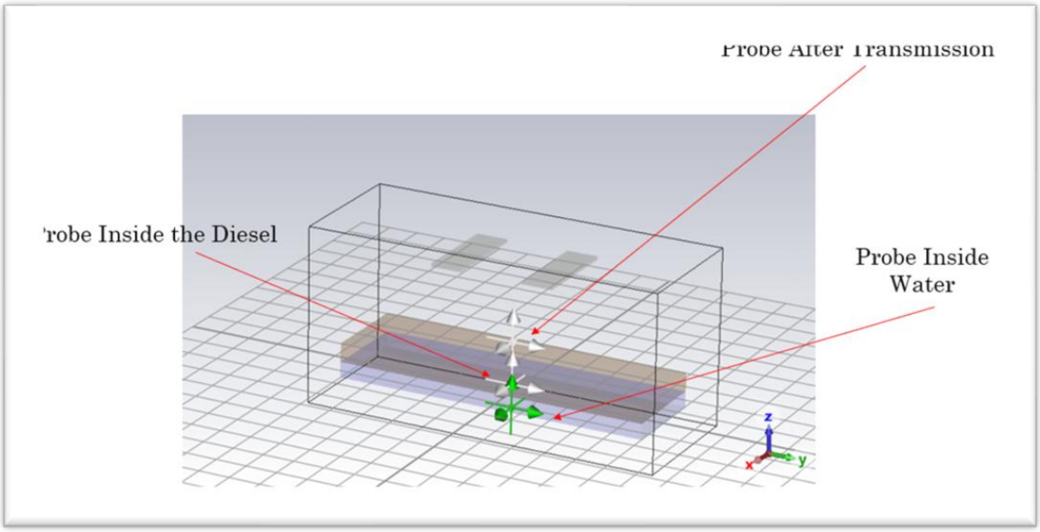

Figure 3.16. Electric Field Probe located below each layer

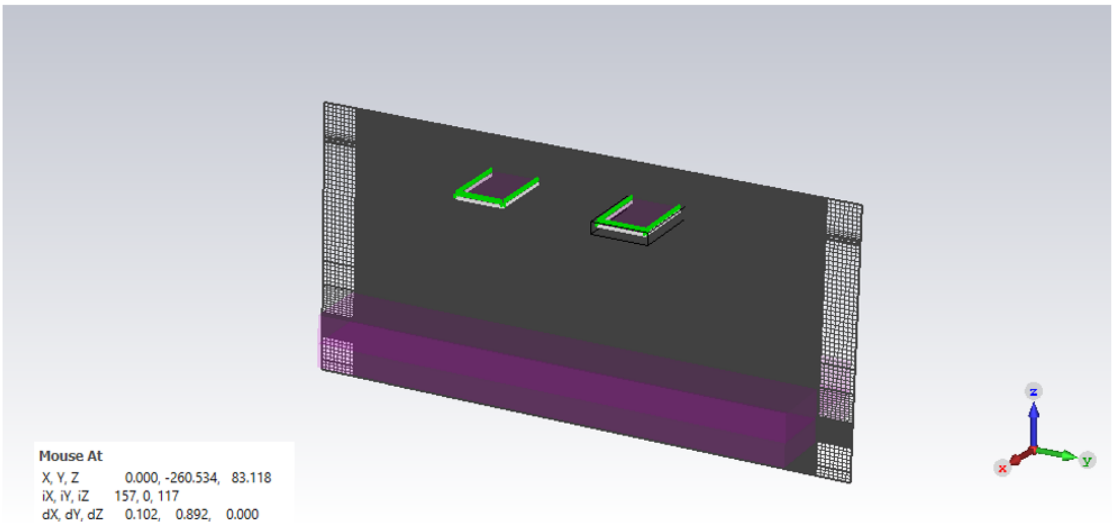

Figure 3.17. Fine Meshing for the section of the tank

3.4.3 Important Considerations for Practical Implementation with Motor Oil (as safe test fluid) and Diesel (as targeted fluid)

In order to perform measurements for our research in an effective and save approach, we do the measurements on stepwise approach as follows:

1. Performing proof of concept using safe fluid first (Motor Oil).

Due to the safety considerations that must be considered during measurements with a flammable fluid like diesel, it was planned to start measurements in an abstract using a fluid with near electrical and material characteristics, and accordingly we selected motor oil as a fluid that can provide similar characteristics and safer test environment in the primary measurement stage.

2. Performing the main measurements using diesel fuel.
   After performing the measurements using safe fluid like motor oil, we must implement a wider scope of measurements after taking into consideration the safety measures and after upgrading the test environment and equipment to cope with the wider scope and the amount of data to be collected

3.4.3.1 Considerations for Measurements for FMCW Radar

Several factors influence the practical feasibility and accuracy of such a system:

Attenuation of Electromagnetic Waves: Electromagnetic signals gradually attenuate as they propagate through different media, particularly in liquids with high dielectric permittivity such as water. Consequently, reflections originating from deeper interfaces—such as the diesel–water boundary—exhibit lower amplitude compared to those from the upper diesel–air interface. This attenuation must be accounted for when interpreting reflection magnitudes and phase responses.

Reflection Strength: The magnitude of the reflected signal primarily depends on the dielectric permittivity contrast between adjacent layers. Diesel, with relative permittivity $\varepsilon_r < 3$, and water, with $\varepsilon_r \approx 80$, produce a pronounced dielectric discontinuity that results in a strong, easily detectable reflection at their interface. Conversely, when the contrast is small—as between similar hydrocarbon layers or between diesel and the metallic tank wall—reflection strength diminishes, complicating interface detection and boundary distinction.

Multipath Reflections: Within enclosed containers such as fuel tanks, multiple reflections from walls, joints, and internal structures often generate unwanted interference known as clutter. These multipath effects distort the received signal and obscure genuine liquid boundary echoes. Employing narrow-beam antennas, strategic sensor positioning, and advanced clutter suppression algorithms (e.g., time-gating or matched filtering) are essential for mitigating these artifacts.

Temperature Variations: Temperature fluctuations affect both radar hardware and measurement accuracy. Internally, variations in component temperature can alter stability and calibration consistency. Externally, temperature changes influence the dielectric properties of liquids and contribute to atmospheric attenuation, necessitating temperature compensation mechanisms within the signal processing chain.

Antenna Characteristics: The radar antenna's performance—defined by its beamwidth, gain, polarization, and alignment—directly impacts measurement accuracy. Misalignment or excessive beam divergence can introduce additional clutter and reduce spatial resolution. Therefore, precise antenna calibration and orientation are critical for reliable level estimation.

In summary, While the underlying electromagnetic principles of FMCW radar enable the detection of multiple liquid layers with high theoretical precision, practical realization requires meticulous system optimization. Accurate calibration, temperature compensation, and clutter-resistant signal processing are indispensable to overcome challenges introduced by material attenuation, environmental variability, and hardware imperfections.

3.4.3.2 Considerations for Measurements with Motor Oil (as safe fluid for Proof of Concept)

Dielectric and Electromagnetic Properties: Motor oil exhibits a relatively low dielectric constant, typically ranging between 2.1 and 2.6, and possesses negligible electrical conductivity, resulting in inherently weak radar reflections. The introduction of chemical additives, oxidation byproducts, or degradation residues over time can subtly modify these electromagnetic characteristics. Continuous monitoring and calibration are therefore essential to maintain measurement precision.

Temperature Sensitivity: Both the dielectric constant and viscosity of motor oil are highly sensitive to temperature fluctuations. As temperature rises, viscosity decreases and dielectric losses increase, leading to observable changes in the phase and amplitude of the reflected radar signal. Temperature compensation mechanisms should be incorporated into the measurement system to correct these variations.

Surface Stability and Viscosity Effects: Due to its relatively high viscosity, motor oil typically maintains a stable surface under static conditions. However, operational vibrations or flow-induced disturbances can generate minor surface ripples that scatter incident radar waves. Signal averaging or filtering techniques can mitigate such effects, improving signal stability.

Contamination and Degradation: With extended use, motor oil can accumulate contaminants including water, metallic particles, and combustion residues. These impurities alter the oil’s dielectric profile, which can be detected through corresponding variations in radar signal amplitude and phase. Proper calibration of the FMCW radar system enables differentiation between clean and contaminated oil based on contrasts in permittivity.

Tank Wall and Structural Interference: In metallic or irregularly shaped storage tanks, internal reflections from walls and structural components may lead to multipath interference. Optimizing antenna positioning and employing narrow-beam or shielded antenna designs minimizes false echoes and enhances measurement precision.

Signal Attenuation and Frequency Selection: Motor oil introduces moderate attenuation to radar waves, particularly at higher frequencies. Selecting an optimal operating frequency band is critical to balancing spatial resolution with penetration depth.

Lower frequencies improve signal-to-noise ratio but reduce resolution, whereas higher frequencies provide finer measurement precision at the cost of increased attenuation.

Safety and Operational Environment: Although less volatile than diesel, motor oil remains combustible. All experimental and industrial setups must adhere to strict electrical safety protocols to prevent ignition hazards. The non-contact nature of FMCW radar measurement is advantageous in this regard, eliminating physical contact with the fluid and reducing operational risk.

Calibration and Maintenance: Routine calibration using reference oil-levels and controlled contamination samples ensures consistent system performance. Regular cleaning of the radar antenna surface is also recommended to remove oil mist or residue that may affect dielectric coupling and signal strength.

3.4.3.3 Considerations for Measurements with Diesel (as main fluid for Research)

Safety and Hazard Considerations: Diesel fuel is a highly flammable substance; however, it cannot ignite except when evaporated at near 52 °C, but its flammability must be taken into considerations. Therefore, radar-based measurement systems must comply with Intrinsic Safety (IS) and Explosion-Proof (Ex-proof) standards to mitigate ignition risks. All radar and electronic components should be hermetically sealed or installed within ATEX-certified enclosures. The non-contact nature of FMCW radar offers a major safety advantage, as it eliminates the use of immersed sensors or mechanical probes that could generate sparks or electrical discharges, in **Figure 3.18** illustrated the fire extinguisher used during measurements.

Figure 3.18. Fire Extinguisher used during measurements

Electrostatic Discharge (ESD) Risks: Static electricity can accumulate during fuel transfer or radar operation, posing a potential discharge hazard. To prevent such incidents, radar units and associated cables must be properly grounded, shielded, and equipped with static dissipation systems. This precaution is particularly crucial during refueling operations or measurements inside enclosed tanks, where vapor concentration is elevated.

Dielectric and Electromagnetic Properties: Diesel fuel has a low dielectric constant less than 3 and minimal conductivity, resulting in weak radar reflections compared to water or metallic surfaces. Even minor water contamination markedly alters these dielectric properties, producing detectable phase and amplitude variations in the reflected FMCW radar signal.

Temperature and Density Variations: Changes in temperature influence both the density and permittivity of diesel. As temperature increases, viscosity and dielectric constant decrease, causing phase drift in the radar response. Temperature compensation algorithms or calibration tables are recommended for accurate interpretation of the measured data.

Surface Disturbances and Flow Conditions: During fuel transfer or tank agitation, surface ripples and turbulence can occur, introducing amplitude fluctuations and noise in the radar return signal. Signal averaging or adaptive filtering techniques can mitigate these disturbances, enhancing measurement stability.

Contamination Sensitivity and Layer Differentiation: Water contamination typically settles at the tank bottom, creating a strong dielectric contrast at the diesel–water interface. FMCW radar effectively detects this boundary through phase inversion and amplitude enhancement in the reflected signal. Regular calibration using known reference samples ensures reliable distinction among clean diesel, emulsified mixtures, and separated water layers.

Tank Wall and Structural Interference: Metallic or coated tank surfaces can cause multipath reflections, distorting radar measurements. Accurate antenna alignment, appropriate frequency selection, and the use of narrow-beam horn or dielectric-lens help suppress unwanted reflections and improve layer discrimination.

Signal Calibration and Maintenance: Routine calibration under controlled conditions is essential to account for variations in temperature, fuel formulation, and contamination level. The radar antenna should be periodically cleaned and inspected to remove residues or condensation that may degrade signal strength or dielectric coupling efficiency.

Integration with Machine Learning Systems: When combined with machine learning algorithms, FMCW radar data can serve dual analytical functions: classification, to identify contamination presence, and regression, to estimate water layer thickness. This integration enables both real-time alerting systems and advanced level transduction for automated monitoring applications.

3.4.4 Measurements Activities

A physical FMCW radar prototype was constructed in the laboratory using key microwave and signal-processing components, including a voltage-controlled oscillator (VCO), amplifiers, mixers, and analog-to-digital converters (ADC). The VCO generated a linearly modulated triangular frequency waveform through controlled voltage variation, forming the basis of the FMCW signal. The received echoes were subsequently mixed with the transmitted signal to obtain the beat frequency, which was then filtered and digitized for analysis, in **Figure 3.19** below, these components were integrated into a unified experimental setup designed to emulate the operational environment of an FMCW radar system. A generic test tank was incorporated into the setup, initially empty, to be filled sequentially with different test fluids for measurement and validation.

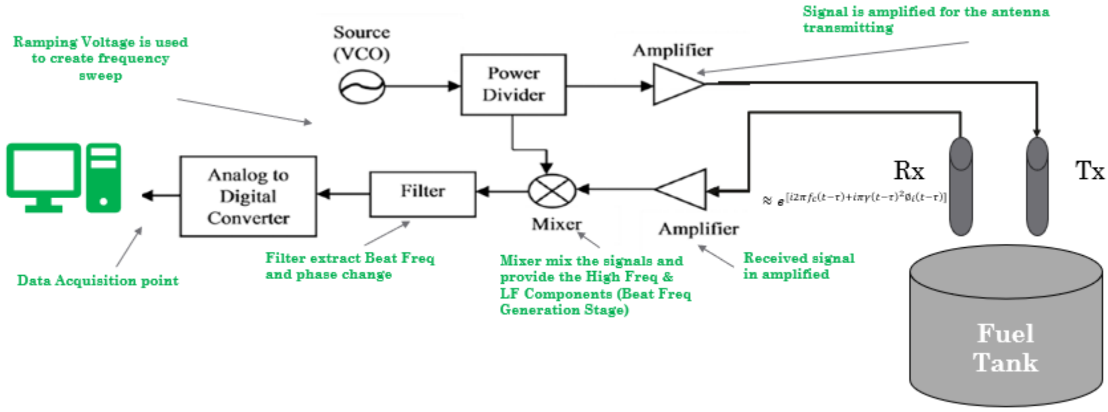

Figure 3.19. Schematic Diagram of the FMCW Radar setup in the lab

Table 3-1 summarizes the key performance parameters of the developed FMCW radar prototype. The radar operates over a center frequency band from 2.3 GHz to 2.6 GHz, with an effective modulation bandwidth of 300 MHz. It supports a frequency sweep range of 10 MHz, enabling high-resolution measurements across the target medium. The transmitted signal follows a triangular frequency modulation profile, which ensures linear up- and down-chirp behavior necessary for accurate beat frequency extraction. These operational parameters provide a solid foundation for precise distance and contamination-level estimation in the experimental setup.

Radar performance parameters.

Important Parameters	Values
Frequency Interval	2300–2600-2300 MHz
Bandwidth	300 MHz
Frequency Sweep	10 MHz
Waveform	Triangular FMCW

Table 3-1. Specifications of FMCW Radar

3.4.4.1 Laboratory Setup - Model of the FMCW Radar for Motor Oil Measurements

During the preliminary testing phase, the experimental tanks were filled with controlled volumes of motor oil and water to evaluate the system's detection capability. Motor oil was utilized instead of diesel for safety considerations, as its dielectric permittivity closely approximates that of diesel fuel. Various configurations were examined, including pure motor oil (control), mixed oil–water layers, and empty tank conditions to establish reference benchmarks. To minimize electromagnetic reflections and stray interference, an absorbing foam layer was positioned beneath the tank. The test tank used in this stage measured 25 cm × 15 cm × 10 cm and was placed directly below the transmitting and receiving antennas of the FMCW radar to ensure consistent geometric alignment and repeatability of measurements. In **Figure 3.20**, the real tank and its dimensions are illustrated.

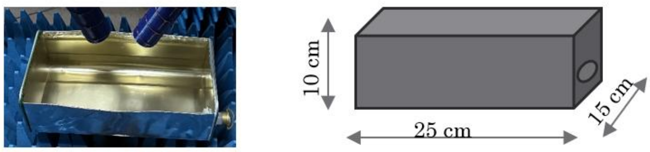

Figure 3.20. Tank used in preliminary measurements with Motor Oil

3.4.4.2 Measurements with Motor Oil

The experimental procedure was conducted in several sequential steps to establish reliable reference benchmarks and analyze radar signal behavior under controlled conditions. **Figure 3.21** shows the setup after locating the Motor Oil Tank below the Radar probes.

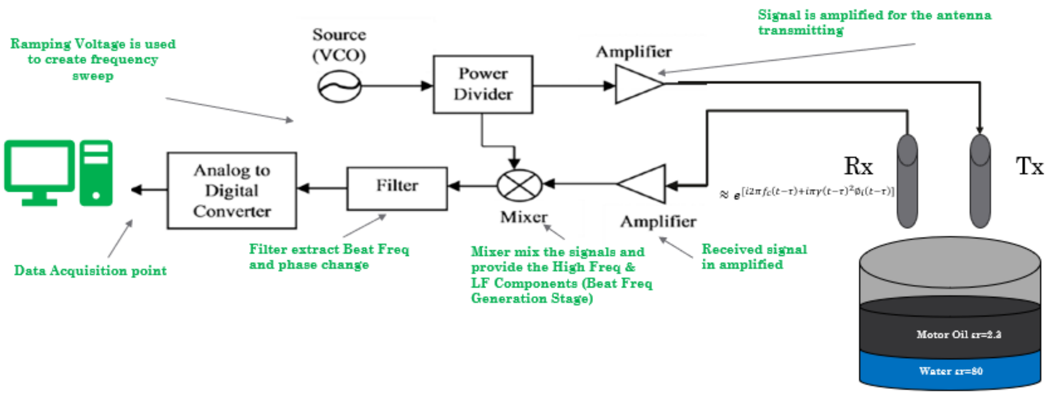

Figure 3.21. FMCW Radar Setup after locating Motor Oil Tank

Test was made on several steps:

3.4.4.2.1 Step 1

Initially, no tank was placed in the measurement area. The transmitting (TX) and receiving (RX) antennas were directed toward a radio-absorbing foam layer to simulate a condition with no reflection. The foam absorbed nearly all incident electromagnetic energy, resulting in an almost negligible received signal. This configuration served as a baseline reference to represent the case of zero reflection. In Figure 3.22, it illustrates the antenna setup and the absorption layer during this stage.

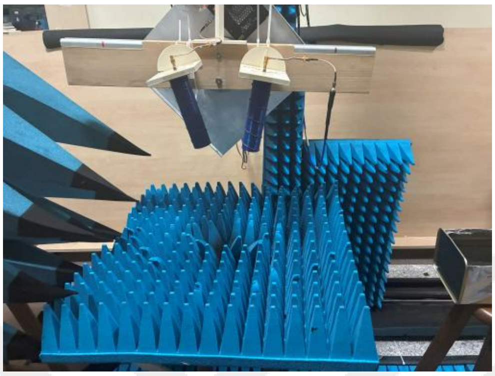

Figure 3.22. Measurement Setup with Absorption Foam Only

3.4.4.2.2 Step 2:

The second configuration involved directly connecting the TX and RX cables, ensuring complete signal transfer without propagation losses. This setup generated a benchmark representing full reflection or total reception of the transmitted signal. It served as an upper reference limit for subsequent measurements. in **Figure 3.23** illustrates this configuration, showing the direct connection between TX and RX coaxial cables.

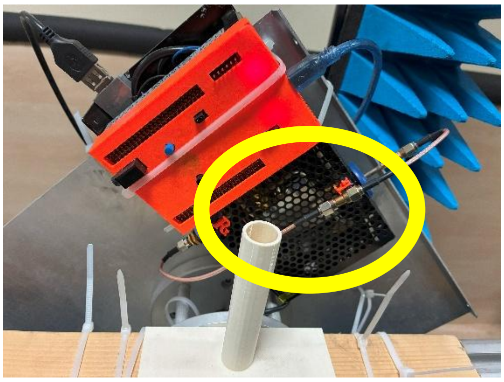

Figure 3.23. Measurement Setup with Tx and Rx connected for full signal reception

3.4.4.2.3 Step 3

In the third step, an empty metallic tank was positioned beneath the radar antennas. The transmitted signal was directed toward the tank's inner surface, and the received response was recorded to characterize background reflections without any liquid present. Figure 3.24 illustrates that clearly.

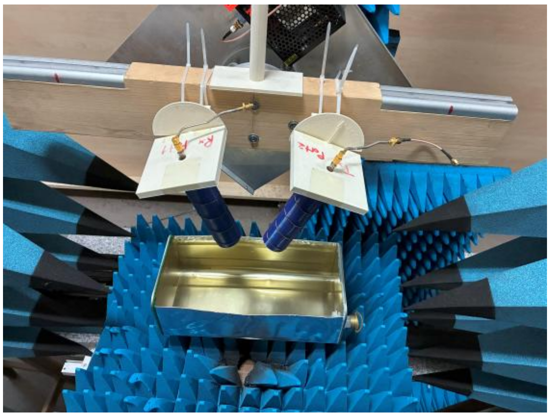

Figure 3.24. Measurement Setup with only Empty Tank

3.4.4.2.4 Step 4

The next stage involved filling the tank with 6 cm of pure motor oil to establish the reference response for uncontaminated fuel. The tank was placed over the absorbing foam to minimize stray reflections, and the received signal was recorded and analyzed using processing software connected to the FMCW radar system. Figure 3.14 illustrates this setup. In Figure 3.25 it's illustrated how the tank is positioned below the TX and RX antennas of the FMCW radar.

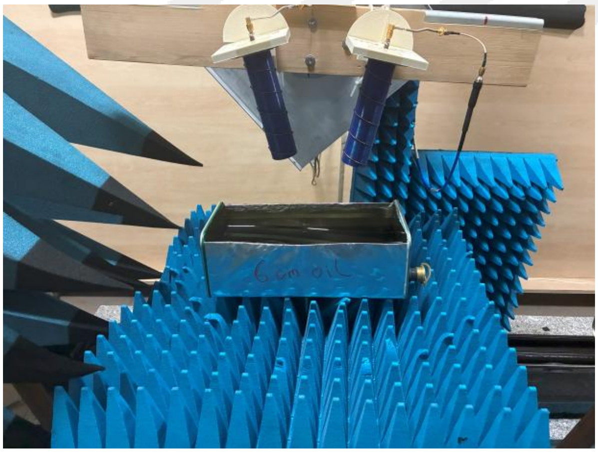

Figure 3.25. Measurement Sample with 6cm of Pure Motor Oil

3.4.4.2.5 Step 5

Finally, a mixed sample consisting of 3 cm of motor oil and 3 cm of water was prepared to simulate contamination conditions. Due to density differences, the oil formed the upper layer while the water settled at the bottom. The total liquid height was maintained at 6 cm, consistent with the previous test, ensuring comparable geometric conditions. This configuration was used to verify the radar's ability to detect the interface between the two liquids through phase and amplitude variations. In Figure 3.26 It is illustrated that we located the tank above that foam layer and we fill it with the mix mentioned above and the tank is located below both the TX and RX signals

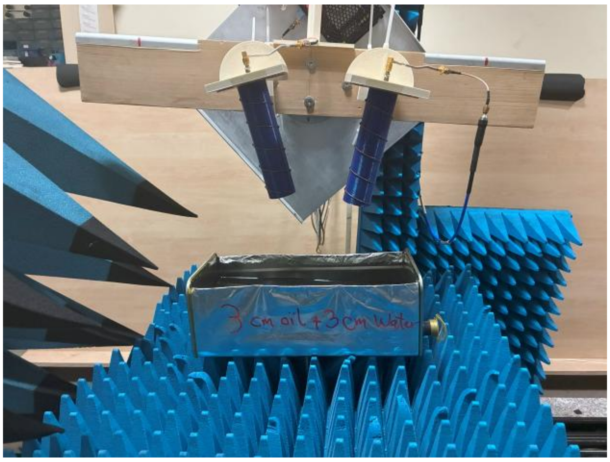

Figure 3.26. Measurement Sample with 3cm of Oil + 3 cm of water

3.4.4.2.6 Data Collection

The file generated by the Python code described above is a Microsoft Excel spreadsheet containing tabulated data recorded during one of the FMCW radar test sessions. The file is structured in two primary columns, Each row represents one measurement entry, forming a simple two-column dataset. The numerical values are formatted in standard decimal notation. The file name follows the convention "date–time – test condition.xlsx", The file has been generated automatically by the radar control software, as part of a batch data export process. The workbook consists of a single worksheet, containing no formulas, macros, or embedded objects — only raw numeric data. The file is compatible with Microsoft Excel, OpenOffice Calc, and similar spreadsheet software.

3.4.4.2.7 Description of Python software code

A custom Python application was developed to control, acquire, and visualize data from an FMCW radar module through a graphical user interface (GUI). The system establishes serial communication between the radar and a host computer via a COM port, enabling the transmission of user-defined signal parameters such as minimum and maximum frequencies, waveform type, and sweep period. The GUI allows interactive configuration of radar parameters through sliders and buttons for measurement, plotting, and system control. The program generates frequency-modulated chirp signals by calculating the corresponding DAC voltage values using a dedicated FMCW signal-processing library. The acquired analog responses are digitized through an ADC, stored in Excel files with timestamped filenames. The software architecture supports triangular, rectangular, and sawtooth modulation schemes and includes safety checks for parameter consistency. Overall, the application provides a complete environment for FMCW radar testing, calibration, and single-shot measurement acquisition.

3.4.4.3 Laboratory Setup - Model of the FMCW Radar for Diesel Measurements

Following the completion of all motor oil measurements, the experimental setup was upgraded for testing with real diesel fuel, while ensuring all previously outlined safety precautions were strictly observed. Since diesel measurements represent the primary focus of this research, a wider tank was introduced to enhance precision, minimize near-field and wall reflection effects, and better replicate real-world fuel storage conditions. In Figure 3.27, The new FMCW radar setup is illustrated after replacing the motor oil tank with a diesel tank.

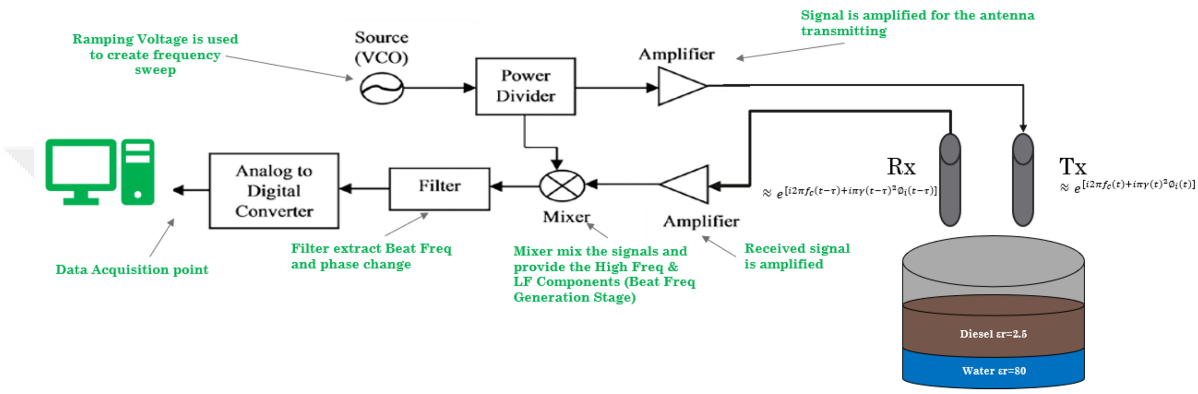

Figure 3.27. FMCW Radar Setup after locating Diesel Tank

To ensure comparability, the new diesel tank design was evaluated against the smaller tank used for motor oil tests (Figure 3.28). The upgraded tank measures 40 cm × 40 cm at the base and 20 cm in height, and includes a transparent column that facilitates precise monitoring of diesel and water levels. Unlike motor oil, diesel's natural transparency enables direct visual inspection through the column.

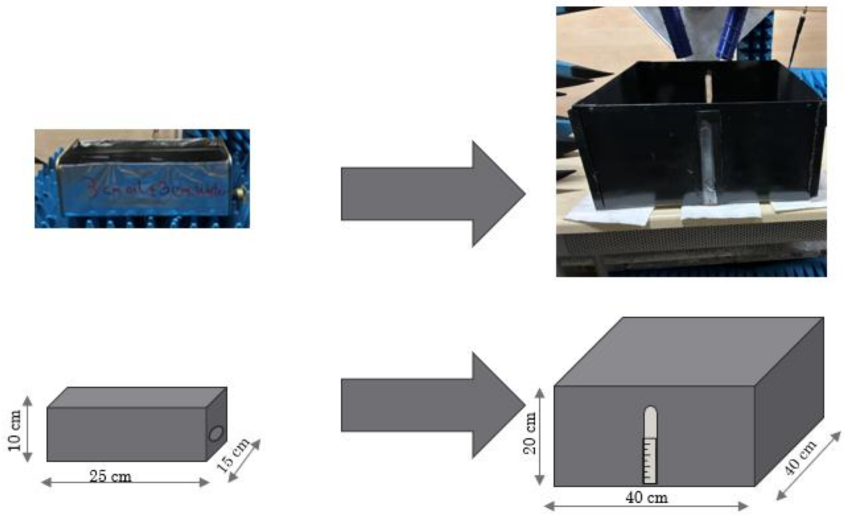

Figure 3.28. Upgrade of the Tank for Diesel Measurements

A limitation of the larger tank is the reduced level resolution resulting from its wider base. To address this, a calibrated volumetric flask was employed, allowing controlled addition of fluid volumes. for example, if we have a swimming pool and we added 1 m^3 of water we may not notice any difference in the level because of the wide area of the base, And similarly we have the same precision issue in this tank. Based on tank geometry, each 2 mm increase in liquid height corresponds to approximately 320 mL of added fluid, as expressed in Equation (3.171). Figure 3.29 illustrates the calibration flask used for this process.

$$2mm \times 400\ mm \times 400mm \approx 320mL \tag{3.171}$$

1 mm of error in height in the filling flask can impact an error margin less than 9.6 micron (0.0096mm = 9.6×10^{-6} m) in the main tank which is negligible.

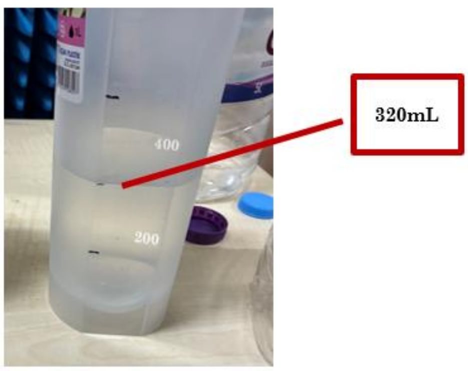

Figure 3.29. Calibration Flask to increase 2mm of height in Tank

The filing precision and the transparency of the measuring column help us with our naked eyes to distinguish between the diesel layer and the water layer as shown in Figure 3.30

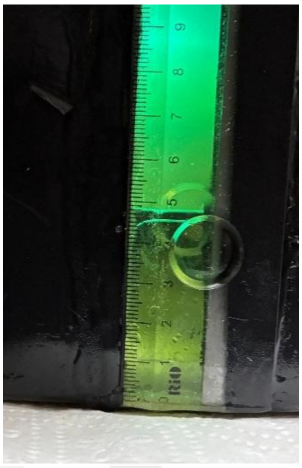

Figure 3.30. Random sample of Diesel and Water (layers are clearly shown)

3.4.4.4 Measurements with Diesel

Using the experimental configuration described above, the measurement process was initiated. The FMCW radar transmitted and received signals vertically toward the tank, as illustrated in the preceding figures. The experimental procedure was conducted in multiple steps, following a methodology like that previously applied during the motor oil measurements, as outlined below.

3.4.4.4.1 Step 1

Since the baseline measurements without a tank had already been performed in the previous experiment—where the antennas were directed toward the RF-absorbing foam to ensure zero reflection—there was no need to repeat this step. Therefore, the previously obtained data were adopted as the baseline reference for this stage, as illustrated in **Figure 3.22**.

3.4.4.4.2 Step 2

In Step 2, the TX and RX antennas of the FMCW radar were directly connected to establish a full-reflection condition. Since this configuration had already been implemented during previous measurements, the same data were utilized for this experimental stage as well, as illustrated in Figure 3.23.

3.4.4.4.3 Step 3

In step 3 it's similar to Step 3 in the motor oil measurement, it only include directing the TX and RX antennas toward an empty tank with the new size and design, we do not expect any difference in the measurements we have than what we get from Step 3 in motor oil measurements, because in both cases we have reflection from a wide metal surface. In **Figure 3.31** Below it is shown that the tank was placed just below the antenna during its empty state, as the level is sensitive whenever we use a wide tank we used to ensure that the tank is accurately leveled in order to avoid an inclined bottom of the tank, it's clear in the figure that we use A bubble level (the yellow instruments in the right of the figure), It will help us to ensure precision with the measurements once we started to add small amounts of liquid, which may concentrate in one of the sides of the tank instead of spreading on the whole base.

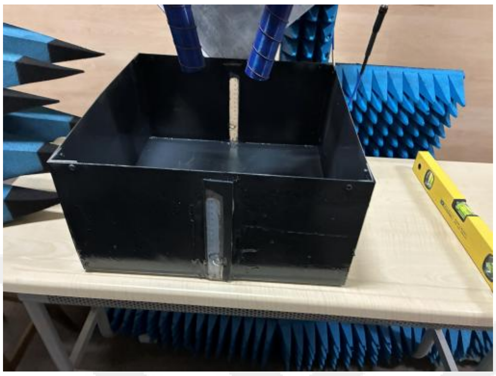

Figure 3.31. Diesel Measurement Setup with only Empty Tank

3.4.4.4.4 Step 4

In Step 4, the procedure shares conceptual similarities with Step 4 of the motor oil measurements; however, several methodological refinements were introduced to enhance precision. While the motor oil experiment involved a single measurement at a 6 cm liquid height, the diesel experiment aimed to achieve higher resolution and precision. Accordingly, the diesel level was incremented in 2 mm steps until reaching a total height of 5 cm, resulting in 25 distinct measurement points. For each 2 mm increment, 320 mL of diesel was added to the tank, followed by a full measurement cycle. This iterative and finely resolved procedure is illustrated in the left half of the graph in Figure 3.32, with ten repeated measurements acquired for each level to ensure statistical reliability.

3.4.4.4.5 Step 5

In Step 5, there are notable similarities between the measurements conducted in motor oil and diesel. Specifically, both procedures involve the simultaneous presence of two fluids within the same tank. However, consistent with Step 4 in the diesel measurements, a gradual increase in fluid level was implemented to achieve higher resolution, using 2 mm increments. To incorporate this, water was gradually added once the diesel level reached 5 cm. By applying 2 mm increments over 25 samples, the water level reached an additional 5 cm, resulting in a total fluid height of 10 cm, evenly split between diesel and water. This iterative process is depicted in the right half of **Figure 3.32**. At each level, ten measurements were collected.

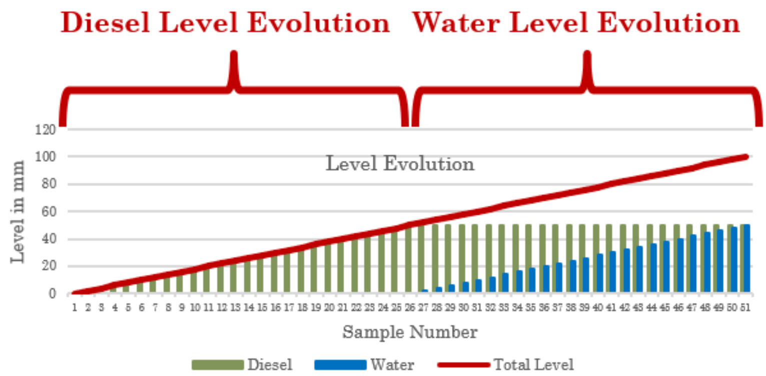

Figure 3.32. Liquid Level Evolution vs sample number

3.4.4.4.6 Data Collection

The Python script employed for data acquisition in the motor oil measurements has been enhanced. Previously, the output was organized in a two-column format, corresponding to an individual recorded sample. The output has now been transposed so that each row contains a complete set of measurements representing a specific fluid level (either diesel or water). This revised structure facilitates subsequent advanced analyses using MATLAB® software.

3.4.4.4.7 Description of Python software code

To streamline the experimental measurements and improve efficiency—given that the number of samples increased tenfold, resulting in 51 measurements, the Python code was upgraded. The revised code consolidates all measurements into a single file, thereby simplifying data processing and eliminating the need to manage 50 separate Excel files.

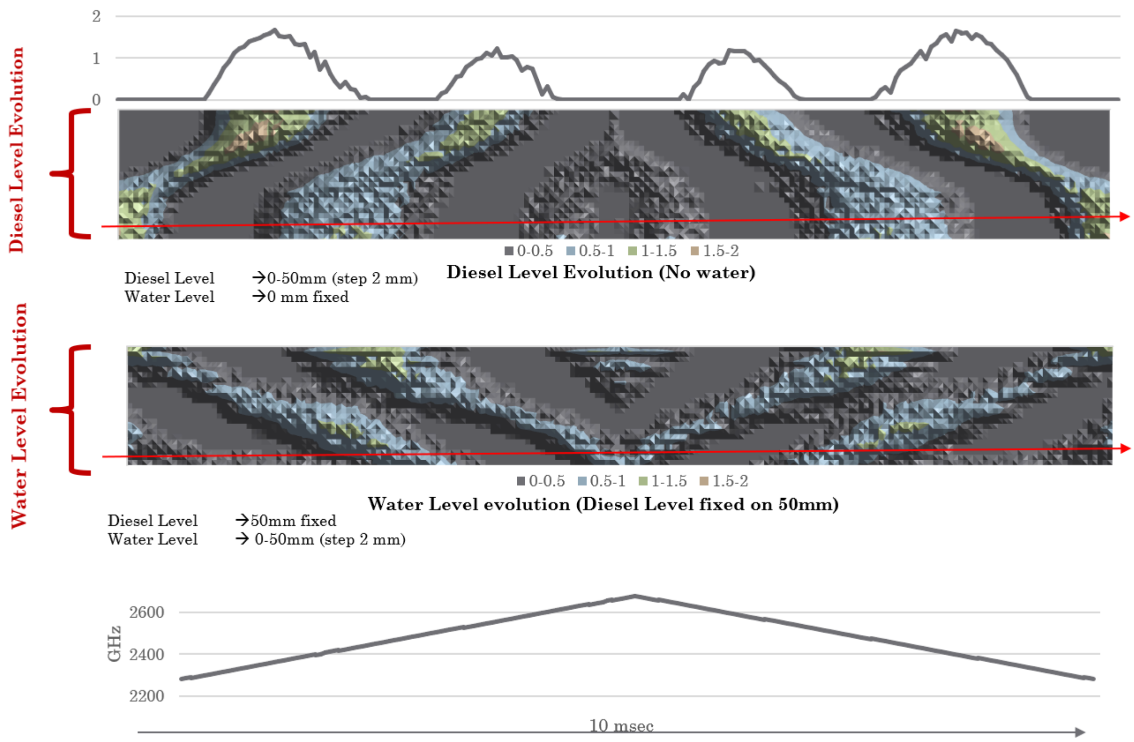

Figure 3.33 - Graphical Representation of the Data Model

In **Figure 3.33**, the data is represented in 2 sections, the upper one represents the pure data samples in graphical, the below is for the contaminated. These are the samples collected when we transmit the pyramidal modulated FMCW radar wave shown in the same figure.

4 MEASUREMENTS FINDINGS

4.1 MATLAB Simulation Findings

Simulation results highlighted clear phase shifts in the reflected signal as the water level increased beneath the diesel. By incrementing contamination levels in millimeter steps, the simulation demonstrated a consistent correlation between fluid depth and signal phase.

Plots of electric field versus depth and time indicated increased signal distortion as water content grew. These findings validated the theoretical model and provided a benchmark for CST simulations and practical data.

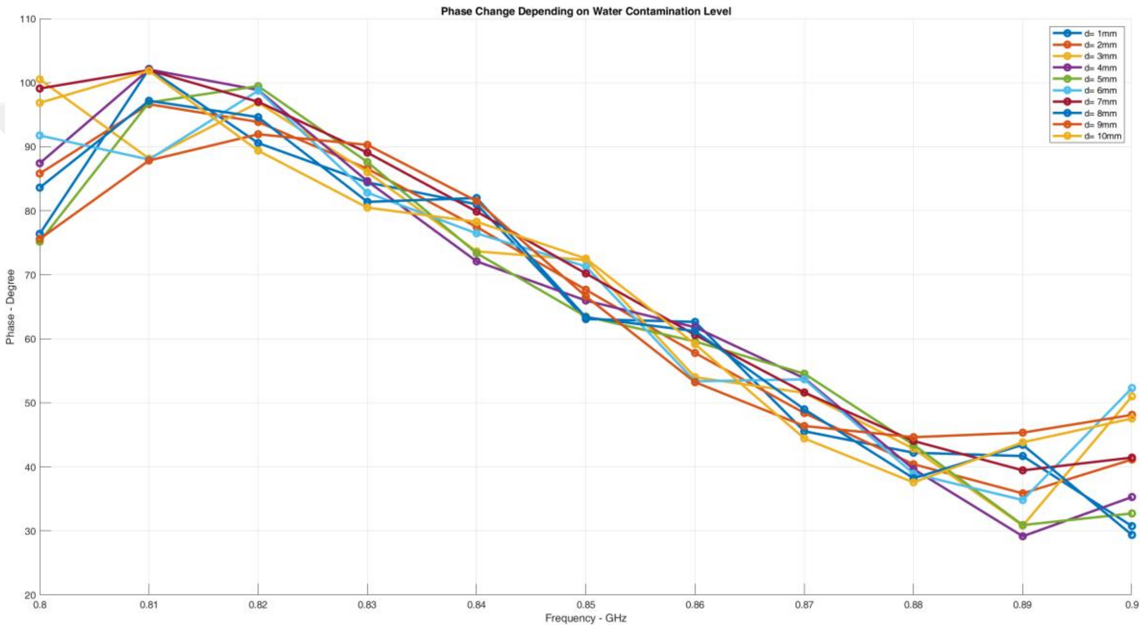

Figure 4.1. Phase change due to change in water level under the diesel layer

4.2 CST Software Modeling Findings

CST results reinforced MATLAB findings. Probes recorded variations in electric field strength at different media boundaries. The black line in simulation outputs represented electric field magnitude within the water layer, confirming its distinguishable signature due to higher permittivity.

Experiments included simulations with mineral oil, custom dielectric properties, and air. While not exact, these approximations illustrated the layered system's electromagnetic behavior and revealed how each interface altered the waveform structure.

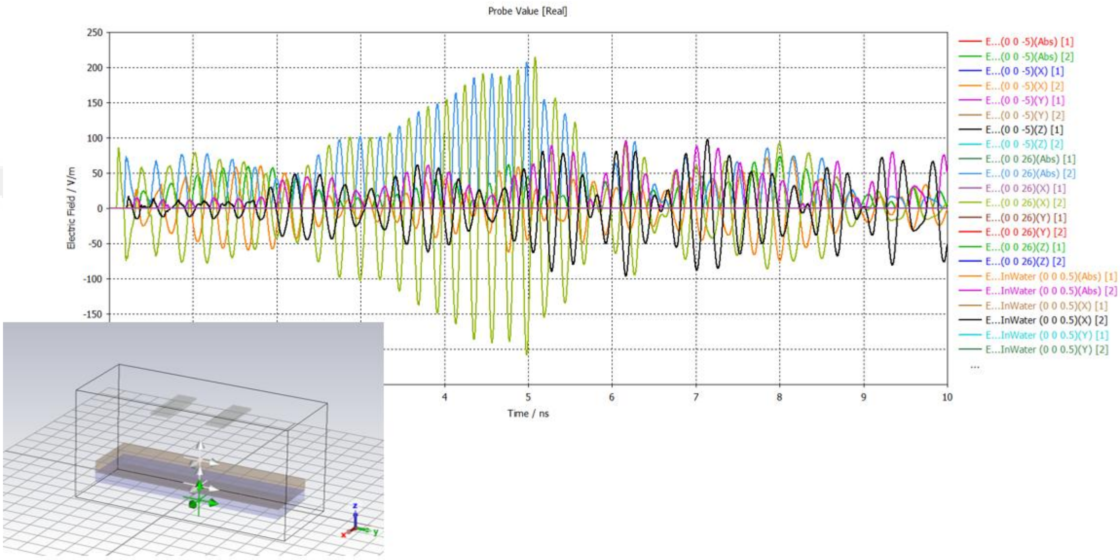

Figure 4.2. Probes values measuring Electric Field below each layer

4.3 Measurement with Motor Oil Findings

Real-world testing revealed significant insights. Beat frequency and signal phase were observed to change according to contamination levels. ADC outputs were normalized and analyzed for amplitude and phase shift. Limitations such as ADC inability to convert negative values were noted and accounted for through cosine function normalization.

Multiple test cases were compared: foam absorption, Total Reflection, empty tank, control tank (pure oil), and contaminated tank (oil + water). Each configuration displayed unique signal characteristics.

In **Figure 4.3**, it is quite clear that the measurement of contaminated oil is significantly different than that of pure oil, and there is no misleading with any other test samples or setups.

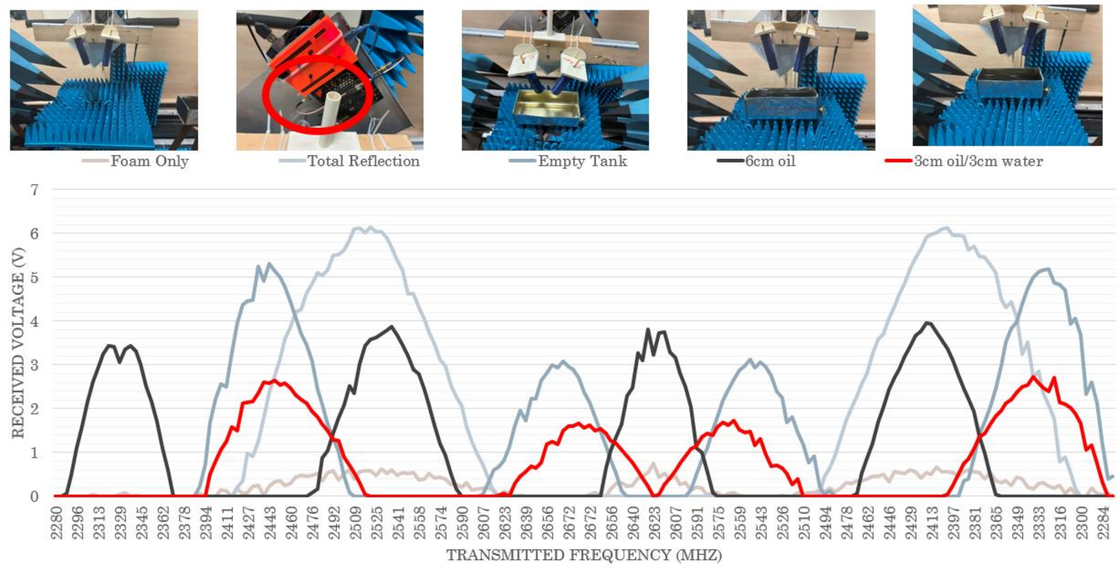

Figure 4.3. Different VCO output values collected in different measurement state

4.4 Measurement with Diesel Findings

Real-world testing revealed significant insights. Beat frequency and signal phase were observed to change according to contamination levels. ADC outputs were normalized and analyzed for amplitude and phase shift. Limitations such as ADC inability to convert negative values were noted and accounted for through cosine function normalization.

Multiple test cases were compared: foam absorption, short-circuit bypass, empty tank, control tank (pure oil), and contaminated tank (diesel + water). Each configuration displayed unique signal characteristics.

In **Figure 4.4**, it is quite clear that the measurement of contaminated diesel is significantly different than that of pure diesel, and there is no misleading with any other test samples or setups.

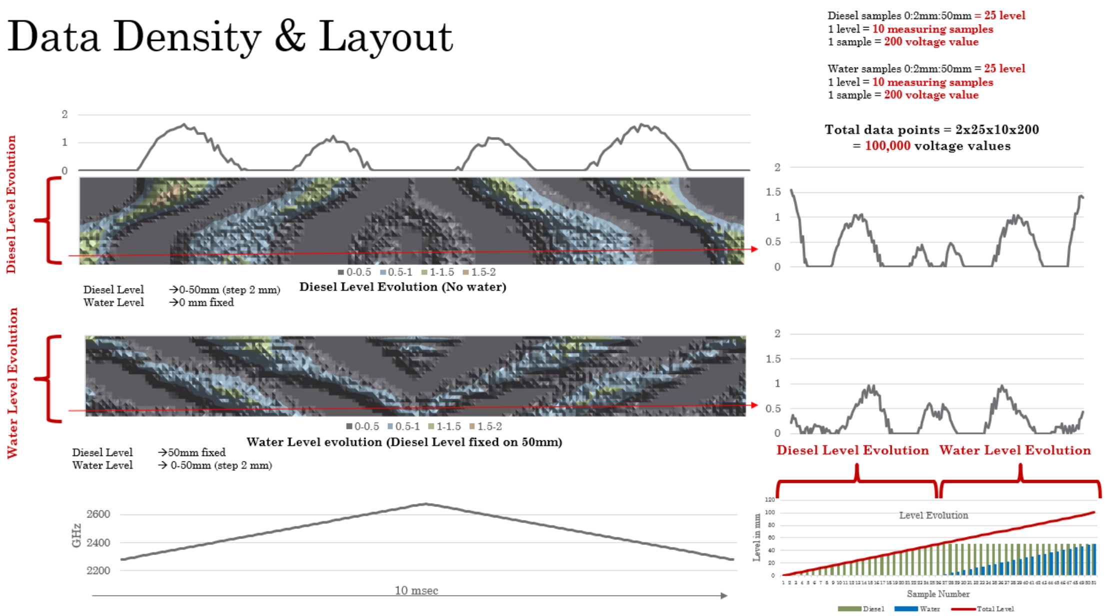

Figure 4.4. Graphical Representation of collected data

The Classifier Machine Learning techniques will be applied several times on full data or partial data on the next sections.

4.5 Applying Machine Learning on Data Collected

In order to take the analysis to a next level by applying Machine Learning in detection of the contamination state and the fluid level, we selected MATLAB as a common tool for machine learning to apply Classification Technique (MLCT) and Regression Technique (MLRT)

In **Figure 4.5** below, We can see how the predictors and responses are selected during our analysis, for responses sometimes we add the state (Contaminated/Pure), and sometimes we add the different level measurements we have (0mm, 2mm, 4mm, etc…), we aim by this technique to answer the following list of questions:

1. Can we detect “Contamination State” using MLCTs? (TRUE = Contaminated / FALSE = Pure)
2. Can we detect “Contamination Level” using MLCTs? Ex: Water Level≈ 26 mm
3. Can we detect “Diesel Fuel Level” using MLCTs? Ex: Diesel Level≈ 34 mm
4. Can we detect “Contamination Level” using MLRTs? Ex: Water Level≈ 18 mm
5. Can we detect “Diesel Fuel Level” using MLRTs? Ex: Diesel Level≈ 42 mm
6. Can we simplify data to 50% only and still can get accurate ML model?
7. Can we simplify data to 25% only and still can get accurate ML model?
8. Can we simplify data to 12.5% only and still can get accurate ML model?
9. Can we simplify data to 6.25% only and still can get accurate ML model?
10. Can we simplify data to 3.125% only and still can get accurate ML model?
11. Can we manipulate data (by replacing values with 0/1 or -1/1) and still can get accurate ML model?
12. Can we process data (by summing rows) and still can get accurate ML model?
13. Can we manipulate and process data (by replacing values with 0/1 or -1/1 then summing rows) and still can get accurate ML model?

We will use for our studies the following Models for Classification Techniques:

1. Binary GLM Logistic Regression
2. Discriminant
3. Efficient Linear SVM
4. Efficient Logistic Regression
5. Ensemble
6. Kernel
7. KNN
8. Naive Bayes
9. Neural Network
10. SVM
11. Tree

We are going also for Regression Techniques the following Models:

1. Binary GLM Logistic Regression
2. Discriminant
3. Efficient Linear SVM
4. Efficient Logistic Regression
5. Ensemble
6. Kernel
7. KNN
8. Naive Bayes
9. Neural Network
10. SVM
11. Tree

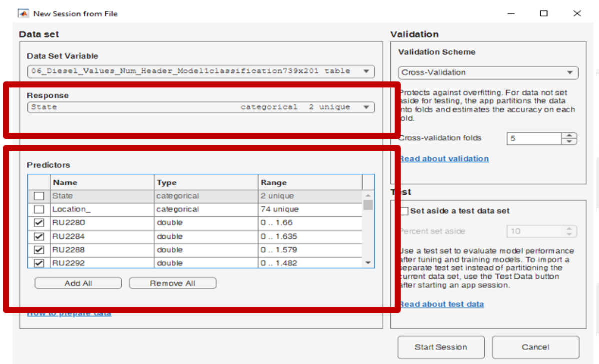

Figure 4.5. Machine Learning Model Configuration in MATLAB

4.5.1 Applying MLCT on Water Contamination Detection

Referring to the collected data structure, we have a unique excel sheet that includes 1 row per measurement, and in the columns, we add the state (pure/contaminated), diesel height, water height, and the specific output of the analog to digital converter.

Using this data structure, we can answer the previously mentioned research questions, as shown in **Figure 4.6**, To apply the MLCT learner on the water contamination state, we must split the data between two states (Pure & Contaminated).

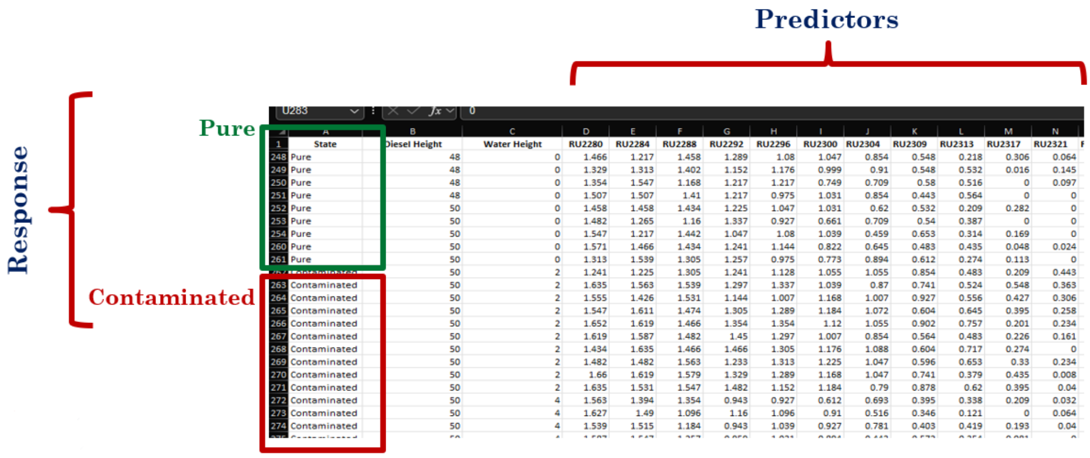

	State	Diesel Height	Water Height	RU2280	RU2284	RU2288	RU2292	RU2296	RU2300	RU2304	RU2309	RU2313	RU2317	RU2321
248	Pure	48	0	1.466	1.217	1.458	1.289	1.08	1.047	0.854	0.548	0.218	0.306	0.064
249	Pure	48	0	1.329	1.313	1.402	1.152	1.176	0.999	0.91	0.548	0.532	0.016	0.145
250	Pure	48	0	1.354	1.547	1.168	1.217	1.217	0.749	0.709	0.58	0.516	0	0.097
251	Pure	48	0	1.507	1.507	1.41	1.217	0.975	1.031	0.854	0.443	0.564	0	0
252	Pure	50	0	1.458	1.458	1.434	1.225	1.047	1.031	0.62	0.532	0.209	0.282	0
253	Pure	50	0	1.482	1.265	1.16	1.337	0.927	0.661	0.709	0.54	0.387	0	0
254	Pure	50	0	1.547	1.217	1.442	1.047	1.08	1.039	0.459	0.653	0.314	0.169	0
260	Pure	50	0	1.571	1.466	1.434	1.241	1.144	0.822	0.645	0.483	0.435	0.048	0.024
261	Pure	50	0	1.313	1.539	1.305	1.257	0.975	0.773	0.894	0.612	0.274	0.113	0
[illegible]	Contaminated	50	2	1.241	1.225	1.305	1.241	1.128	1.055	1.055	0.854	0.483	0.209	0.443
263	Contaminated	50	2	1.635	1.563	1.539	1.297	1.337	1.039	0.87	0.741	0.524	0.548	0.363
264	Contaminated	50	2	1.555	1.426	1.531	1.144	1.007	1.168	1.007	0.927	0.556	0.427	0.306
265	Contaminated	50	2	1.547	1.611	1.474	1.305	1.289	1.184	1.072	0.604	0.645	0.395	0.258
266	Contaminated	50	2	1.652	1.619	1.466	1.354	1.354	1.12	1.055	0.902	0.757	0.201	0.234
267	Contaminated	50	2	1.619	1.587	1.482	1.45	1.297	1.007	0.854	0.564	0.483	0.226	0.161
268	Contaminated	50	2	1.434	1.635	1.466	1.466	1.305	1.176	1.088	0.604	0.717	0.274	0
269	Contaminated	50	2	1.482	1.482	1.563	1.233	1.313	1.225	1.047	0.596	0.653	0.33	0.234
270	Contaminated	50	2	1.66	1.619	1.579	1.329	1.289	1.168	1.047	0.741	0.379	0.435	0.008
271	Contaminated	50	2	1.635	1.531	1.547	1.482	1.152	1.184	0.79	0.878	0.62	0.395	0.04
272	Contaminated	50	4	1.563	1.394	1.354	0.943	0.927	0.612	0.693	0.395	0.338	0.209	0.032
273	Contaminated	50	4	1.627	1.49	1.096	1.16	1.096	0.91	0.516	0.346	0.121	0	0.064
274	Contaminated	50	4	1.539	1.515	1.184	0.943	1.039	0.927	0.781	0.403	0.419	0.193	0.04

Figure 4.6. Predictors and Responses During Applying MLCT on the state

In **Figure 4.7** below, it is clearly shown the confusion matrix as one of the module training output, it represents the amount of correctly and wrongly identified responses, the true class contains the number of the real categorization of the original data, while the predicted class include the data predicted by the machine learning model, Once all values are allocated correctly (real contaminated samples are correctly predicted, And all real pure samples are correctly predicted), we can have 100% accuracy and no mis predicted samples which will exist in the white squares.

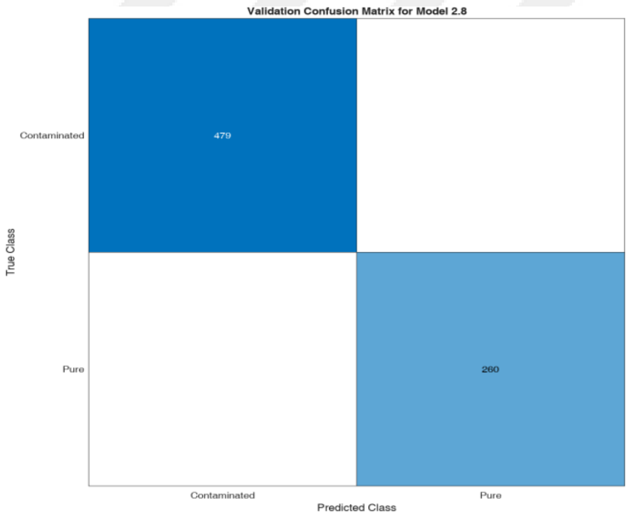

Figure 4.7. Confusion Matrix for Model 2.8 (Efficient Linear SVM)

We applied all available modules, and we obtained the accuracy level for each module as shown in **Figure 4.8**, the models are numbered and color coded as per the legend in the figure

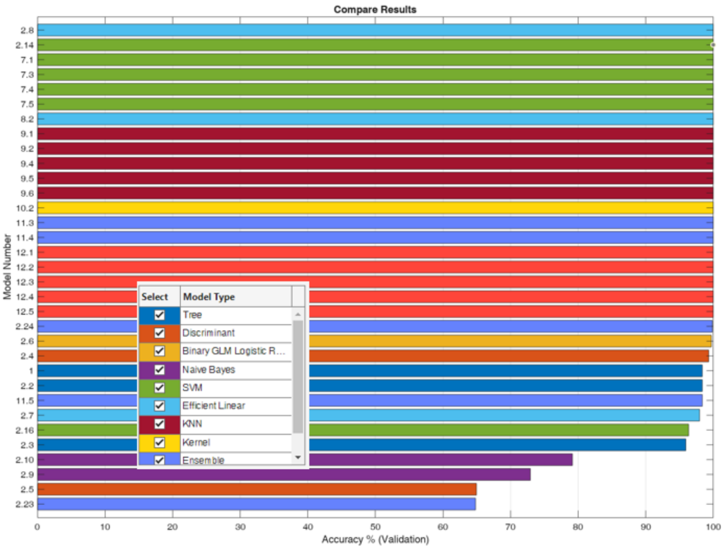

Figure 4.8. Accuracy Obtained by Applying MLCT on States with Full Data

4.5.2 Applying MLCT on Water Level

Using the same data structure, we applied MLCT on contaminated samples only to estimate the water level on the tank, as shown in **Figure 4.9**.

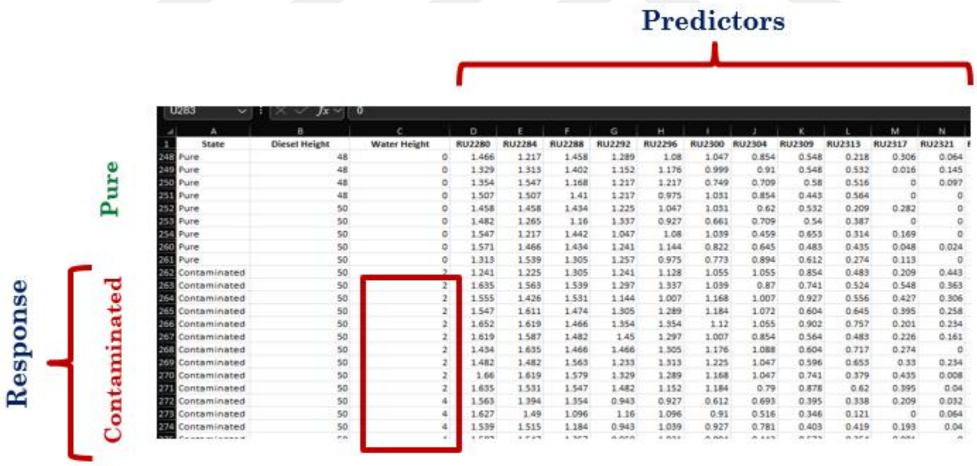

Figure 4.9. Predictors and Responses During Applying MLCT on The Contamination Only to Water Level

We have in this analysis one response per each level value (2mm, 4mm, 6mm, etc…), We are targeting to classify the samples that include the same water contamination level, And accordingly, we can train the model that can estimate the water contamination level. In **Figure 4.10**, It is clearly shown that most of the trained model succeeded to achieve 100% accuracy, which indicates a good chance over realizing the solution. In **Figure 4.11**, The confusion matrix clearly illustrates the classification of the samples as per the level value, we have ideal prediction of all values which indicates the successful training.

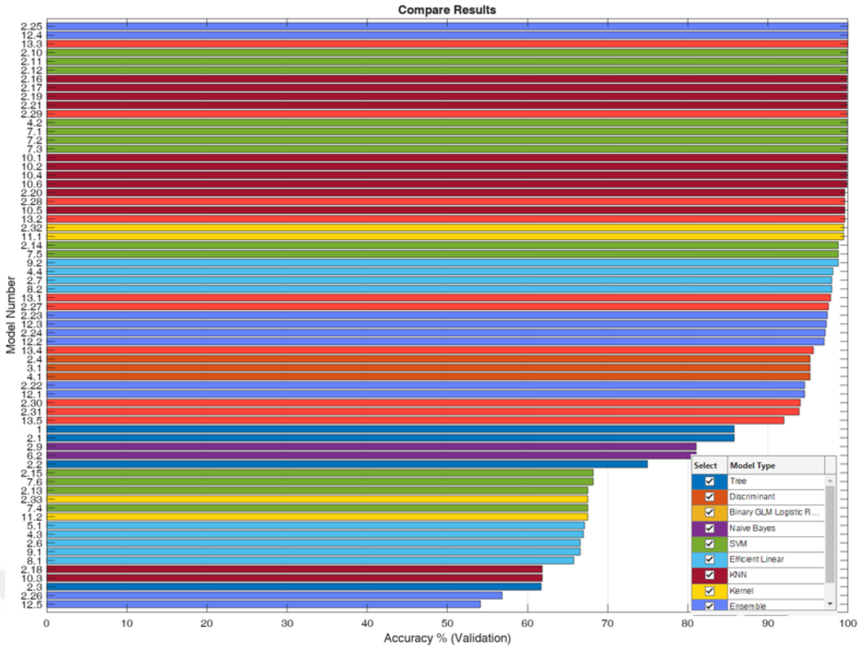

Figure 4.10. Accuracy Obtained by Applying MLCT on Water Level with Full Data

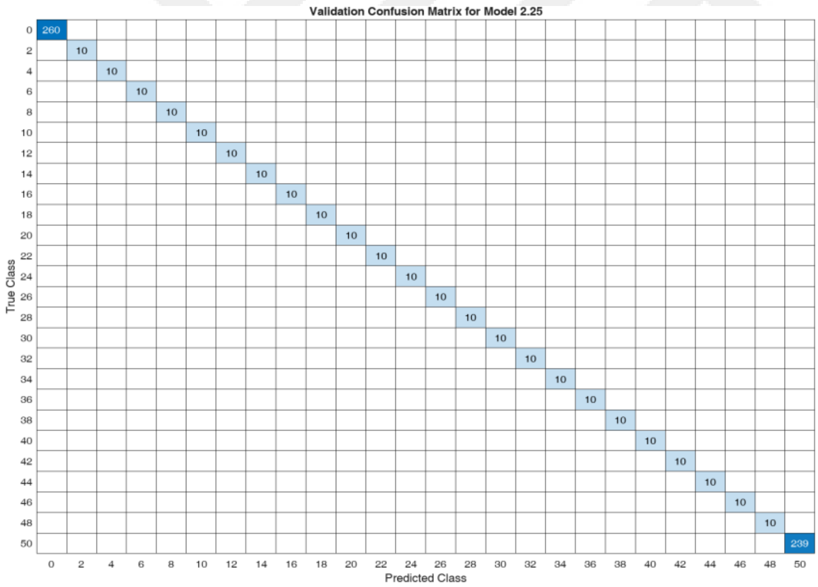

Figure 4.11. Confusion Matrix for Model 2.25

4.5.3 Applying MLCT on Diesel Level

Using the same data structure, we applied only on pure samples only to estimate the diesel level on the tank, as shown in **Figure 4.12**. We are targeting by this analysis to check the feasibility to use the solution as a "Level Transducer" OK to measure the level of the fuel in the tank and replace traditional level measurements, by the module on the diesel samples and we expect the model to classify values per the diesel height values. In **Figure 4.13**, The accuracy comparison chart is illustrated, its expertise to achieve 100%

accuracy, this could be resulted due to physical reasons, we are detecting these level which is the liquid with less permittivity, which mean that it has less reflection component compared to water and not easy to detect, the best model barely achieved 93% accuracy.

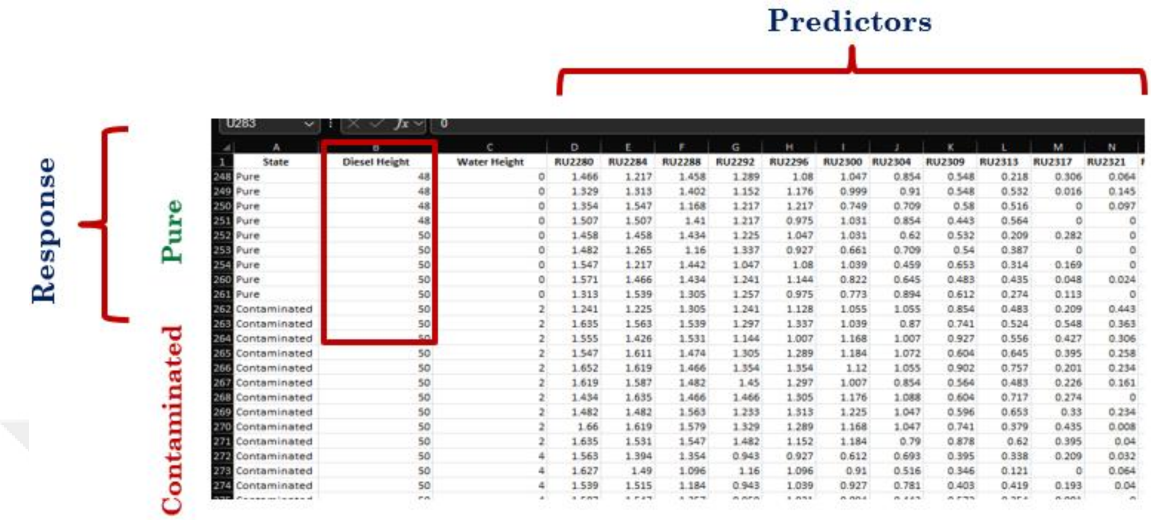

Figure 4.12 – Predictors and Responses During Applying MLCT on the Pure Diesel

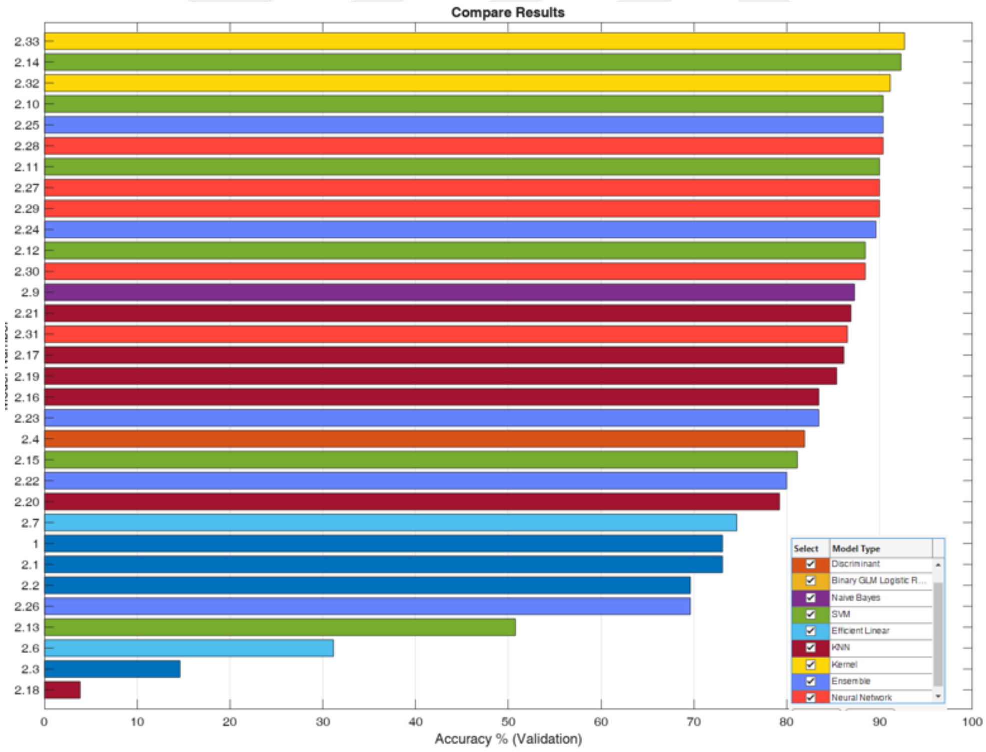

Figure 4.13 – Accuracy Obtained by Applying MLCT on Diesel Level with Full Data

By selecting the best model 2.33 to represent the model confusion matrix, we notice some outliers that could not correctly classify it, but it's in the acceptable level for industrial use.

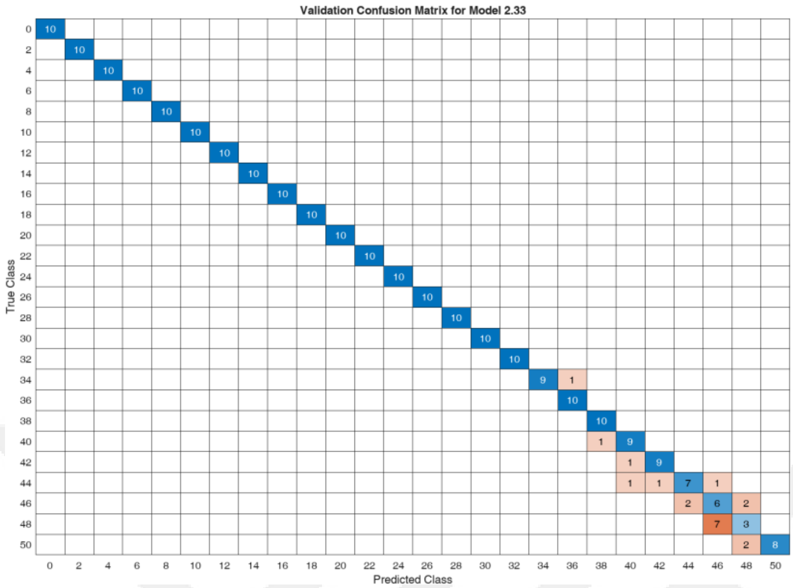

Figure 4.14. Confusion Matrix for Model 2.33

4.5.4 Applying MLRT on Water Contamination

Using the same data structure, we applied machine learning regression technique MLRT. We aim by this to build a model that can estimate and interpolate between all values of water level and help us to overcome precision barriers (step every 2mm of height). **Figure 4.15** Illustrates the model application zone for this analysis. In **Figure 4.16**, The R-Squared values For all trained models are clearly shown, it provides a scale of 0 to 1, which 1 means the best model with less errors, We have several models successfully achieved the value 1 and almost all models have good results, limited models couldn't achieve this good value but in general we have good level and feasibility.

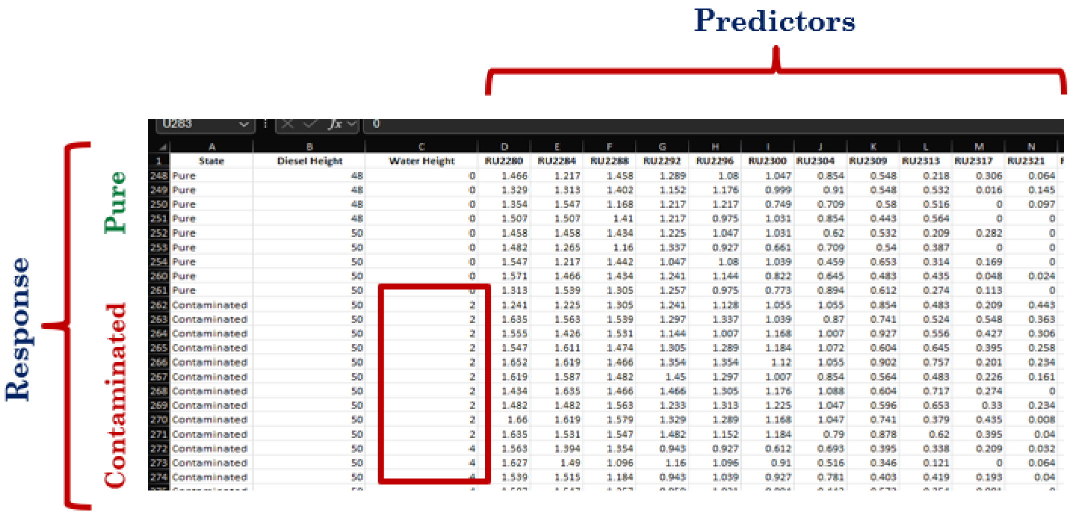

	State	Diesel Height	Water Height	RU2280	RU2284	RU2288	RU2292	RU2296	RU2300	RU2304	RU2309	RU2313	RU2317	RU2321
248	Pure	48	0	1.466	1.217	1.458	1.289	1.08	1.047	0.854	0.548	0.218	0.306	0.064
249	Pure	48	0	1.329	1.313	1.402	1.152	1.176	0.999	0.91	0.548	0.532	0.016	0.145
250	Pure	48	0	1.354	1.547	1.168	1.217	1.217	0.749	0.709	0.58	0.516	0	0.097
251	Pure	48	0	1.507	1.507	1.41	1.217	0.975	1.031	0.854	0.443	0.564	0	0
252	Pure	50	0	1.458	1.458	1.434	1.225	1.047	1.031	0.62	0.532	0.209	0.282	0
253	Pure	50	0	1.482	1.265	1.16	1.337	0.927	0.661	0.709	0.54	0.387	0	0
254	Pure	50	0	1.547	1.217	1.442	1.047	1.08	1.039	0.459	0.653	0.314	0.169	0
260	Pure	50	0	1.571	1.466	1.434	1.241	1.144	0.822	0.645	0.483	0.435	0.048	0.024
261	Pure	50	0	1.313	1.539	1.305	1.257	0.975	0.773	0.894	0.612	0.274	0.113	0
262	Contaminated	50	2	1.241	1.225	1.305	1.241	1.128	1.055	1.055	0.854	0.483	0.209	0.443
263	Contaminated	50	2	1.635	1.563	1.539	1.297	1.337	1.039	0.87	0.741	0.524	0.548	0.363
264	Contaminated	50	2	1.555	1.426	1.531	1.144	1.007	1.168	1.007	0.927	0.556	0.427	0.306
265	Contaminated	50	2	1.547	1.611	1.474	1.305	1.289	1.184	1.072	0.604	0.645	0.395	0.258
266	Contaminated	50	2	1.652	1.619	1.466	1.354	1.354	1.12	1.055	0.902	0.757	0.201	0.234
267	Contaminated	50	2	1.619	1.587	1.482	1.45	1.297	1.007	0.854	0.564	0.483	0.226	0.161
268	Contaminated	50	2	1.434	1.635	1.466	1.466	1.305	1.176	1.088	0.604	0.717	0.274	0
269	Contaminated	50	2	1.482	1.482	1.563	1.233	1.313	1.225	1.047	0.596	0.653	0.33	0.234
270	Contaminated	50	2	1.66	1.619	1.579	1.329	1.289	1.168	1.047	0.741	0.379	0.435	0.008
271	Contaminated	50	2	1.635	1.531	1.547	1.482	1.152	1.184	0.79	0.878	0.62	0.395	0.04
272	Contaminated	50	4	1.563	1.394	1.354	0.943	0.927	0.612	0.693	0.395	0.338	0.209	0.032
273	Contaminated	50	4	1.627	1.49	1.096	1.16	1.096	0.91	0.516	0.346	0.121	0	0.064
274	Contaminated	50	4	1.539	1.515	1.184	0.943	1.039	0.927	0.781	0.403	0.419	0.193	0.04

Figure 4.15. Applying MLRT on the Contamination Only to Detect Water Level

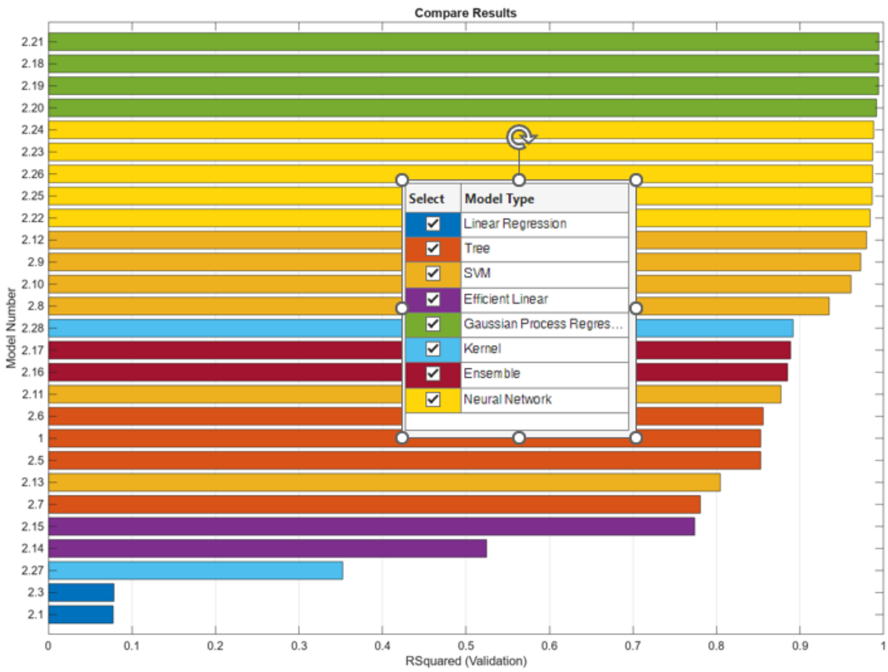

Figure 4.16. R-Squared for MLRT on the Contamination Only to Detect Water Level

In **Figure 4.17**, We obtained and illustrated the (Response Plot) Which demonstrates the relative position of the response points or values estimated for any model (for this example we represent Gaussian Process Regression). The best model is the model which coincides with the true data as much as possible, we obtained a very good result in model 2.21.

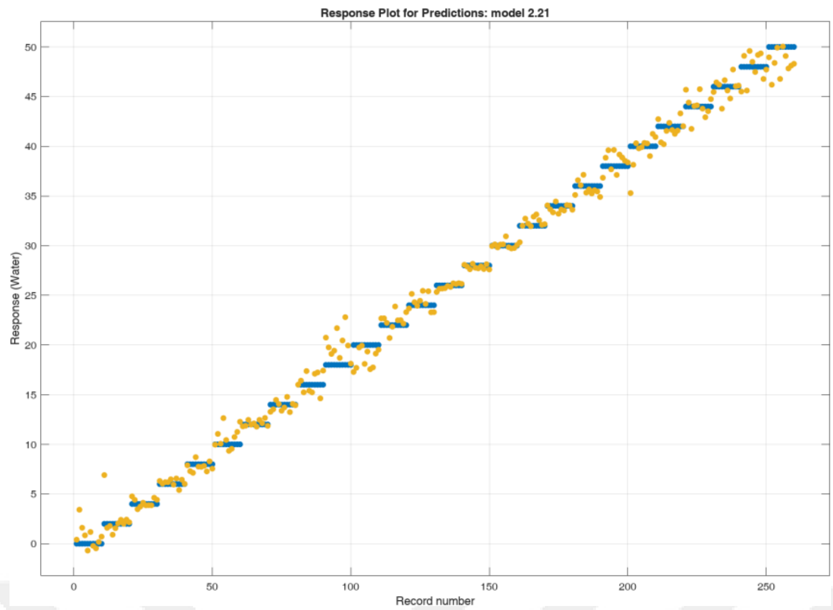

Figure 4.17. Response Plot for Regression for Model 2.21

4.5.5 Applying MLRT on Diesel Level

Using the same data structure, we applied machine learning technique and alert we aimed by this to build a model that can estimate and interpolate between all the values of these level, and can help us to overcome precision barriers (the 2mm of height), **Figure 4.18** Illustrates the model application zone of this analysis. In **Figure 4.19**, R-squared values For all trained models are displayed, We have most of the models with the value almost 1, and all models in general provide acceptable level of errors.

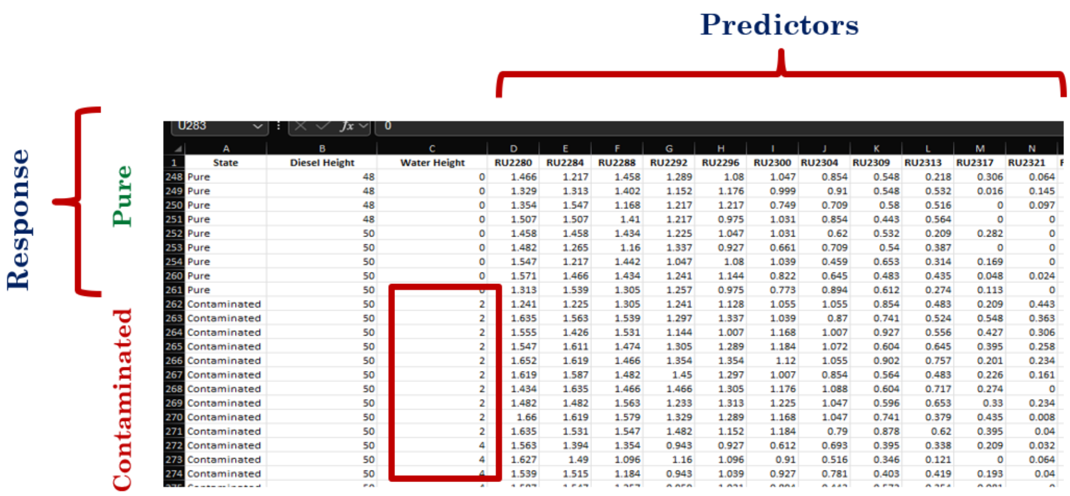

	A	B	C	D	E	F	G	H	I	J	K	L	M	N
1	State	Diesel Height	Water Height	RU2280	RU2284	RU2288	RU2292	RU2296	RU2300	RU2304	RU2309	RU2313	RU2317	RU2321
248	Pure	48	0	1.466	1.217	1.458	1.289	1.08	1.047	0.854	0.548	0.218	0.306	0.064
249	Pure	48	0	1.329	1.313	1.402	1.152	1.176	0.999	0.91	0.548	0.532	0.016	0.145
250	Pure	48	0	1.354	1.547	1.168	1.217	1.217	0.749	0.709	0.58	0.516	0	0.097
251	Pure	48	0	1.507	1.507	1.41	1.217	0.975	1.031	0.854	0.443	0.564	0	0
252	Pure	50	0	1.458	1.458	1.434	1.225	1.047	1.031	0.62	0.532	0.209	0.282	0
253	Pure	50	0	1.482	1.265	1.16	1.337	0.927	0.661	0.709	0.54	0.387	0	0
254	Pure	50	0	1.547	1.217	1.442	1.047	1.08	1.039	0.459	0.653	0.314	0.169	0
260	Pure	50	0	1.571	1.466	1.434	1.241	1.144	0.822	0.645	0.483	0.435	0.048	0.024
261	Pure	50	0	1.313	1.539	1.305	1.257	0.975	0.773	0.894	0.612	0.274	0.113	0
262	Contaminated	50	2	1.241	1.225	1.305	1.241	1.128	1.055	1.055	0.854	0.483	0.209	0.443
263	Contaminated	50	2	1.635	1.563	1.539	1.297	1.337	1.039	0.87	0.741	0.524	0.548	0.363
264	Contaminated	50	2	1.555	1.426	1.531	1.144	1.007	1.168	1.007	0.927	0.556	0.427	0.306
265	Contaminated	50	2	1.547	1.611	1.474	1.305	1.289	1.184	1.072	0.604	0.645	0.395	0.258
266	Contaminated	50	2	1.652	1.619	1.466	1.354	1.354	1.12	1.055	0.902	0.757	0.201	0.234
267	Contaminated	50	2	1.619	1.587	1.482	1.45	1.297	1.007	0.854	0.564	0.483	0.226	0.161
268	Contaminated	50	2	1.434	1.635	1.466	1.466	1.305	1.176	1.088	0.604	0.717	0.274	0
269	Contaminated	50	2	1.482	1.482	1.563	1.233	1.313	1.225	1.047	0.596	0.653	0.33	0.234
270	Contaminated	50	2	1.66	1.619	1.579	1.329	1.289	1.168	1.047	0.741	0.379	0.435	0.008
271	Contaminated	50	2	1.635	1.531	1.547	1.482	1.152	1.184	0.79	0.878	0.62	0.395	0.04
272	Contaminated	50	4	1.563	1.394	1.354	0.943	0.927	0.612	0.693	0.395	0.338	0.209	0.032
273	Contaminated	50	4	1.627	1.49	1.096	1.16	1.096	0.91	0.516	0.346	0.121	0	0.064
274	Contaminated	50	4	1.539	1.515	1.184	0.943	1.039	0.927	0.781	0.403	0.419	0.193	0.04

Figure 4.18. Predictors and Responses During Applying MLRT on the Diesel Only to Detect Diesel Level

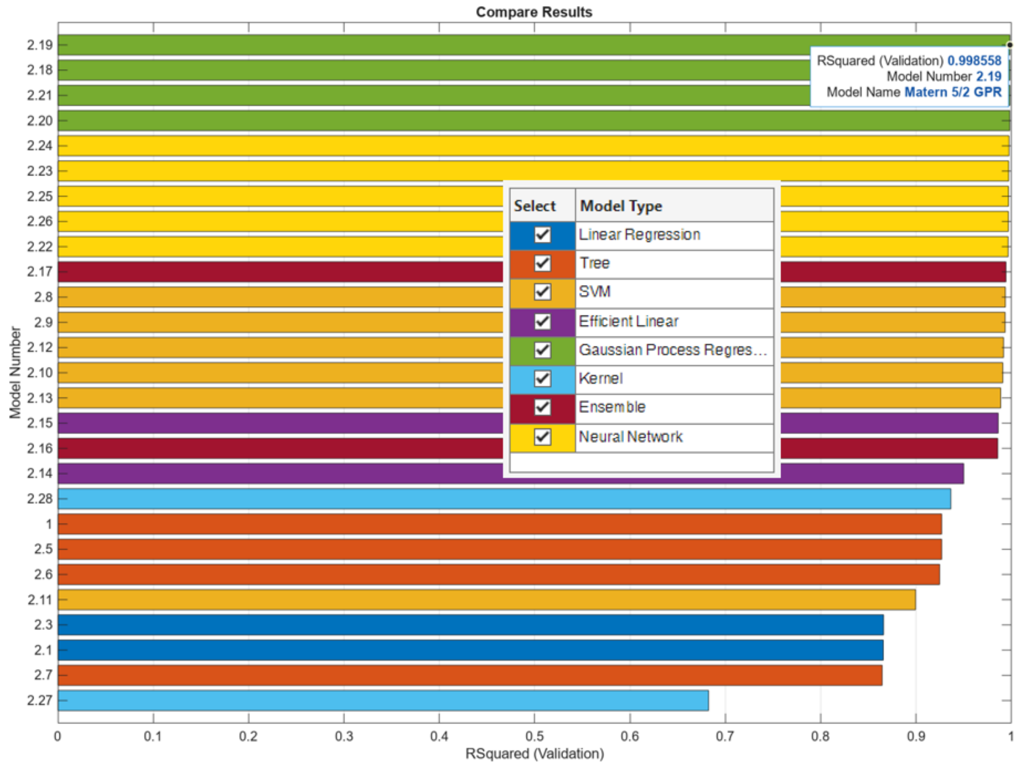

Figure 4.19. R-Squared Obtained by Applying MLRT on the Diesel Only to Detect Diesel Level

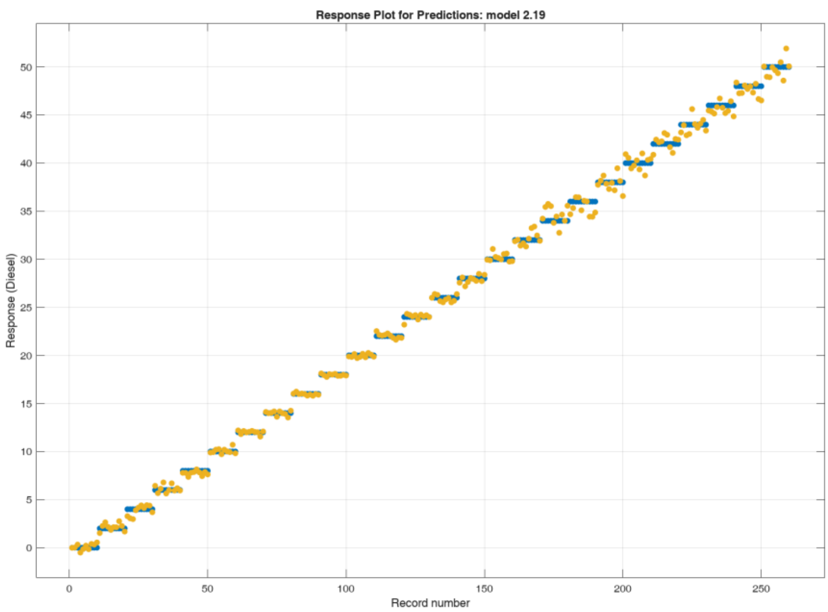

Figure 4.20. Response Plot for Regression for Model 2.19

In **Figure 4.20**, Response Plot for model 2.19 (Gaussian Process Regression) is displayed.

4.5.6 Data Simplification (Reduction) and Applying MLCT & MLRT

Referring to the fact that having 100% accuracy and less errors does not always mean that we have immunity against overfitting and "ready to go", We must take our analysis to the next level by manually eliminating amount of data and retrain the models, we expected by this to have minimum amount of data that marginally can provide accuracies less than 100%, once we have this we could achieve a target of data optimization and provide better immunity against overfitting, We met stepwise that reduction as per the following sections.

4.5.6.1 Applying Both Techniques on 50% of the Predictors

In order to reduce the number of predictors without having major effects on the data identity, we selected to eliminate every other column, so we keep a column and we eliminate the next one, so we can achieve 50% data reduction without being biased against response signal collected by the ADC of the setup, **Figure 4.21** Represents the columns to be eliminated to achieve this reduction.

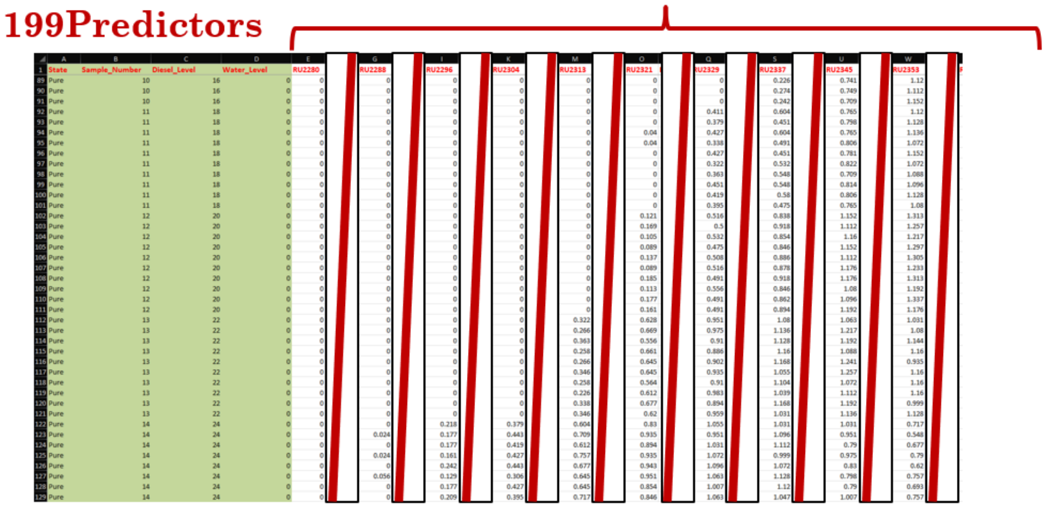

Figure 4.21. Reduction of Predictors to 50% Only

After running all the same machine learning techniques only reduce data, different accuracy on most of the models, which opened the doors for more data reduction, **Figure 4.22**. Comparison of Confusion Matrix and **Figure 4.23** Compare full data models against reduced data models (50% reduction).

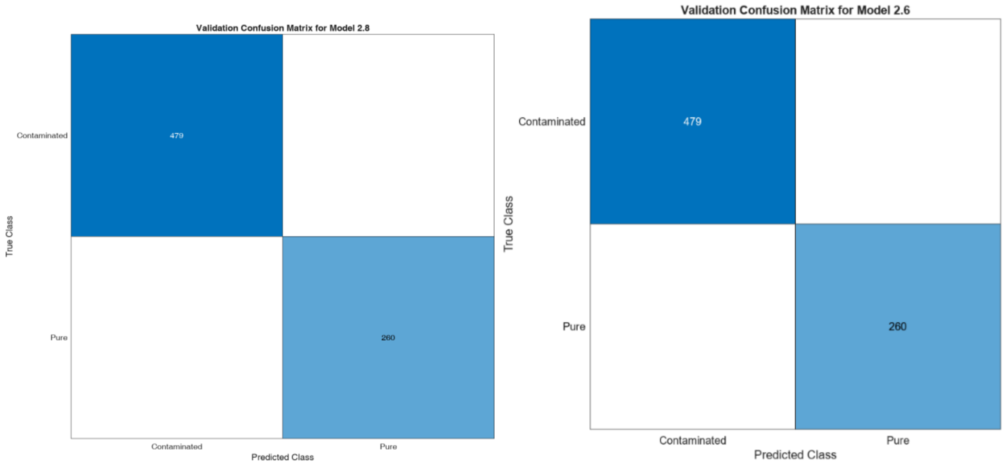

Figure 4.22. Comparison of Confusion Matrix (100% VS 50% Data Set)

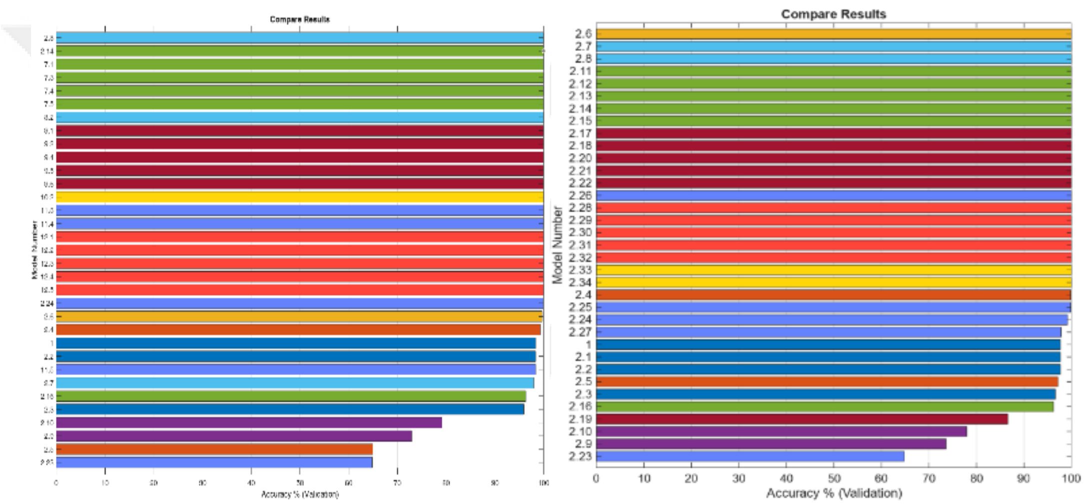

Figure 4.23. Comparison of Accuracy of Models (100% VS 50% Data Set)

By applying the previously applied MLRE modules also, we still have good models that can give us more space for more data optimization.

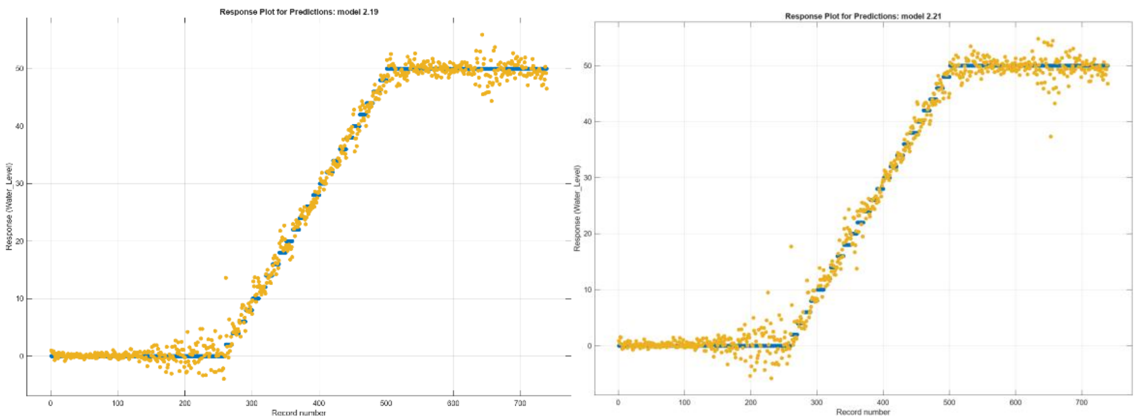

Figure 4.24. Comparison of Response Plot (100% VS 50% Data Set)

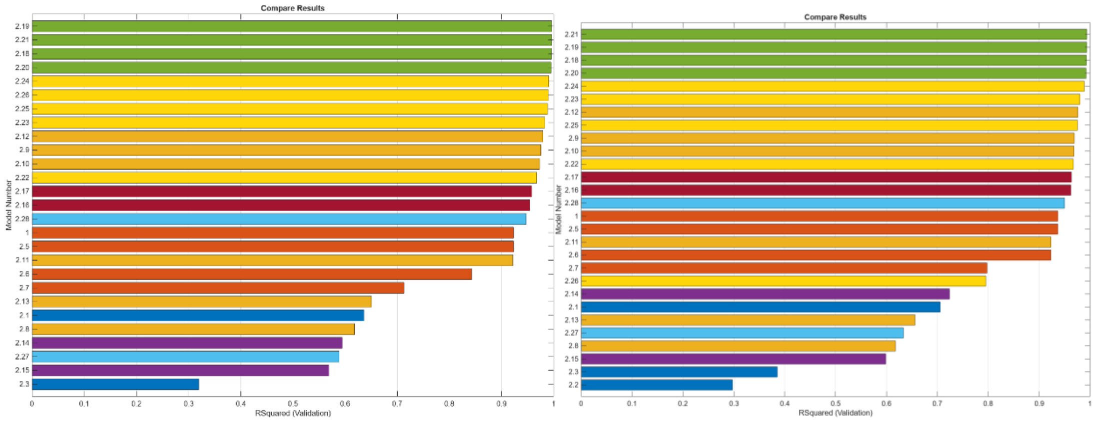

Figure 4.25. Comparison of R-Squared values (100% VS 50% Data Set)

Figure 4.24 and **Figure 4.25** illustrates the difference clearly for MLRT, for all models and a sample model as example.

4.5.6.2 Applying Both Techniques on 25% of the Predictors

As we still have the opportunity for data optimization, we retrained all our previous models on 25% of the data. **Figure 4.26** Illustrates that clearly.

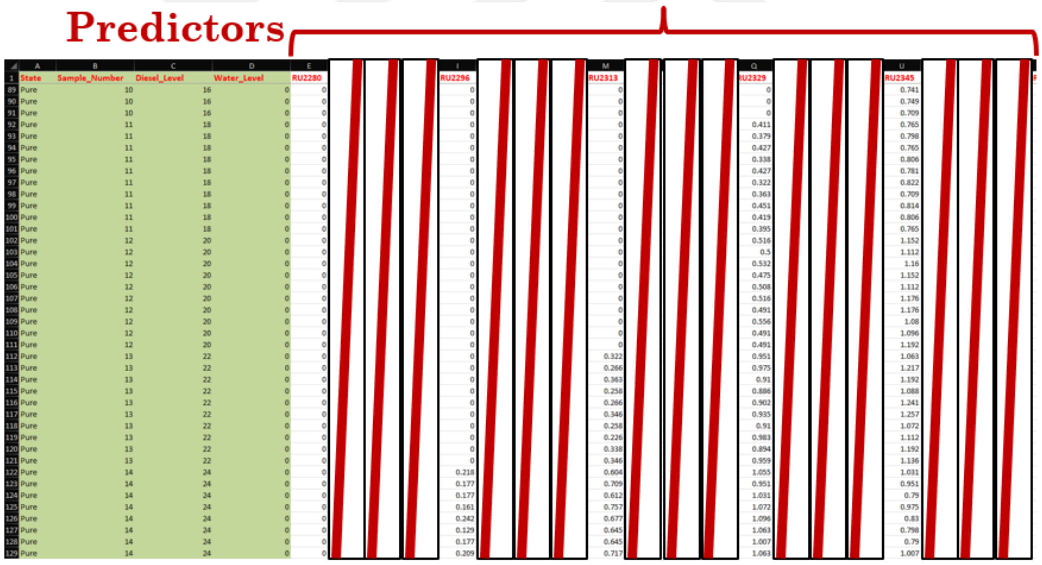

Figure 4.26. Reduction of Predictors to 25% Only

After running the same models, we still achieve 100% accuracy which permit us to apply more data optimization, **Figure 4.25** and **Figure 4.26** Illustrates that clearly. We have the comparison between all models and a comparison between a sample model as an example.

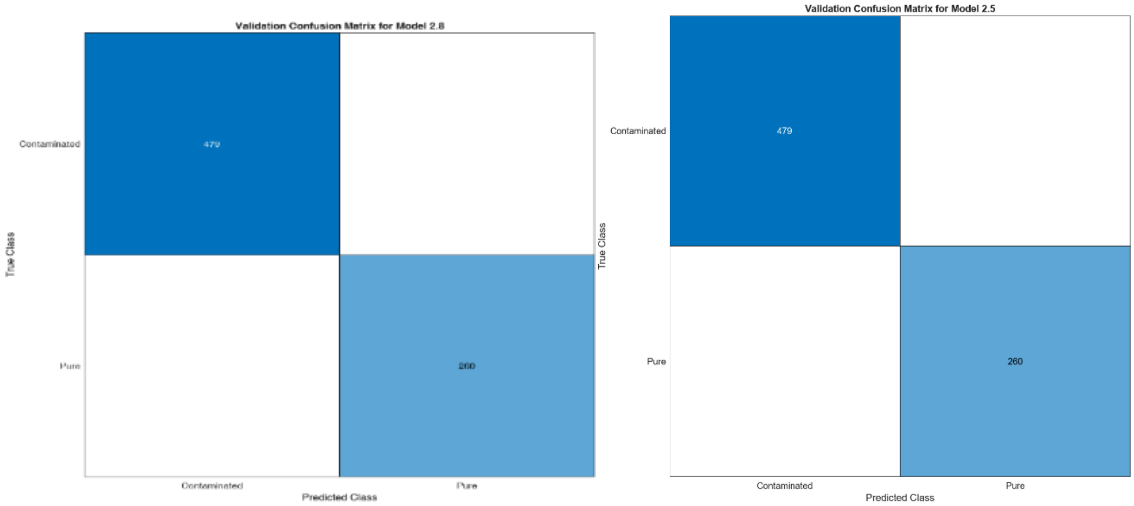

Figure 4.27. Comparison of Confusion Matrix (100% VS 25% Data Set)

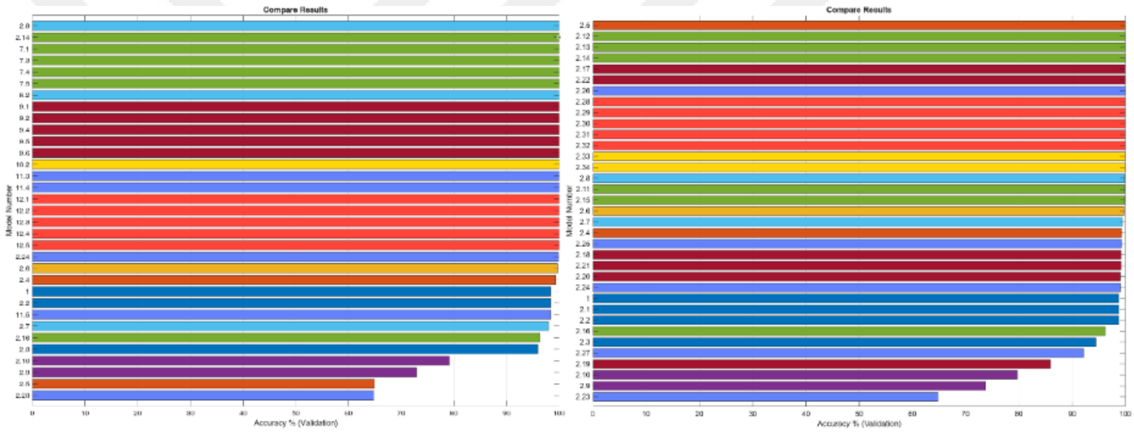

Figure 4.28. Comparison of Accuracy of Models (100% VS 25% Data Set)

4.5.6.3 Applying Both Techniques on 12.5% of the Predictors

As we still have the opportunity for data optimization, we retrained all our previous models on 12.5% of the data. **Figure 4.29** Illustrates that clearly.

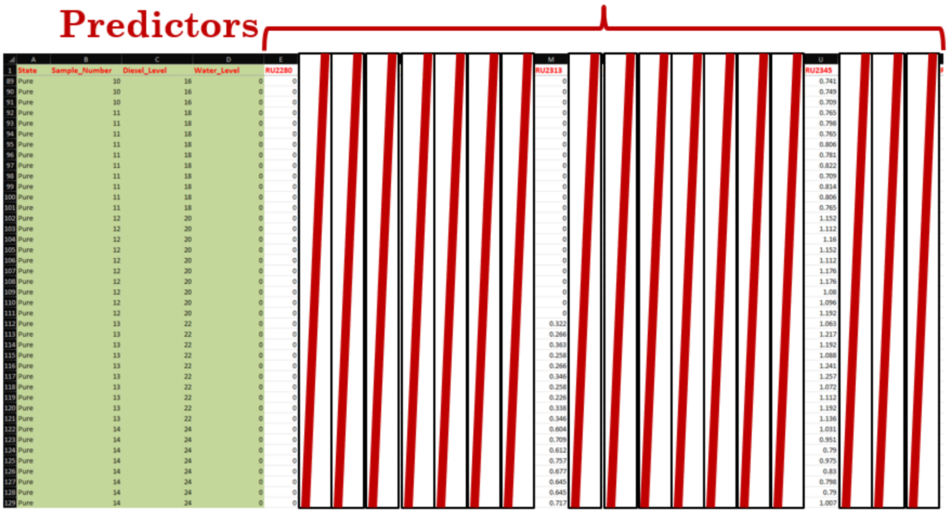

Figure 4.29. Reduction of Predictors to 12.5% Only

After running the same models, we still achieve 100% accuracy which permit us to apply more data optimization, **Figure 4.30** and **Figure 4.31** Illustrates that clearly. We have the comparison between all models and a comparison between a sample model as an example.

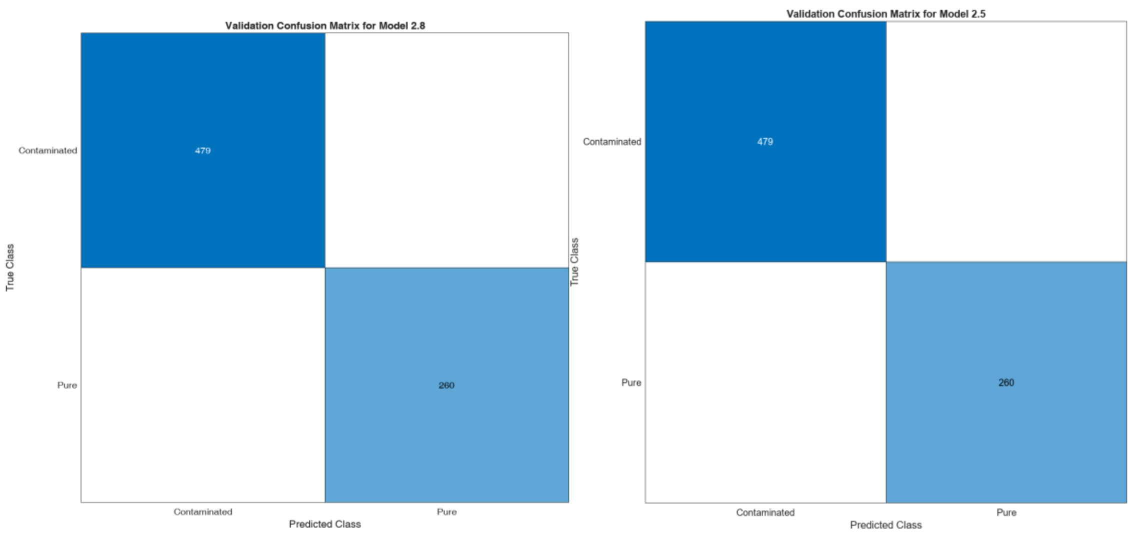

Figure 4.30. Comparison of Confusion Matrix (100% VS 12.5% Data Set)

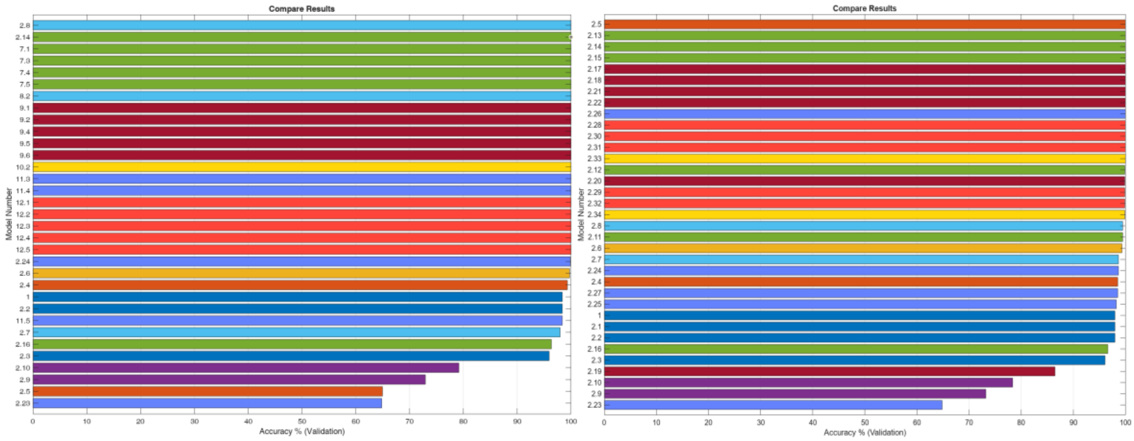

Figure 4.31. Comparison of Accuracy of Models (100% VS 12.5% Data Set)

By applying the previously applied MLRE modules also, we still have good models that can give us more space for more data optimization.

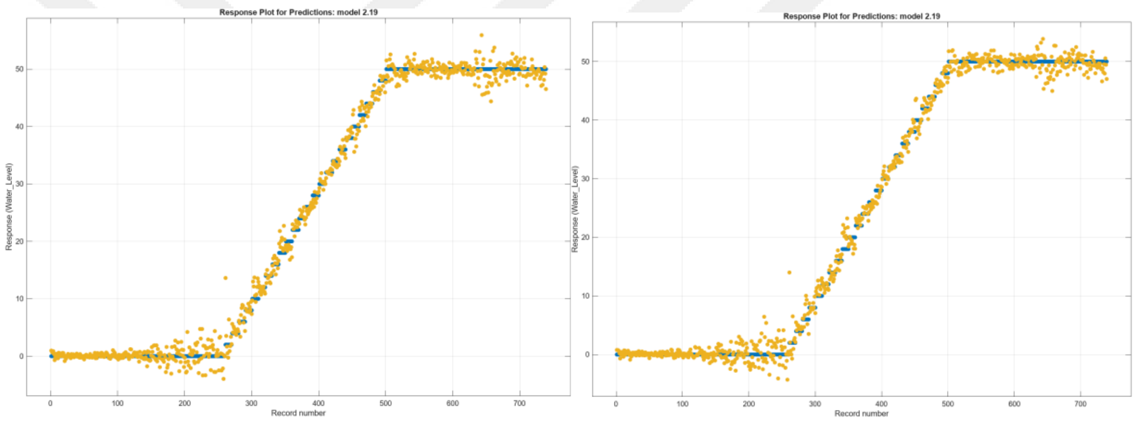

Figure 4.32. Comparison of Response Plot of Models (100% VS 12.5% Data Set)

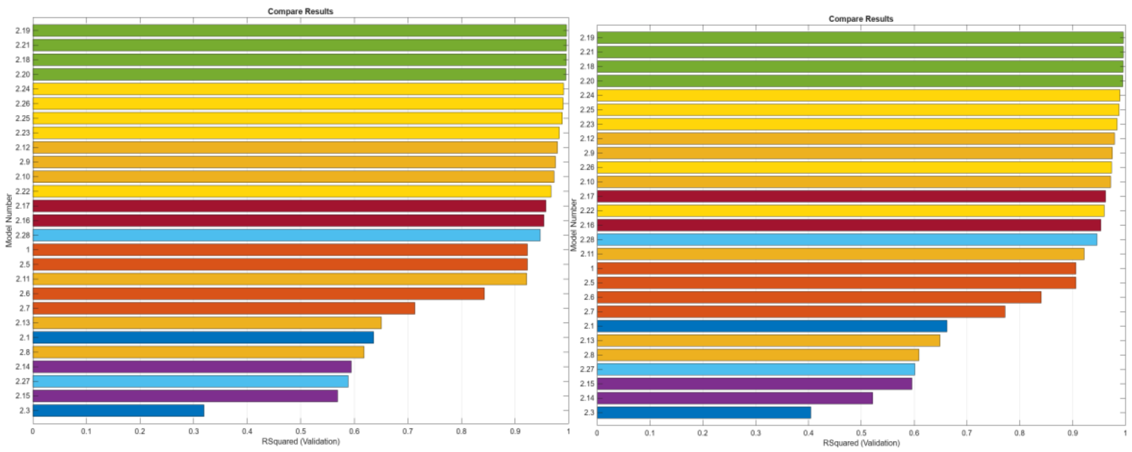

Figure 4.33. Comparison of R-Squared values (100% VS 12.5% Data Set)

Figure 4.32 and **Figure 4.33** illustrates the difference clearly, for all models and a sample model as example.

4.5.6.4 Applying Both Techniques on 6.25% of the Predictors

As we still have the opportunity for data optimization, we retrained all our previous models on 6.25% of the data. **Figure 4.34** Illustrates that clearly.

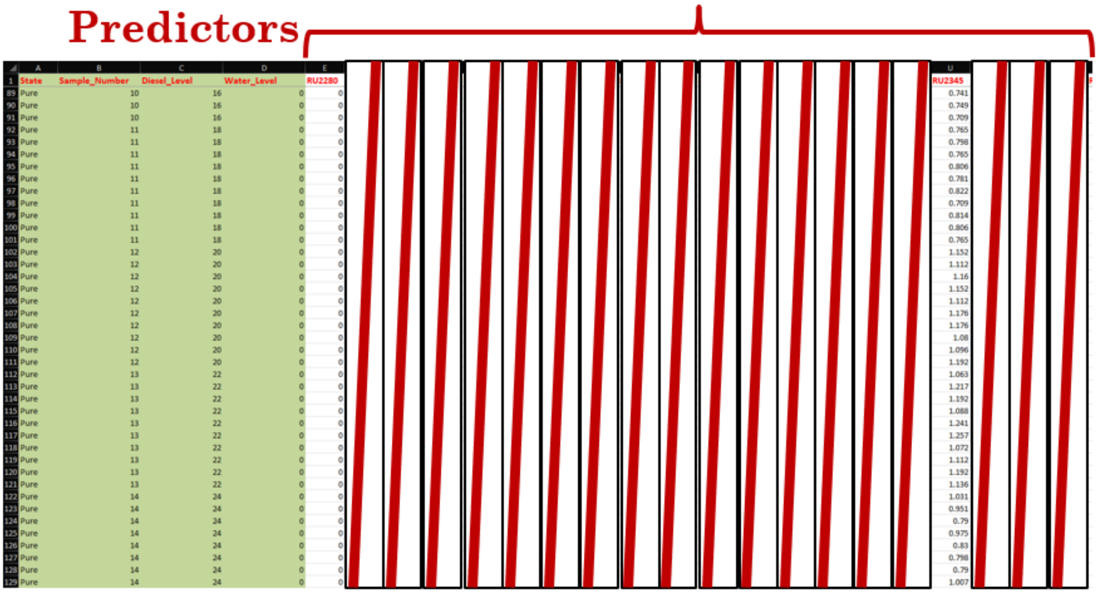

Figure 4.34. Reduction of Predictors to 6.25% Only

After running the same models, we started noticing a drop in accuracy, which means that we are in a marginal data optimization limit, and the optimized amount of data lies between 12.5% and 6.25%,**Figure 4.35** and **Figure 4.36** Illustrates that clearly. We have the comparison between all models and a comparison between a sample model as an example.

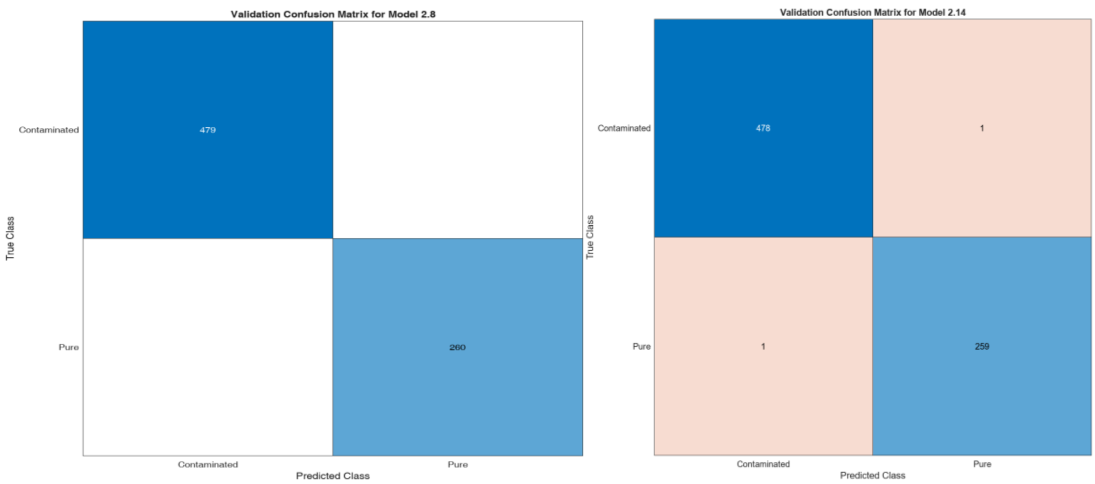

Figure 4.35. Comparison of Confusion Matrix (100% VS 6.25% Data Set)

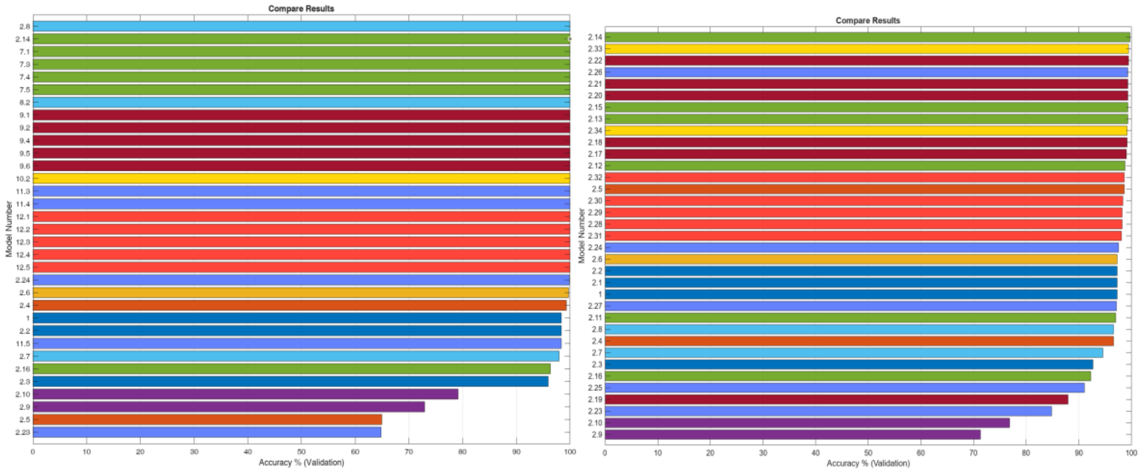

Figure 4.36. Comparison of Accuracy of Models (100% VS 6.25% Data Set)

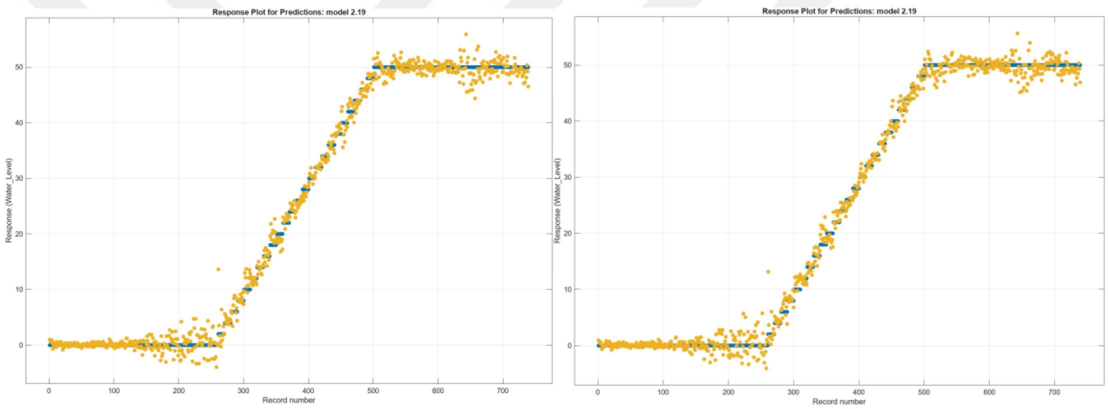

Figure 4.37. Comparison of Response Plot of Models (100% VS 6.25% Data Set)

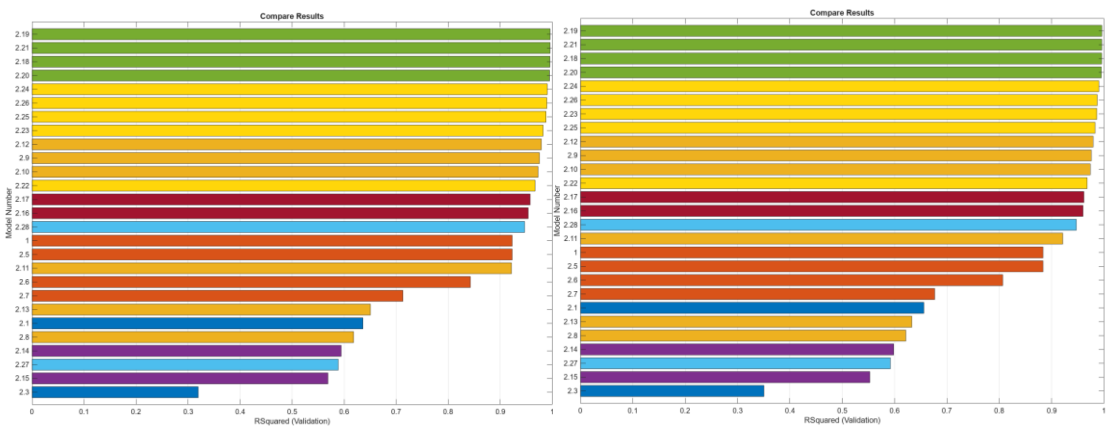

Figure 4.38. Comparison of R-Squared values (100% VS 6.25% Data Set)

Figure 4.37 and **Figure 4.38** illustrates the difference clearly for MLRT, for all models and a sample model as example.

4.5.6.5 Applying Both Techniques on 3.125% of the Predictors

We applied the last data reduction, to run our analysis on ony 3.125% of the data, **Figure 4.39** indicate the rest of the data we used to apply our analysis.

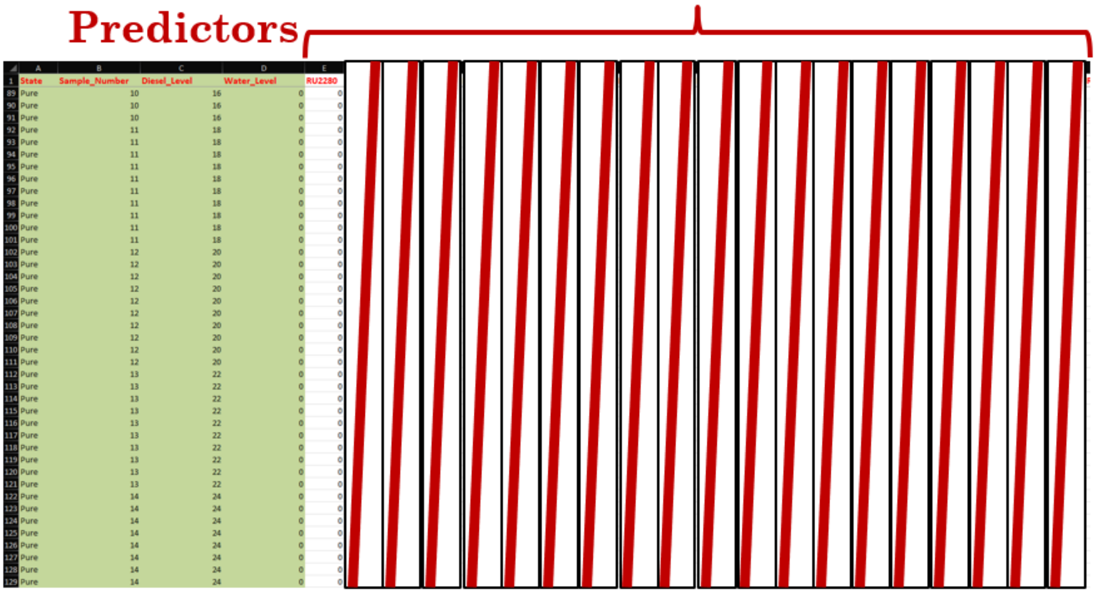

Figure 4.39. Reduction of Predictors to 3.125% Only

After running the same models, we started noticing more drop in accuracy, which means that it is enough to do more data optimization because we are about to sacrifice accuracy to gain immunity against overfitting, and the optimized amount of data still lies between 12.5% and 6.25%,**Figure 4.40** and **Figure 4.41** Illustrates that clearly. We have the comparison between all models and a comparison between a sample model as an example.

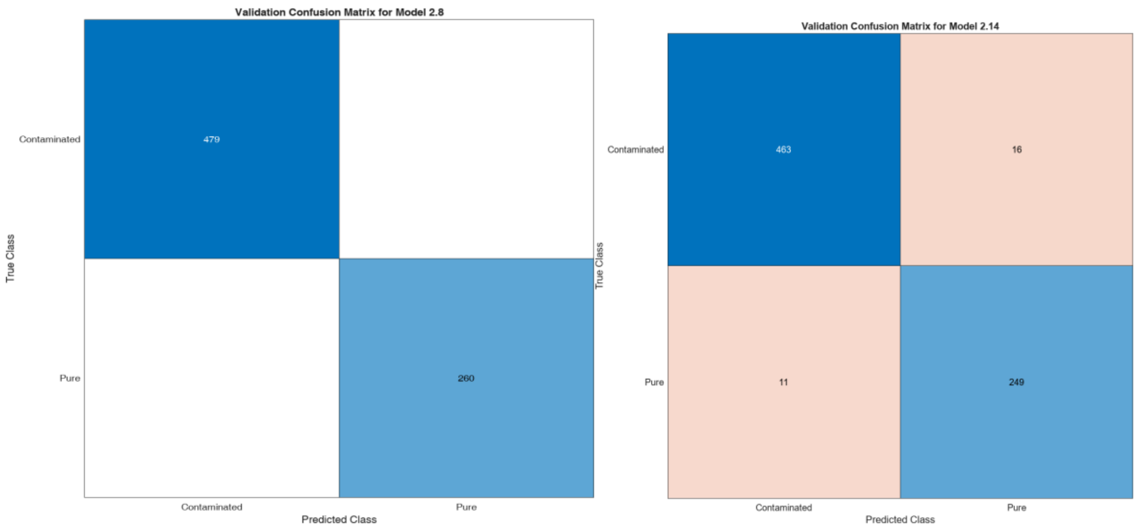

Figure 4.40. Comparison of Confusion Matrix (100% VS 3.125% Data Set)

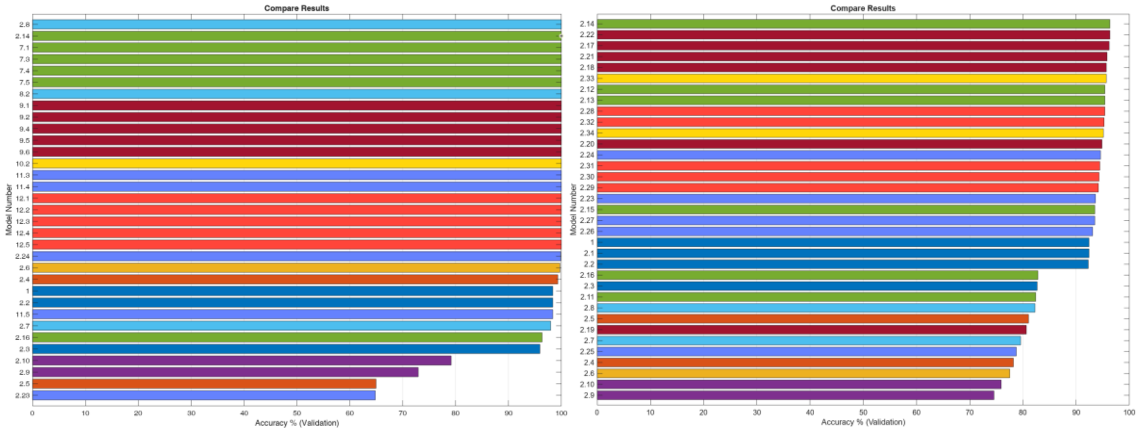

Figure 4.41. Comparison of Accuracy of Models (100% VS 3.125% Data Set)

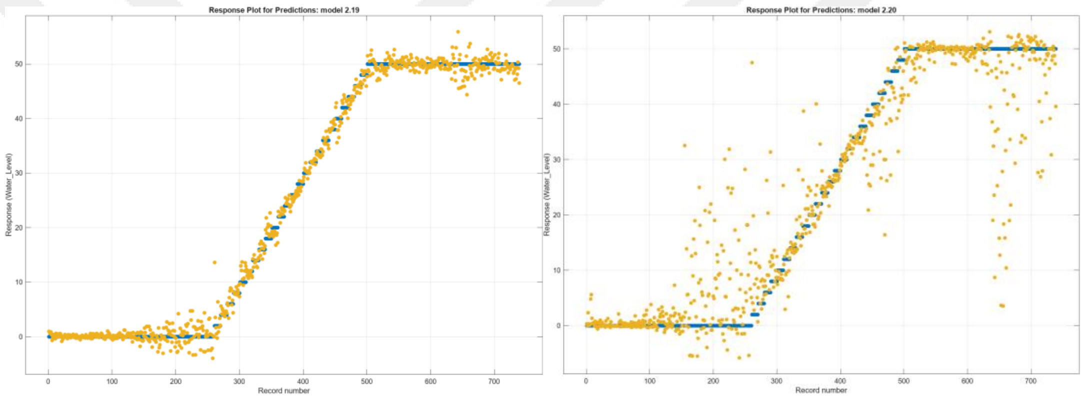

Figure 4.42. Comparison of Response Plot of Models (100% VS 3.125% Data Set)

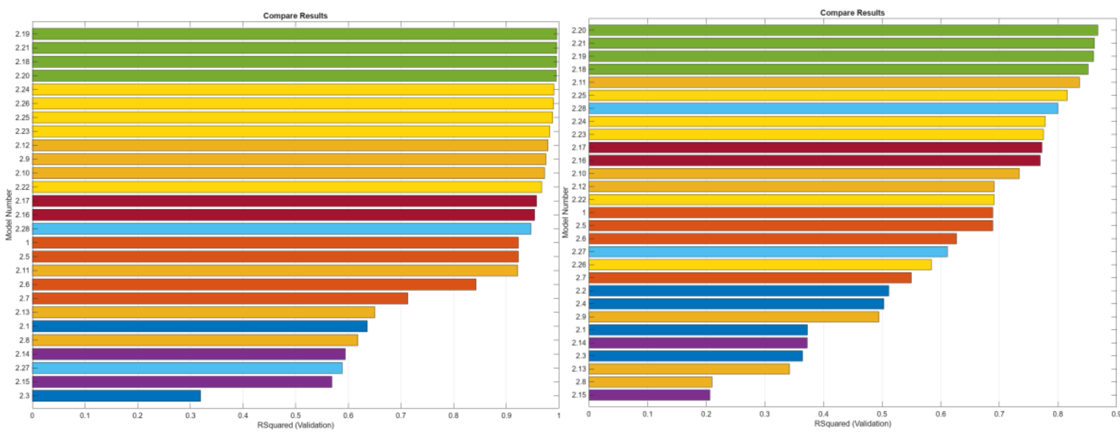

Figure 4.43. Comparison of R-Squared values (100% VS 3.125% Data Set)

Figure 4.42 and **Figure 4.43** illustrates the difference clearly for MLRT, for all models and a sample model as example.

4.5.7 Data Manipulation (Substitution) Before Applying Both Techniques (MLCT & Regression)

In order to continue assessment of the optimization techniques, we decided here to manipulate data by replacing all non-Zero values, and keeping all zero values as it is, we are aiming to assess the data identity and checking the effect of absence of the relative value between data predictors

4.5.7.1 Applying Both Techniques After Replacing values with 0s&1s

As shown in **Figure 4.44**, all non-Zero valves has been replaced by ones to remove the relative difference between data and distinguish it from zero values As clearly shown in **Figure 4.45**, **Figure 4.46**, **Figure 4.47** and **Figure 4.48**, we started having fast drop in accuracy for the first trial, which reflects the importance of data identity and the relative value between data points "data pattern". We did our analysis using both classifier technique and Regression technique.

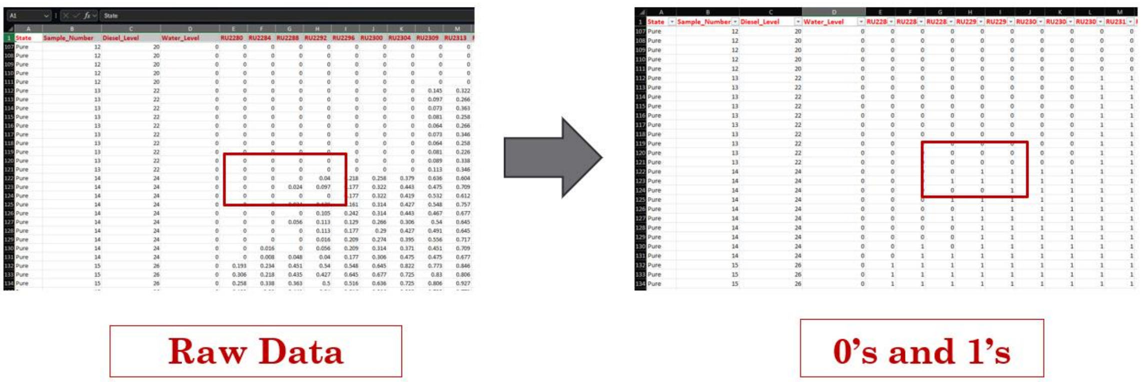

Figure 4.44. Replacing non-zero values by 1 to manipulate the data

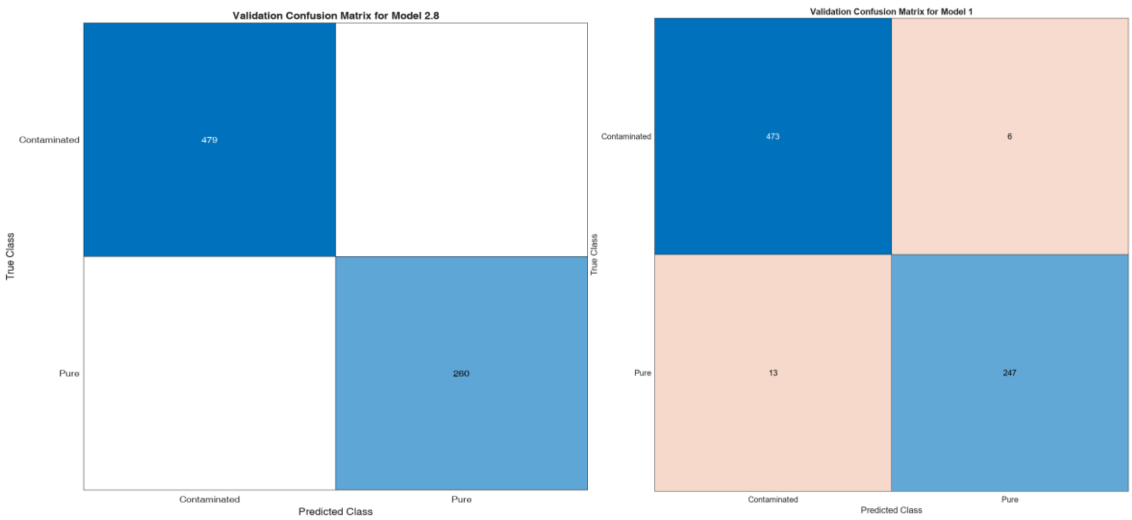

Figure 4.45. Comparison of Confusion Matrix (Real VS Manipulated Data 0 & 1s)

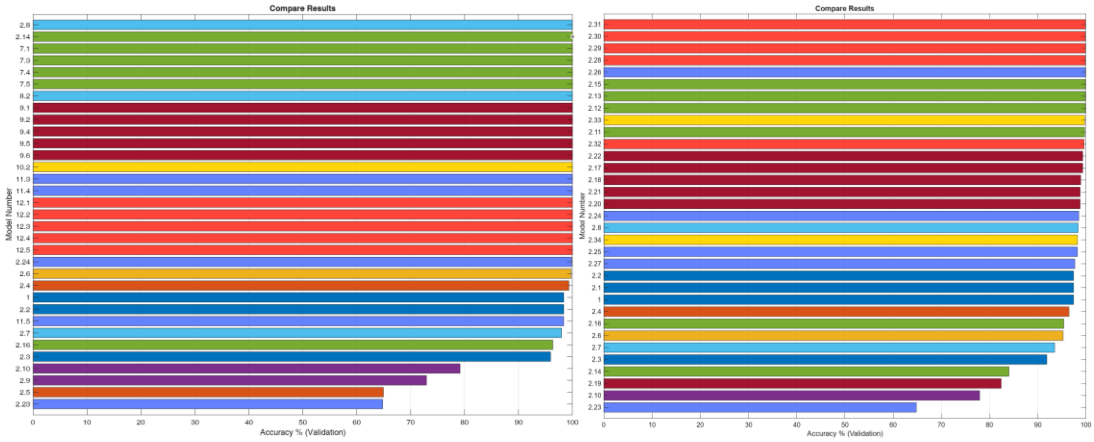

Figure 4.46. Comparison of Accuracy of Models (Real VS Manipulated Data 0 & 1s)

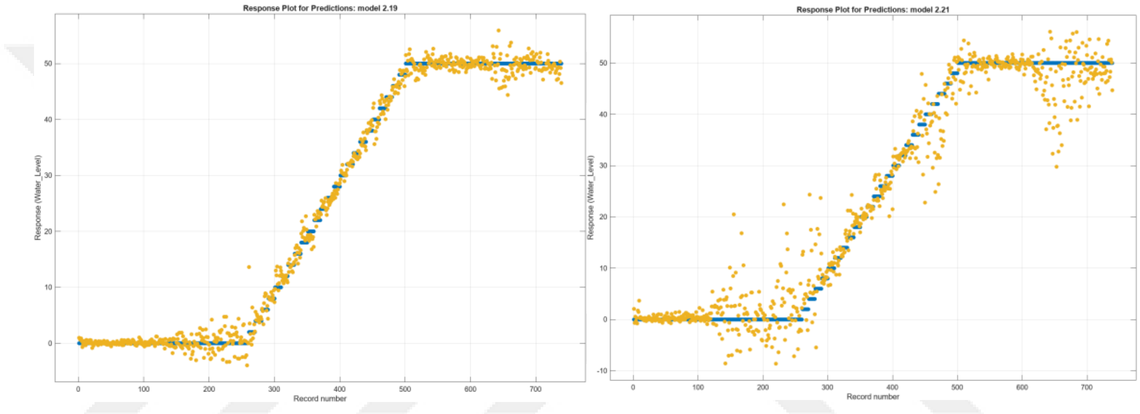

Figure 4.47. Comparison of Response Plot of Models (Real VS Manipulated Data 0 & 1s)

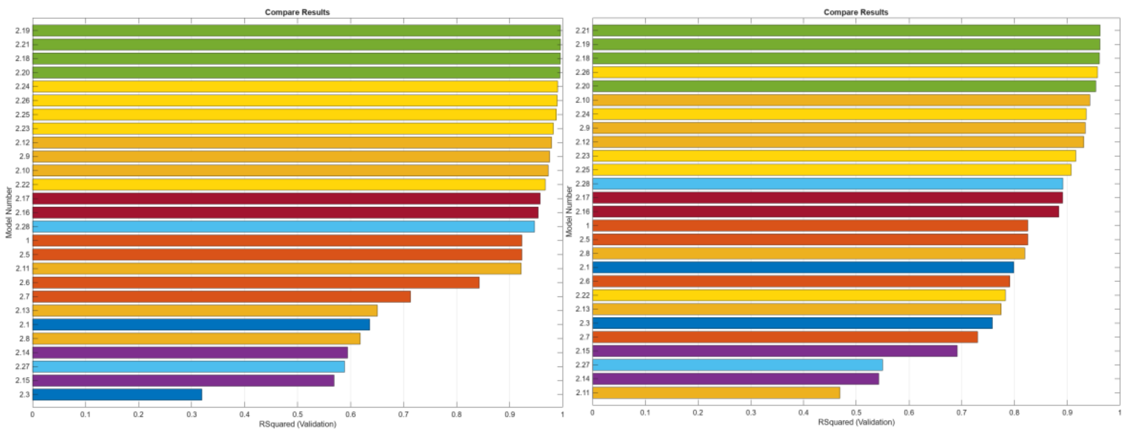

Figure 4.48. Comparison of R-Squared values (Real VS Manipulated Data 0 & 1s)

4.5.7.2 Applying Both Techniques After Replacing values with -1s&1s

Using the same methodology, but instead of keeping the zero values as zero, we decided to replace them by -1 which means that we will have 1s instead of all non-zero values, and will have -1s instead of all zero values , **Figure 4.49** clearly shows that transformation.

As clearly shown in **Figure 4.50**, **Figure 4.51**, **Figure 4.52** and **Figure 4.53**, we have difference in accuracy than that of the (0s & 1s) analysis, which indicates that the model consider 0s and -1s in slight different way.

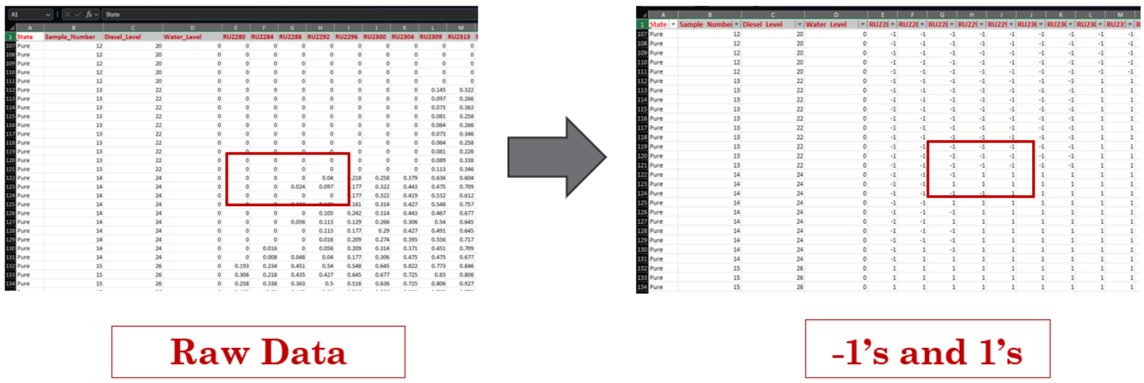

Figure 4.49. Replacing non-zero values by 1, and zeros with -1

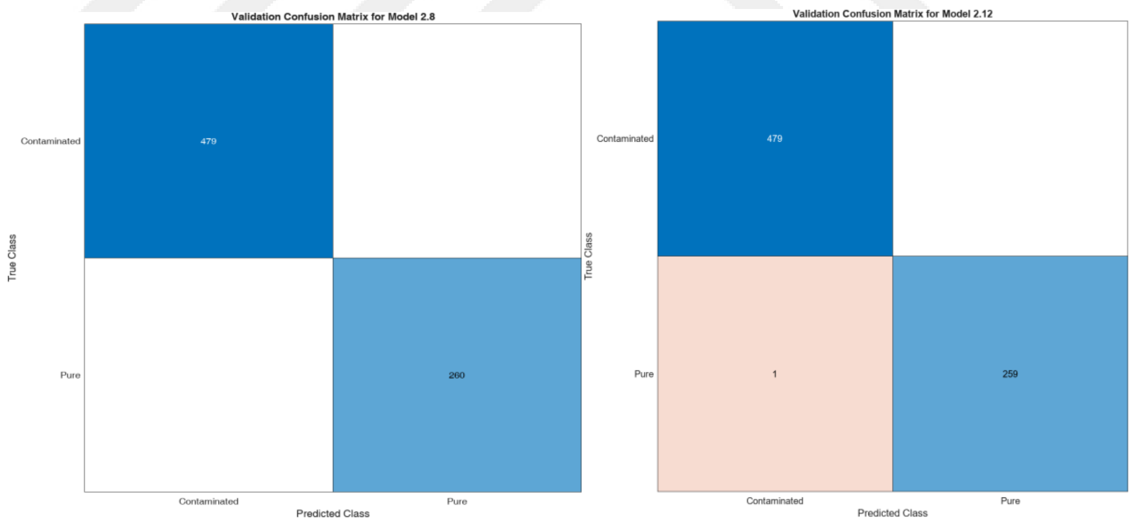

Figure 4.50. Comparison of Confusion Matrix (Real VS Manipulated Data -1 & 1s)

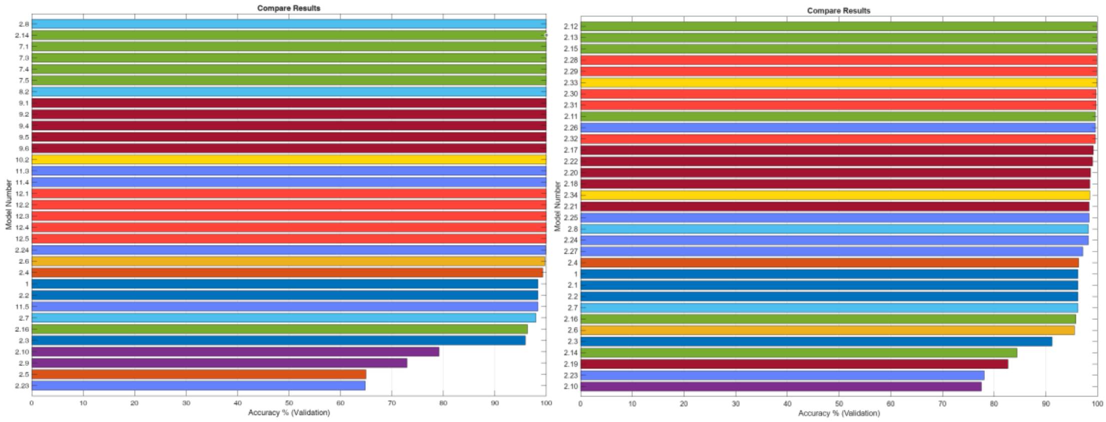

Figure 4.51. Accuracy Comparison of Models (Real VS Manipulated Data -1 & 1s)

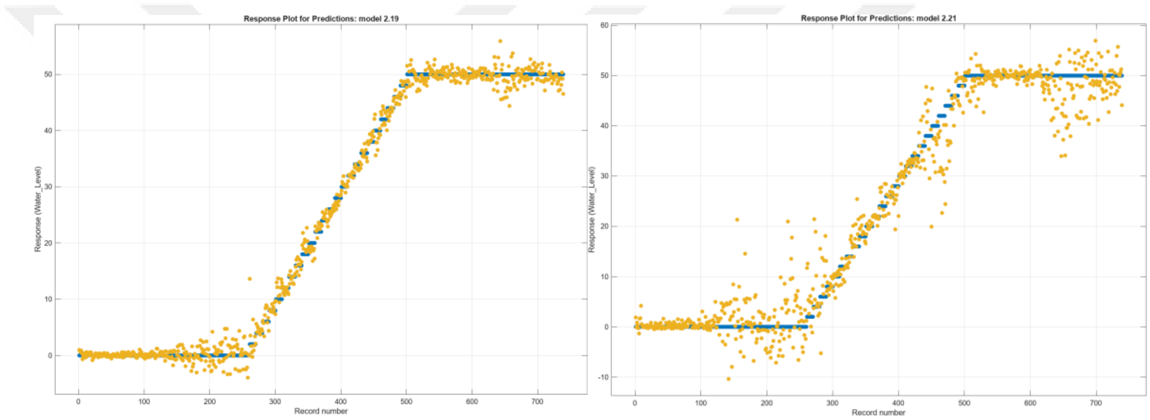

Figure 4.52. Comparison of Response Plot of Models (Real VS Manipulated Data -1 & 1s)

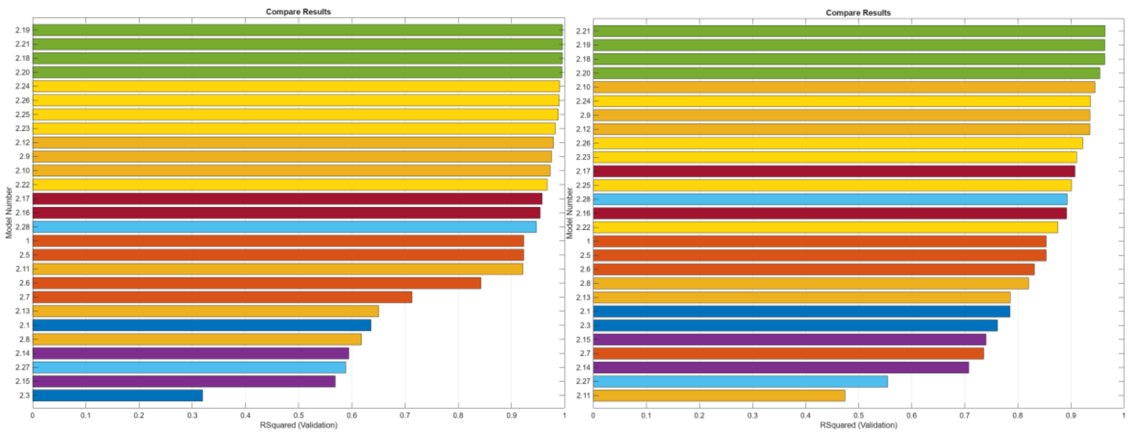

Figure 4.53. Comparison of R-Squared values (Real VS Manipulated Data -1 & 1s)

4.5.7.3 Applying Both Techniques After Summation of Rows

To continue processing data, we decided to rely on one predictor only. We made this by summing all rows values together , forming one total value representing the full row, then applying all Machine Learning classifications and Regression techniques. **Figure 4.54** illustrates that below.

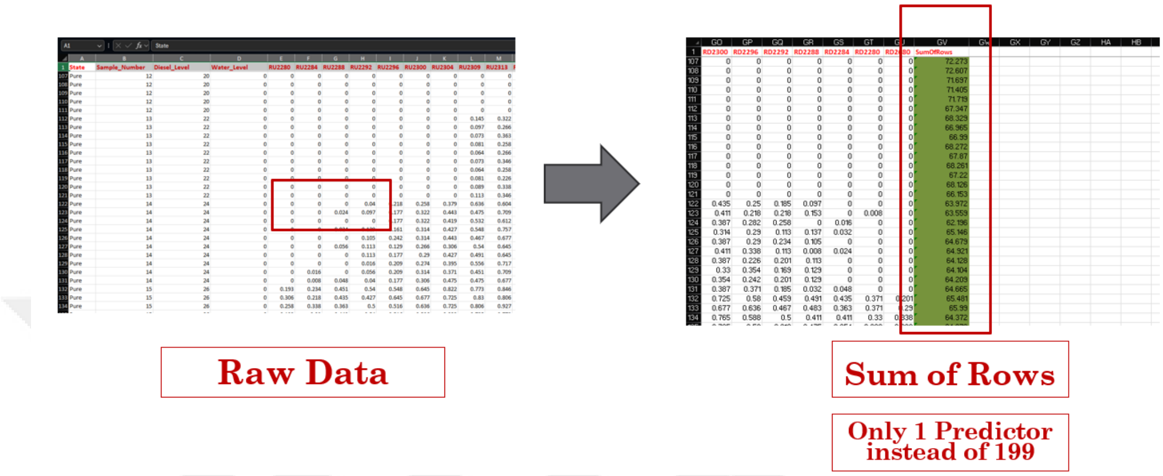

Figure 4.54. Summation of Rows to create 1 Predictor

As clearly shown in **Figure 4.50**, **Figure 4.51**, **Figure 4.52** and **Figure 4.53**, we have difference in accuracy than that of the (0s & 1s) analysis, which indicates that the model consider 0s and -1s in slight different way.

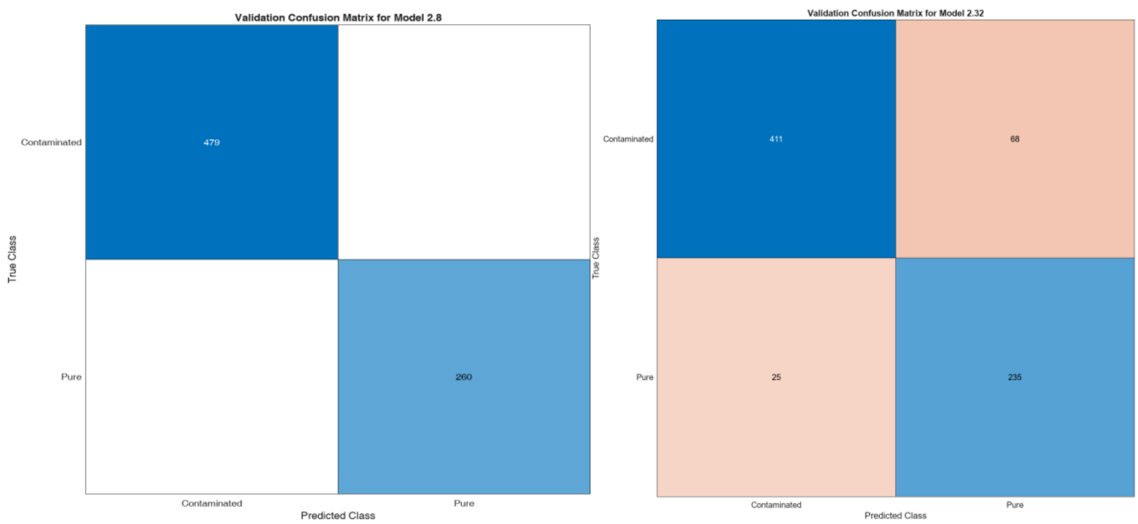

Figure 4.55. Comparison of Confusion Matrix (Real Data VS 1 Sum Predictor)

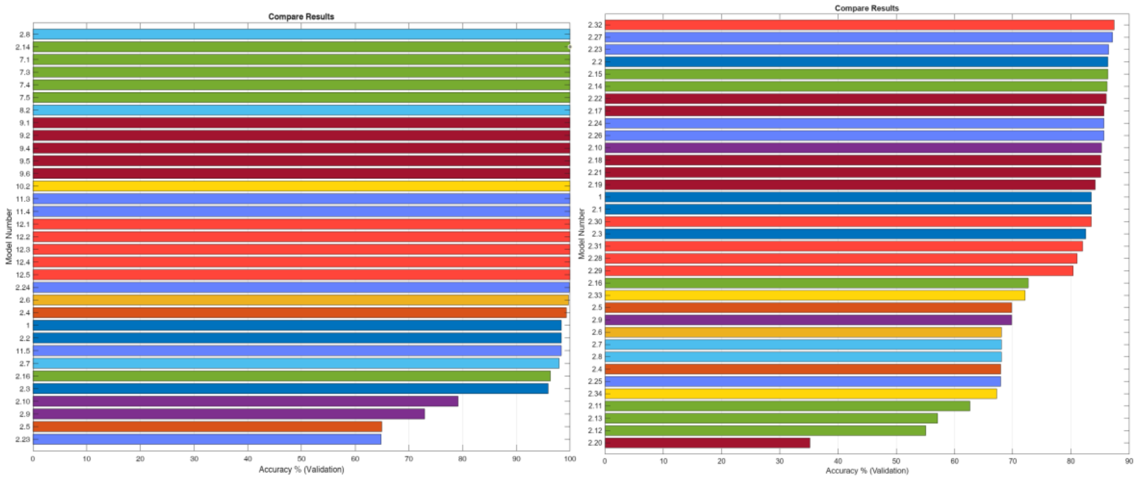

Figure 4.56. Comparison of Accuracy of Models (Real Data VS 1 Sum Predictor)

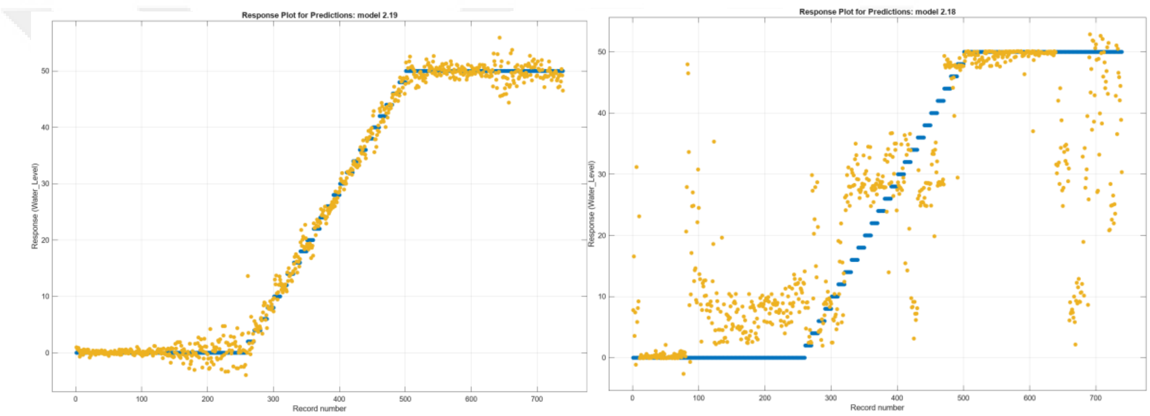

Figure 4.57. Comparison of Response Plot of Models (Real Data VS 1 Sum Predictor)

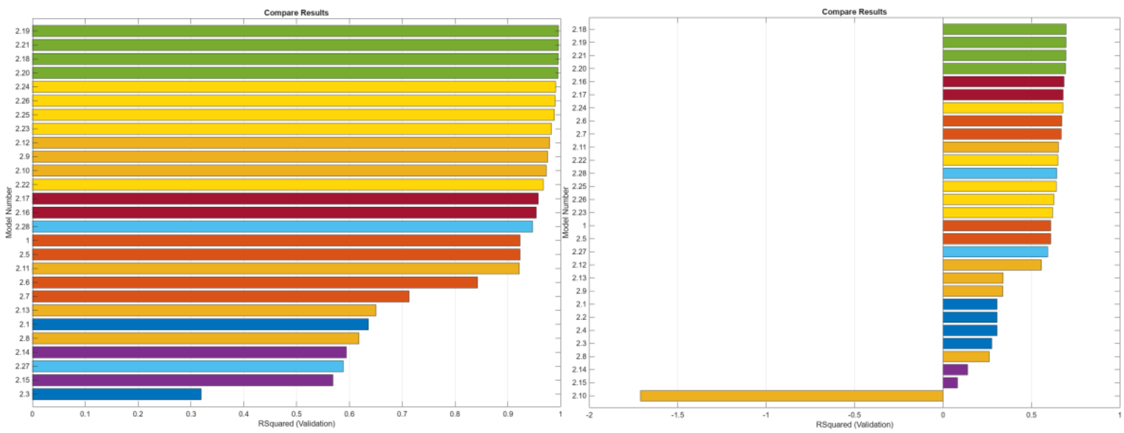

Figure 4.58. Comparison of R-Squared values (Real Data VS 1 Sum Predictor)

4.5.7.4 Applying Both Techniques After Replacing values with 0s&1s and Summing Rows

Blending two Data processing activities, we decided in This analysis to mix between replacement of values by 0s & 1s and summing rows, **Figure 4.59** clearly shows the two processes to be carried out.

As clearly shown in **Figure 4.60**, **Figure 4.61**, **Figure 4.62** and **Figure 4.63**, we have drop in accuracy for the first trial, which reflects the importance of data identity and the relative value between data points "data pattern". We did our analysis using both classifier technique and Regression technique.

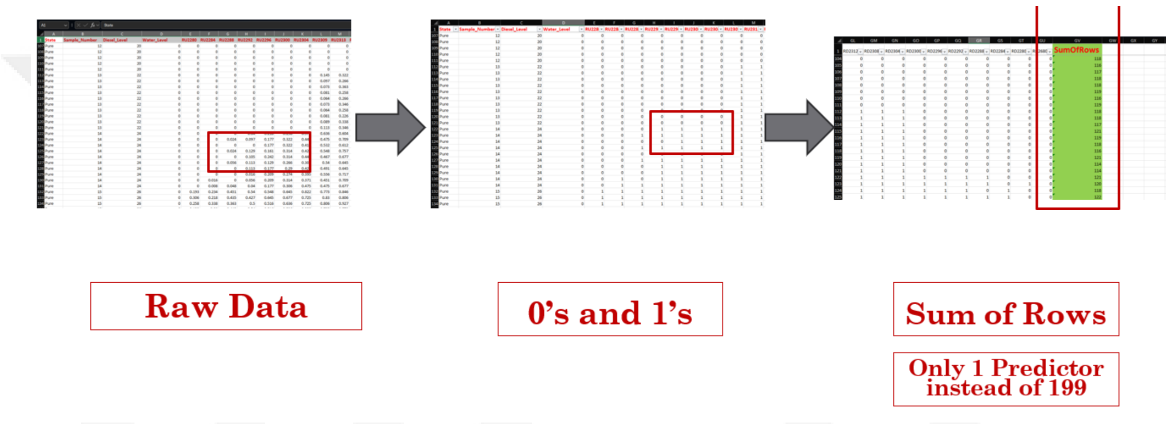

Figure 4.59. Replacing non-zero values by 1 then applying summation

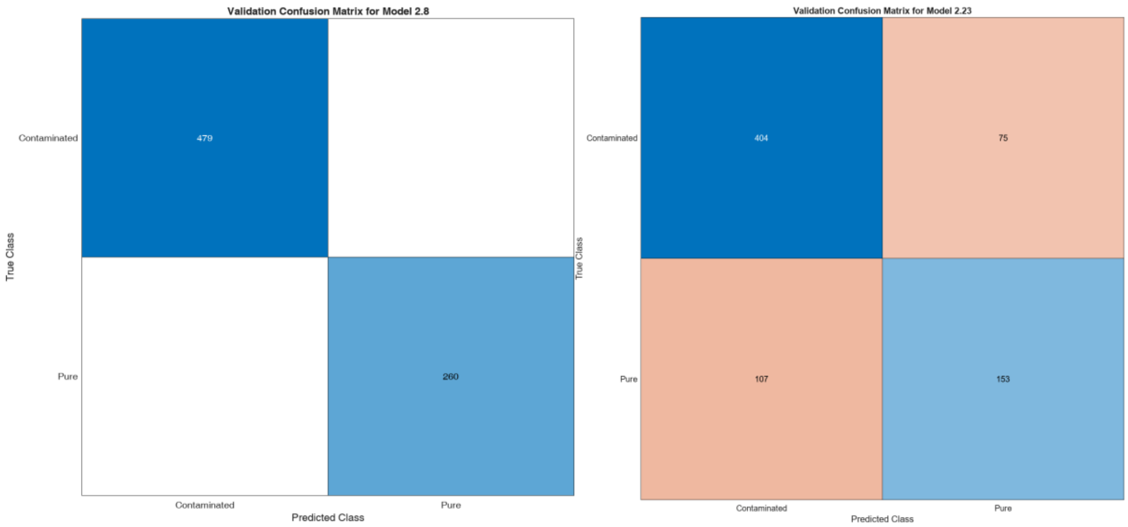

Figure 4.60. Comparison of Response Plot of Models (Real VS Manipulated Data 0 & 1s and summed)

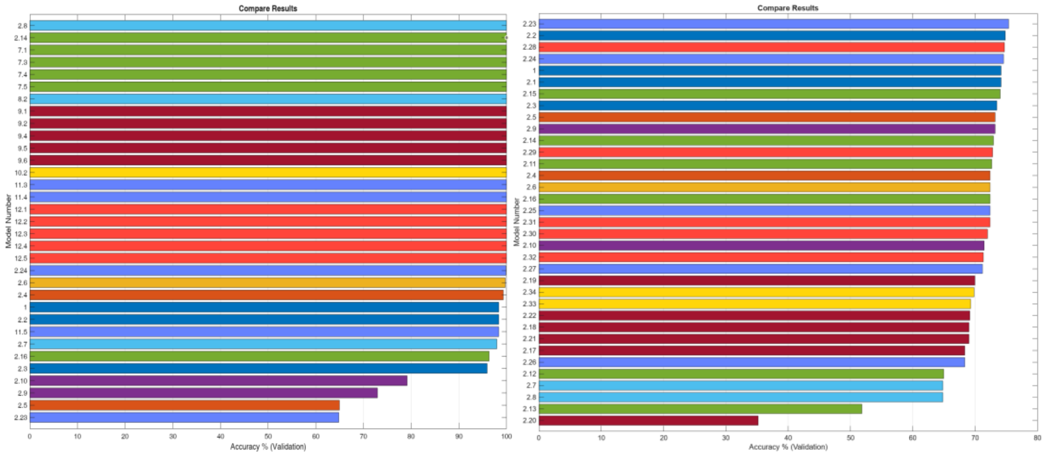

Figure 4.61. Comparison of Accuracy of Models (Real VS Manipulated Data 0s & 1s and summed)

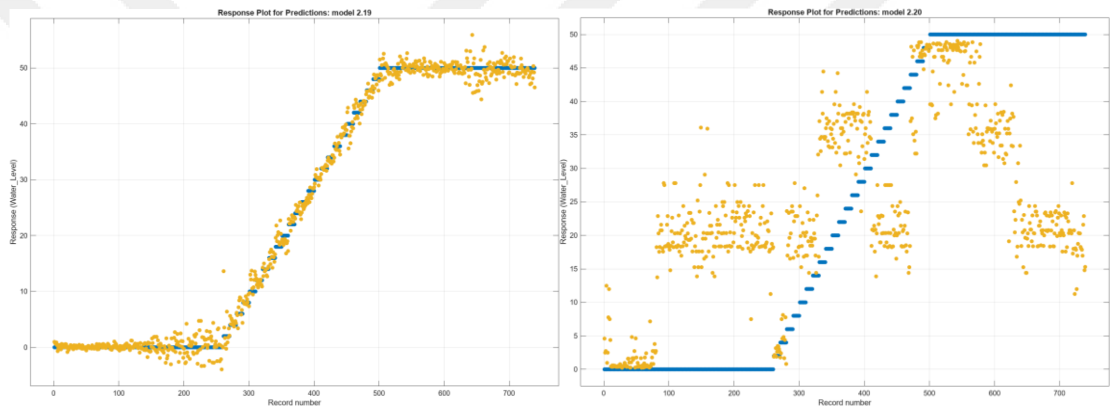

Figure 4.62. Comparison of Response Plot of Models (Real VS Manipulated Data 0s & 1s and summed)

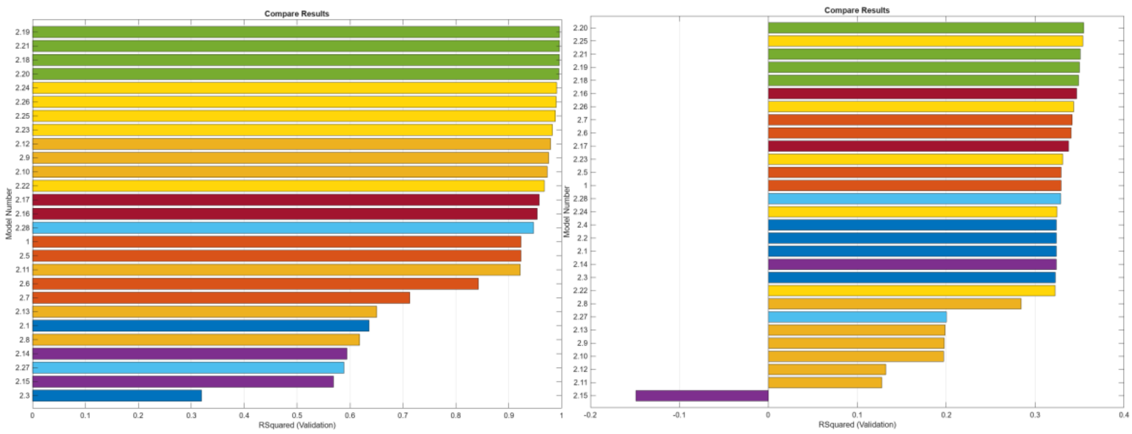

Figure 4.63. Comparison of R-Squared values (Real VS Manipulated Data 0s & 1s and summed)

4.5.7.5 Applying Both Techniques After Replacing values with -1s&1s and Summing Rows

Blending two Data processing activities, we decided in This analysis to mix between replacement of values by 0s & 1s and summing rows, **Figure 4.64** clearly shows the two processes to be carried out.

As clearly shown in **Figure 4.65**, **Figure 4.66**, **Figure 4.67** and **Figure 4.68**, we have drop in accuracy for the first trial, which reflects the importance of data identity and the relative value between data points "data pattern". We did our analysis using both classifier technique and Regression technique.

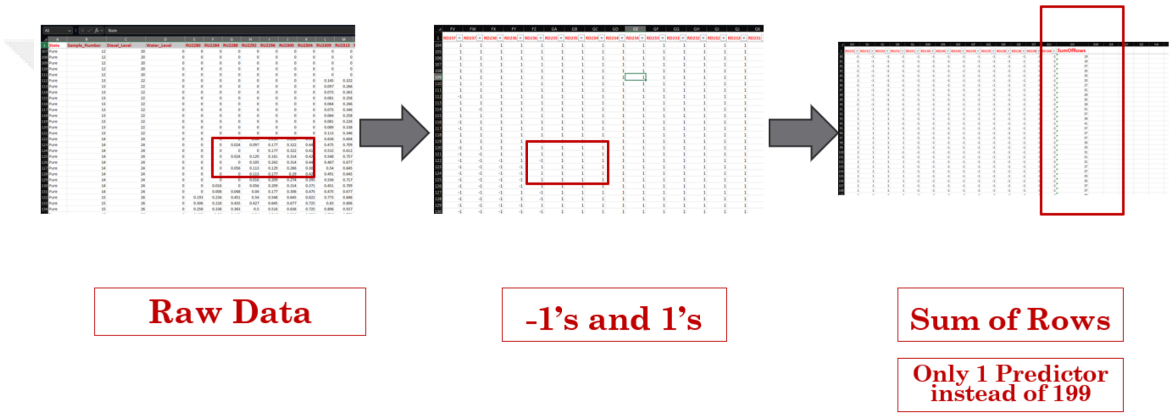

Figure 4.64. Replacing non-zero values by 1 and 0 with -1 then summation

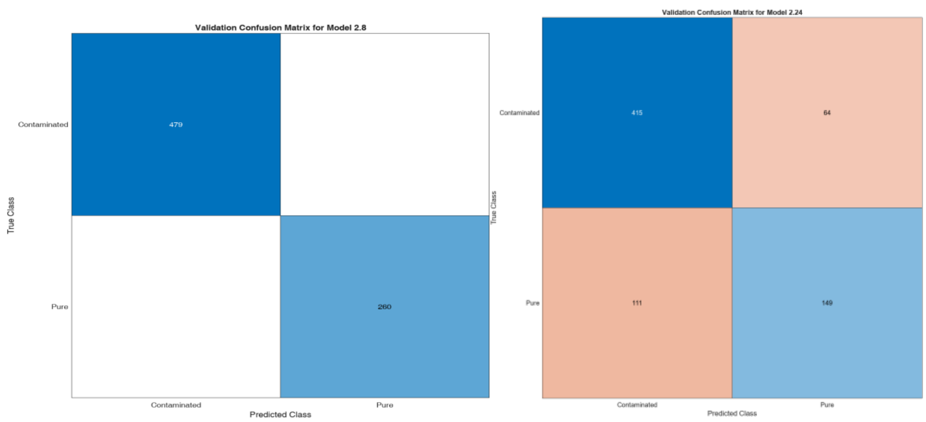

Figure 4.65. Comparison of Response Plot of Models (Real VS Manipulated Data -1 & 1s and summed)

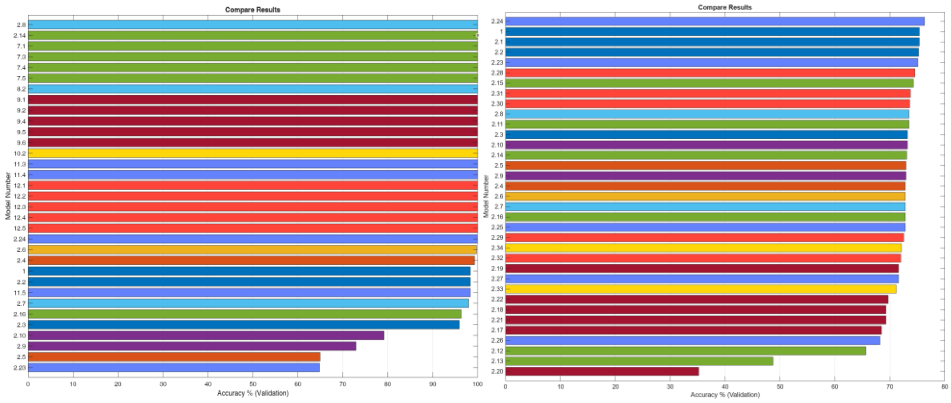

Figure 4.66. Comparison of Accuracy of Models (Real VS Manipulated Data -1s & 1s and summed)

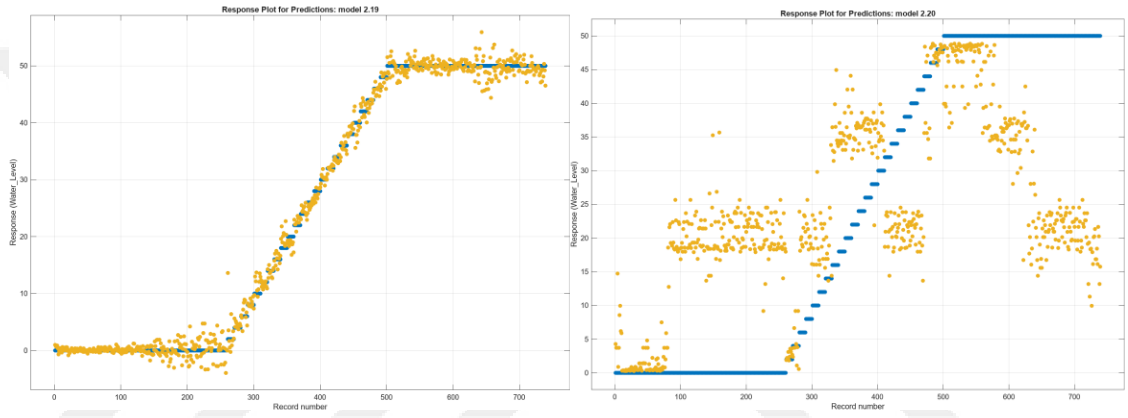

Figure 4.67. Comparison of Response Plot of Models (Real VS Manipulated Data -1s & 1s and summed)

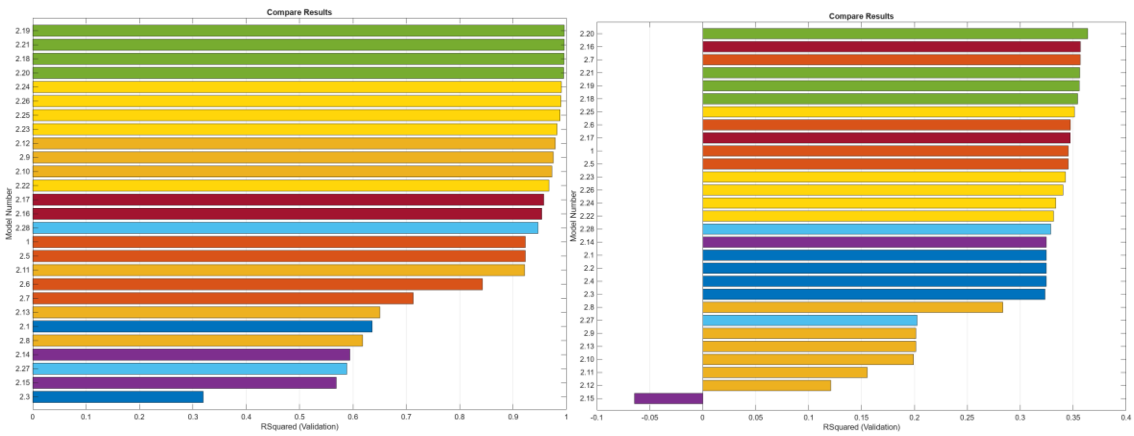

Figure 4.68. Comparison of R-Squared values (Real VS Manipulated Data -1s & 1s and summed)

4.6 Feature Selection Application on Data

As we found a good opportunity to optimize the data, we manually eliminated a big portion of the data and still get good accuracy, so we applied some of the common "Feature Selection" techniques to check how these common techniques see the optimization opportunities in our data. The following algorithms are demonstrated.

1. MRMR (Minimum Redundancy Maximum Relevance): Selects features that are highly relevant to the target variable while minimizing redundancy among themselves. Calculates mutual information between each feature and the target (relevance). Penalizes features that are highly correlated with already selected features (redundancy). Ensures that selected features provide unique, non-overlapping information, improving model efficiency and reducing overfitting.

2. Chi-Square (Chi²): Evaluates the dependency between categorical features and the target variable. Compares observed and expected frequencies of feature-target combinations. Higher Chi² scores indicate stronger association with the target. Commonly used in classification problems to rank categorical predictors by their predictive power.

3. ReliefF: Estimates feature importance by considering how well features differentiate between similar instances of different classes. For each sample, finds nearest neighbors from the same class and different classes. Features that consistently separate classes receive higher weights. Handles noisy and multi-class datasets well, making it suitable for real-world sensor data.

4. ANOVA (Analysis of Variance): Measures the statistical significance of differences in feature means across target classes. Computes F-statistic by comparing variance between groups (classes) to variance within groups. Higher F-values indicate that the feature discriminates well between classes. Ideal for continuous features in classification tasks.

5. Kruskal-Wallis Test: A non-parametric alternative to ANOVA for ranking features when data does not meet normality assumptions. Ranks all data points and compares rank sums across groups. Determines whether distributions differ significantly between classes. Robust for non-normal or ordinal data, making it suitable for radar measurements with irregular distributions.

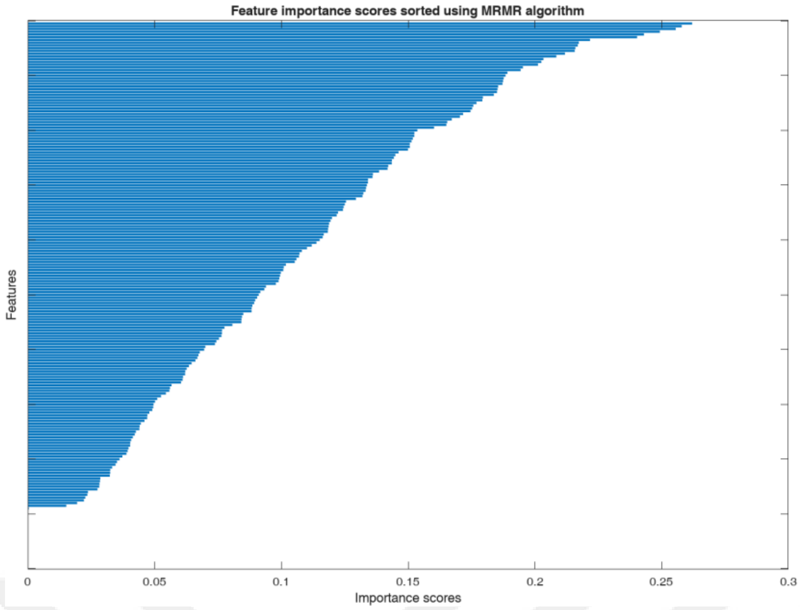

Figure 4.69. Feature Importance Scores using MRMR Algorithm

Figure 4.69 illustrates how the MRMR algorithm ranks the predictors (features) based on their relevance to the target variable (e.g., contamination state or liquid level) while minimizing redundancy among features.

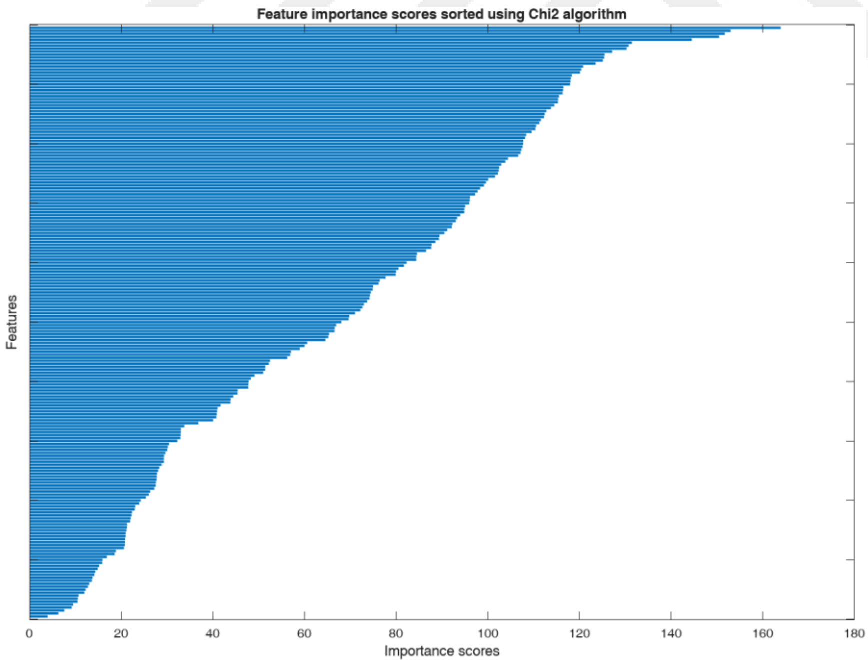

Figure 4.70. Feature Importance Scores using Chi2 Algorithm

Figure 4.70 illustrates the Feature Importance Scores using the Chi-Square (Chi^2) algorithm. This figure is part of the feature selection analysis aimed at identifying which predictors (features) in our radar measurement dataset have the strongest statistical association with the target variable (e.g., contamination state or liquid level).

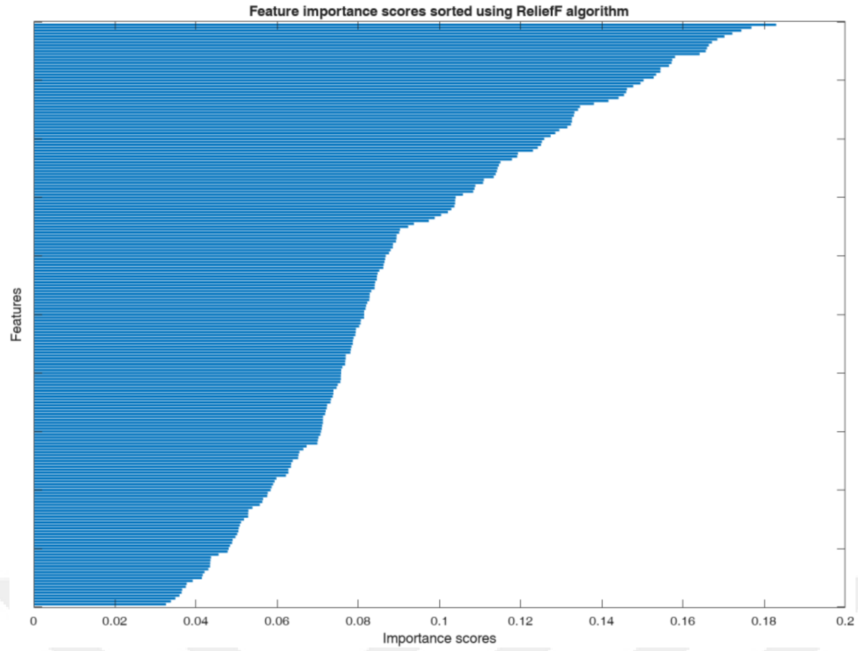

Figure 4.71. Feature Importance Scores using ReliefF Algorithm

Figure 4.71 illustrates the Feature Importance Scores using the ReliefF algorithm, which is part of the feature selection analysis applied to optimize machine learning models for contamination detection and level estimation.

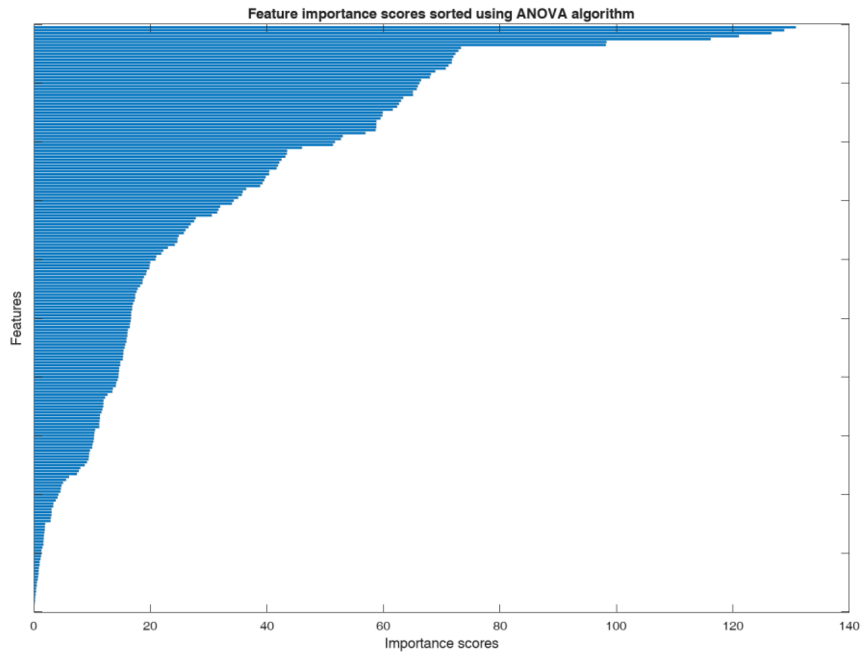

Figure 4.72. Feature Importance Scores using ANOVA Algorithm

Figure 4.72 illustrates the Feature Importance Scores using the ANOVA (Analysis of Variance) algorithm, which is part of the feature selection process applied to optimize machine learning models for contamination detection and liquid level estimation.

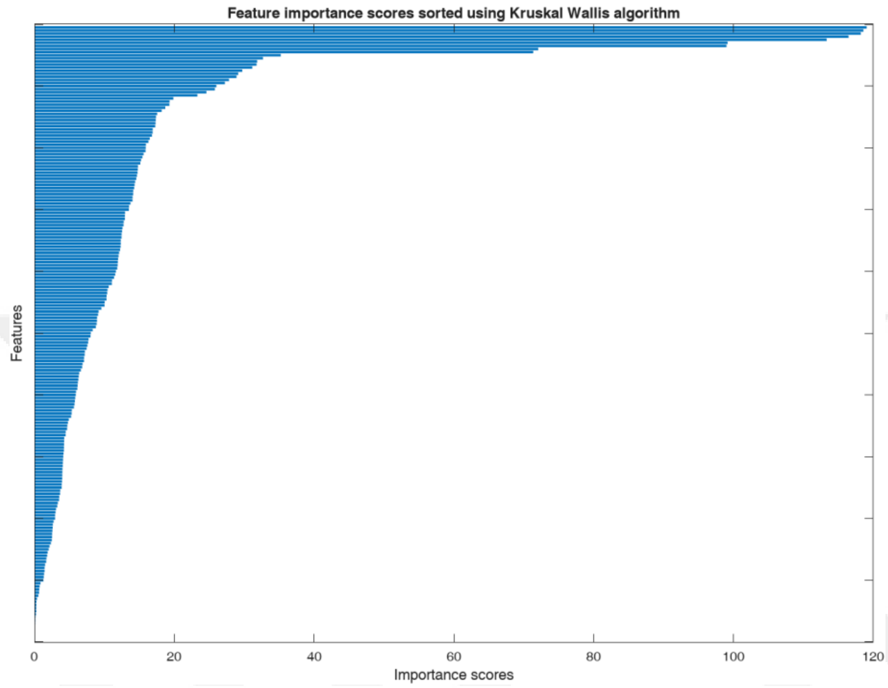

Figure 4.73. Feature Importance Scores using Kruskal Algorithm

Figure 4.73 illustrates the Feature Importance Scores using the Kruskal-Wallis Test, which is a non-parametric statistical method used for feature selection when data does not meet normality assumptions.

Different techniques have different opinions about our data; however, all techniques recommend data optimization.

5 DISCUSSION

The literature demonstrated in the references was intuitive for the research due to the possibility observed to measure complex structures, for example:

The paper "A Study of FMCW Radar for the Detection of Water Level Inside a Wine Jar" by Min Wang et al. explores the application of Frequency-Modulated Continuous-Wave (FMCW) radar technology for non-invasively measuring the liquid level in wine jars sealed with wooden lids, thereby eliminating the need for manual inspection or contact-based sensors. The study presents a detailed electromagnetic model of wave interactions with the layered structure comprising air, wood, and wine, focusing on signal reflection, transmission loss, and attenuation characteristics. Simulation results indicate that although higher-frequency components (>100 MHz) suffer noticeable attenuation within the wine medium (approximately 3 dB), the wooden lid contributes only minor signal loss (~0.08 dB), supporting the radar's feasibility for this use case.

Also, Shi et al. propose the Golden-section-based Fast Fourier Transform (GFFT) algorithm to improve liquid level measurement accuracy in opaque industrial tanks using Frequency Modulated Continuous Wave (FMCW) radar. Traditional FFT-based methods suffer from issues like the "Picket Fence Effect" and signal interference from tank walls and surface ripples, which limit precision. GFFT addresses these by applying golden section search to refine peak detection within the FFT spectrum, achieving sub-bin resolution with minimal computational cost. Simulations and experimental results—using water as the test liquid—demonstrate that GFFT delivers accuracy near the Cramer-Rao Lower Bound, even in low Signal-to-Noise Ratio environments. It consistently outperforms established algorithms such as Quinn, MacLeod, and Candan. Field tests with a Texas Instruments IWR6843ISK radar and MATLAB-based signal processing confirm the algorithm's ability to achieve millimeter-level precision. These results suggest GFFT is a strong candidate for practical deployment in industries that require accurate, non-invasive level sensing, including chemical processing, wastewater treatment, and the monitoring of hazardous fluids.

In addition to the paper *"River Surface Analysis and Characterization Using FMCW Radar"* investigates the use of frequency-modulated continuous-wave (FMCW) radar for real-time, non-contact monitoring of river surfaces to improve flood and drought forecasting. A 76–81 GHz commercial FMCW radar is employed to measure water surface velocity and level using chirp sequence modulation and 2D fast Fourier transform (2D-FFT) to produce range-Doppler maps. The study introduces an innovative envelope velocity distribution method that extracts key features such as maximum mean velocity and peak width to analyze river flow characteristics. To improve signal clarity, the approach applies zero-velocity blanking and constant false alarm rate (CFAR) filtering, followed by time-averaging of envelope velocities to identify dominant reflection zones. The system distinguishes between smooth and turbulent flows and corrects radial velocity measurements using geometric adjustments. Field tests conducted on four rivers in Southern Germany validate the radar's effectiveness in classifying flow regimes and identifying environmental artifacts, such as reflections from stationary objects like branches. The findings demonstrate FMCW radar's promise for continuous hydrological monitoring and early warning systems, offering a robust, contact-free solution capable of operating under varying environmental conditions.

Also, the paper *"Radar Sensors (24 and 80 GHz Range) for Level Measurement in Industrial Processes,"* Vogt (2018) presents a detailed comparison of FMCW radar systems operating at 24 GHz and 80 GHz for monitoring liquid and bulk solid levels. The study highlights how material properties—such as permittivity, conductivity, and surface roughness—affect signal reflection, scattering, and attenuation, influencing sensor performance. Through theory and field experiments, the paper demonstrates that 80 GHz radar offers superior resolution, narrower beamwidths, and better signal clarity, especially in cluttered environments like tanks or silos. However, it cautions that in dusty or foggy settings, 24 GHz may perform more reliably due to less Rayleigh scattering. The research also compares antenna and RF front-end designs, noting that 80 GHz systems, though more compact and bandwidth-rich, require fixed lens antennas, limiting flexibility. Ultimately, the paper concludes that sensor selection should depend on specific environmental and material conditions, despite the general advantages of 80 GHz systems.

Finally, the paper *"High Precision Water Level Gauge with an FMCW Radar under Limited Bandwidth"* by Yukinobu Tokieda *et al.* introduces a radar-based solution for accurate water level measurement, overcoming strict bandwidth limits imposed by license-free radio regulations in Japan. These regulations cap bandwidth at 76 MHz, limiting theoretical range resolution to 197 cm—far from the centimeter-level precision required in practice. To address this, the authors designed an FMCW radar system operating at 24.15 GHz and 75 MHz bandwidth, incorporating innovative hardware and signal processing techniques to suppress key disturbances: multiple reflections, image frequency, and latent noise. Their design employs separate horn antennas to reduce reflections, a quadrature detector to eliminate image frequency, and switchable RF amplifiers to mitigate noise. Signal processing includes noise filtering, IQ imbalance correction, sub-resolution smoothing, and FFT-based frequency estimation. Experimental results show that the system maintains error margins below 3 cm for ranges under 4 meters and under 1 cm for longer distances. Field tests in a pool confirmed ±3 cm precision, demonstrating strong performance even under real-world conditions. The radar achieves 1.5% of the theoretical resolution limit, making it viable for applications in river monitoring and disaster prevention. Minor measurement discontinuities remain a subject for further investigation.

The results align with previous studies on FMCW radar applications for liquid level measurement and material characterization. Similar to works by Min Wang et al. and Vogt, this study demonstrates that dielectric contrasts between liquids significantly influence radar signal reflections, enabling accurate detection of multi-layer systems. The observed phase shifts and amplitude variations in radar signals corroborate theoretical predictions and simulation outputs, reinforcing the validity of the proposed approach.

MATLAB and CST simulations provided a strong theoretical foundation, predicting clear phase changes corresponding to water contamination levels. Laboratory measurements confirmed these predictions, with FMCW radar successfully distinguishing between pure diesel and contaminated states even at millimeter-scale water layers. While minor discrepancies were noted between simulation and experimental data, attributable to environmental noise and hardware limitations—the overall trend remained consistent, validating the robustness of the model.

The application of machine learning significantly enhanced detection capabilities. Classification models achieved near-perfect accuracy in identifying contamination states, while regression models demonstrated strong predictive performance for estimating water and diesel levels. These results indicate that combining FMCW radar with AI-driven analytics can transform traditional fuel monitoring systems into intelligent, automated solutions. Furthermore, successful data reduction experiments suggest that high accuracy can be maintained with fewer predictors, reducing computational complexity and improving scalability.

The study's outcomes have substantial industrial relevance. FMCW radar offers a non-contact, real-time monitoring solution that mitigates safety risks associated with invasive sensors in flammable environments. Its ability to detect contamination early can prevent corrosion, fuel degradation, and engine damage, reducing maintenance costs and enhancing operational reliability. These advantages position FMCW radar as a viable alternative to conventional methods, which often lack precision or fail under harsh conditions.

Despite promising results, certain challenges remain. Multipath reflections within metallic tanks, temperature-induced dielectric variations, and hardware calibration issues can affect measurement accuracy. Addressing these factors through advanced signal processing, environmental compensation algorithms, and optimized antenna design will be critical for real-world deployment.

6 CONCLUSIONS

The study was successful to utilize the analogy between practically implemented measuring techniques and the proposed model and approach.

The successful completion of this research confirms the viability and precision of using Frequency-Modulated Continuous Wave (FMCW) radar technology for detecting water contamination in diesel storage tanks. Through comprehensive modeling, simulation, and experimental validation, the study demonstrated that FMCW radar can effectively distinguish between diesel and water layers based on their distinct electromagnetic properties, such as dielectric constant and signal attenuation. By analyzing the phase shift and amplitude of reflected radar signals, even small volumes of water contamination—introduced at millimeter-scale increments—were detectable with high precision. The use of multi-layer modeling (air, diesel, water, and tank wall) allowed for realistic simulation environments, and signal processing techniques like phase unwrapping and matched filtering further enhanced the system's sensitivity and resolution. Practical implications include the potential to replace manual or invasive level-sensing techniques with a non-contact, real-time monitoring solution that is robust to tank geometry, surface disturbances, and contamination levels. The system's capability to operate in high-frequency bands also ensures minimal interference and superior range resolution, critical for industrial fuel management. Moreover, by identifying even thin water layers that accumulate over time, the technology helps prevent corrosion, fuel degradation, and engine failure—ultimately contributing to improved operational safety and reduced maintenance costs. Overall, this research lays the groundwork for deploying FMCW radar as a cost-effective, dependable, and scalable solution for fuel quality monitoring in both stationery and mobile storage environments. Future work could involve integrating machine learning algorithms for automated contamination classification and extending the system for use with other fluid combinations or under varying environmental conditions.

For Future Work, we can consider the following points as proposed opportunities.

1. Integration with IoT and Cloud Platforms: Develop a fully automated monitoring system by integrating FMCW radar with IoT-enabled sensors and cloud-based analytics. This would allow real-time contamination alerts, remote diagnostics, and predictive maintenance for industrial fuel storage systems.

2. Miniaturization and Cost Optimization: Focus on reducing the size and cost of FMCW radar hardware to make the solution commercially viable for widespread deployment in automotive, marine, and industrial sectors. Leveraging low-cost RF components and system-on-chip designs can accelerate adoption.

3. Multi-Fuel and Multi-Contaminant Detection: Extend the radar-based detection approach to other fuels (e.g., gasoline, biofuels) and contaminants (e.g., sediments, chemical impurities). This requires refining dielectric models and calibration algorithms for diverse fluid properties.

4. Advanced Signal Processing Techniques: Implement enhanced algorithms such as Golden-Section FFT, adaptive filtering, and clutter suppression to improve accuracy

under challenging conditions like tank geometry variations, turbulence, and multipath reflections.

5. Machine Learning Model Deployment: Transition from offline MATLAB-based models to embedded AI systems capable of real-time classification and regression. Explore lightweight neural networks and edge computing for on-device processing.

6. Robustness Under Environmental Variations: Conduct long-term field tests to evaluate system performance under varying temperature, pressure, and humidity conditions. Develop compensation mechanisms for dielectric property changes due to environmental factors.

7. Safety and Compliance Enhancements: Design radar systems that meet ATEX/Explosion-Proof standards for hazardous environments. Future work should also include electromagnetic compatibility (EMC) testing and certification for industrial deployment.

8. Hybrid Sensing Approaches: Investigate combining FMCW radar with other sensing technologies (e.g., ultrasonic, capacitive, or optical sensors) to create redundant systems that enhance reliability and accuracy.

9. Data Optimization and Feature Engineering: Explore advanced feature selection and dimensionality reduction techniques to maintain high model accuracy with minimal data, reducing computational load and improving scalability.

10. Commercial Prototyping and Pilot Deployment: Develop a prototype for real-world testing in fuel stations, marine vessels, and industrial tanks. Collect operational data to refine algorithms and validate performance under practical conditions.

Finally, the study showed the feasibility of not only detecting one liquid below the other but paved the way for an Industrial solution to solve critical and frequently occurring problems within the Oil & Gas industry as well as domestic and commercial vehicles running on liquid fossil.

7 REFERENCES

Abouzaid, S., Jaeschke, T., Barowski, J., & Pohl, N. (2022). Deep Learning-Based Material Characterization Using FMCW Radar With Open-Set Recognition Technique. *2022 24th International Microwave and Radar Conference, MIKON 2022*. https://doi.org/10.23919/mikon54314.2022.9924681

Anitori, L., De Jong, A., & Nennie, F. (2009). FMCW radar for life-sign detection. *IEEE National Radar Conference - Proceedings*. https://doi.org/10.1109/RADAR.2009.4976934

Baer, C., Jaeschke, T., Pohl, N., & Musch, T. (2015). Contactless Detection of State Parameter Fluctuations of Gaseous Media Based on an mm-Wave FMCW Radar. *IEEE Transactions on Instrumentation and Measurement*, *64*(4), 865–872. https://doi.org/10.1109/TIM.2014.2374696

Barowski, J., Zimmermanns, M., & Rolfes, I. (2018). Millimeter-Wave Characterization of Dielectric Materials Using Calibrated FMCW Transceivers. *IEEE Transactions on Microwave Theory and Techniques*, *66*(8), 3683–3689. https://doi.org/10.1109/TMTT.2018.2854180

Bordoloi, S., Singh, B., Dhakal, R., & Dutta, S. (2017, September 27). Ranging and SAR Imaging of underground targets using Laptop based FMCW RADAR. *2016 International Conference on Circuits, Controls, Communications and Computing, I4C 2016*. https://doi.org/10.1109/CIMCA.2016.8053254

Burr, R., Schartel, M., Grathwohl, A., Mayer, W., Walter, T., & Waldschmidt, C. (2022). UAV-Borne FMCW InSAR for Focusing Buried Objects. *IEEE Geoscience and Remote Sensing Letters*, *19*. https://doi.org/10.1109/LGRS.2021.3094165

Charvat, G. L., Kempel, L. C., Rothwell, E. J., Coleman, C. M., & Mokole, E. L. (2010). A Through-Dielectric Radar Imaging System. *IEEE Transactions on Antennas and Propagation*, *58*(8), 2594–2603. https://doi.org/10.1109/TAP.2010.2050424

Cho, Y. S., & Cho, S. H. (2014). A design of the frequency modulated continuous wave (FMCW) radar system. *Proceedings of the International Symposium on Consumer Electronics, ISCE*. https://doi.org/10.1109/ISCE.2014.6884519

Christian M. Schmid, C. P. R. F. A. S. (2013). *An FMCW MIMO Radar Calibration and Mutual Coupling Compensation Approach*. IEEE European Radar Conference.

Du, Y., Cao, X., Yang, Y., Zhang, T., Yuan, J., Cui, T., & Yao, J. (2024). Acoustic Signal Reconstruction Across Water–Air Interface Through Millimeter-Wave Radar Micro-Vibration Detection. *Journal of Marine Science and Engineering*, *12*(11). https://doi.org/10.3390/jmse12111989

Eugin Hyun, Young-Seok Jin, & Jonghun Lee. (2014). *Development of 24GHz FMCW Level Measurement Radar System*. IEEE Radar Conference : from sensing to information : conference program.

Gromek, D., Samczyński, P., Wielgo, M., Malanowski, M., & Kulpa, K. (2016). Design and validation tests for compact FMCW C-band Analog-Front-End for radar imaging applications. *International Journal of Microwave and Wireless Technologies*, *8*(6), 845–854. https://doi.org/10.1017/S1759078716000623

Grosch, T. (2017). Correcting nonlinear modulation error in linear FMCW radar systems. *2017 IEEE Radar Conference, RadarConf 2017*, 1577–1581. https://doi.org/10.1109/RADAR.2017.7944459

Hegazy, A. M., Alizadeh, M., Samir, A., Basha, M., & Safavi-Naeini, S. (2023). Remote Material Characterization with Complex Baseband FMCW Radar Sensors. In *Progress In Electromagnetics Research* (Vol. 177).

Hwang, J. H., & Kim, D. J. (2020). Sea Surface Imaging with a Shortened Delayed-Dechirp Process of Airborne FMCW SAR for Ocean Monitoring on Emergency. *Sensors (Switzerland)*, *20*(24), 1–16. https://doi.org/10.3390/s20247310

Irmak, G., Sapmaz, E., Kocakuşak, A., & Helhel, S. (2025). DETERMINATION OF OLIVE OIL PURITY BY S PARAMETER. *Mühendislik Bilimleri ve Tasarım Dergisi*, *13*(1), 177–184. https://doi.org/10.21923/jesd.1483272

Jeong, H., & Kim, S. (2021). Educational low-cost c-band fmcw radar system comprising commercial off-the-shelf components for indoor through-wall object detection. *Electronics (Switzerland)*, *10*(22). https://doi.org/10.3390/electronics10222758

Kim, P. (2017). MATLAB Deep Learning. In *MATLAB Deep Learning*. Apress. https://doi.org/10.1007/978-1-4842-2845-6

Li, L., Yu, J., & Krolik, J. (2010). Software-defined calibration for FMCW phased-array radar. *IEEE National Radar Conference - Proceedings*, 877–881. https://doi.org/10.1109/RADAR.2010.5494498

Liang, H., & He, Z. (2009). Study on Signal Processing of FMCW Ground Penetrating Radar. *2009 International Conference on Measuring Technology and Mechatronics Automation, ICMTMA 2009*, *1*, 528–531. https://doi.org/10.1109/ICMTMA.2009.285

M. Vogt. (2018). *Radar Sensors (24 and 80 GHz Range) for Level Measurement in Industrial Processes*.

Ma, M. E., Li, Y., Jiang, X., & Huang, X. (2020, September 20). Hydrological Information Measurement Using an MM-Wave FMCW Radar. *2020*

International Conference on Microwave and Millimeter Wave Technology, ICMMT 2020 - Proceedings. https://doi.org/10.1109/ICMMT49418.2020.9386510

MacAsero, J. M. S., Gerasta, O. J. L., Pongcol, D. P., Ylaya, V. J. V., & Caberos, A. B. (2018, July 2). Underground Target Objects Detection Simulation Using FMCW Radar with SDR Platform. *2018 IEEE 10th International Conference on Humanoid, Nanotechnology, Information Technology, Communication and Control, Environment and Management, HNICEM 2018*. https://doi.org/10.1109/HNICEM.2018.8666248

Menguc, E., Kocakusak, A., Sapmaz, E., Irmak, G., & Helhel, S. (2025). Corrosion mapping of the surface of metal plates using FMCW radar. *Measurement: Journal of the International Measurement Confederation*, *253*. https://doi.org/10.1016/j.measurement.2025.117703

Micheli-Tzanakou, Evangelia. (2000). *Supervised and unsupervised pattern recognition : feature extraction and computational intelligence*. CRC Press.

Min Wang, Jinjie Yao, Yan Han, Rundong Jiang, Zhenni Liu, & Yahong Fan. (2012). *A Study of FMCW Radar For The Detection of Water Level Inside a Wine Jar*. College Publishing House.

Mun, J. M., Lee, J. H., Lee, S. C., Sim, K. D., & Kim, S. H. (2021). Performance evaluation of 80 GHz FMCW Radar for level measurement of cryogenic fluid. *Progress in Superconductivity and Cryogenics (PSAC)*, *23*(4), 56–60. https://doi.org/10.9714/psac.2021.23.4.056

Mutschler, M. A., Scharf, P. A., Rippl, P., Gessler, T., Walter, T., & Waldschmidt, C. (2022). River Surface Analysis and Characterization Using FMCW Radar. *IEEE Journal of Selected Topics in Applied Earth Observations and Remote Sensing*, *15*, 2493–2502. https://doi.org/10.1109/JSTARS.2022.3157469

Nashashibi, A. Y., Kashanianfard, M., & Sarabandi, K. (2022). Calibration of Wideband FMCW Polarimetric Radars Operating at Millimeter-Wave Frequencies. *IEEE Transactions on Geoscience and Remote Sensing*, *60*. https://doi.org/10.1109/TGRS.2021.3136484

Norouzi, Y., Jamaluddin, A. N., Abedi, F., & Shakir, A. M. (2022). Dual Band Signal for more precision in tank gauging radar. *IICETA 2022 - 5th International Conference on Engineering Technology and Its Applications*, 304–307. https://doi.org/10.1109/IICETA54559.2022.9888655

Nowak, A., Naus, K., & Maksimiuk, D. (2019). A Method of Fast and Simultaneous Calibration of Many Mobile FMCW Radars Operating in a Network Anti-Drone System. *Remote Sensing*, *11*(22). https://doi.org/10.3390/rs11222617

Părăian, M., Ghicioi, E., Vătavu, N., Gabor, D., & Mangu, S. I. (2021). The risk of static electricity at handling diesel fuel. *MATEC Web of Conferences*, *343*, 10013. https://doi.org/10.1051/matecconf/202134310013

Passafiume, M., Rojhani, N., Collodi, G., & Cidronali, A. (2021). Modeling Small UAV Micro-Doppler Signature Using Millimeter-Wave FMCW Radar. *Electronics (Switzerland)*, *10*(6), 1–16. https://doi.org/10.3390/electronics10060747

Schenkel, F., Schultze, T., Baer, C., Rolfes, I., & Schulz, C. (2024). Smoke Detection and Combustion Analysis Using Millimeter-Wave Radar Measurements. *IEEE MTT-S International Microwave Symposium Digest*, 887–890. https://doi.org/10.1109/IMS40175.2024.10600292

Shui, H., Geng, H., Li, Q., Du, L., & Du, Y. (2022). A Low-Power High-Accuracy Urban Waterlogging Depth Sensor Based on Millimeter-Wave FMCW Radar. *Sensors*, *22*(3). https://doi.org/10.3390/s22031236

Stove, A. G. (2004). *Modern FMCW Radar-Techniques and Applications*.

Tokieda, Y., Sugawara, H., Niimura, S., & Fujise, T. (2005). *High Precision Waterlevel Gauge with an FMCW Radar under Limited Bandwidth*.

Tushar Yuvaraj Gite, Pranav G Pradeep, & A. A. Bazil Raj. (2018). *Design and Evaluation of C-Band FMCW Radar System*.

Ulaby, F. T., & Jedlicka, R. P. (1984). Microwave Dielectric Properties of Plant Materials. *IEEE TRANSACTIONS ON GEOSCIENCE AND REMOTE SENSING*, *4*.

Vincenti Gatti, R., Cicioni, G., Spigarelli, A., Orecchini, G., Saltalippi, C., & Alimenti, F. (2024). A Dual-Mode FMCW-Doppler Radar With a Frequency Scanning Antenna for River Imaging Applications. *IEEE Access*, *12*, 86132–86143. https://doi.org/10.1109/ACCESS.2024.3414189

Yang, J., Thompson, J., Huang, X., Jin, T., & Zhou, Z. (2012). FMCW Radar Near Field Three- Dimensional Imaging. *IEEE International Conference on Communications*, 6353–6356. https://doi.org/10.1109/ICC.2012.6364681

Zhang, J., & Bai, R. (2011). A level measurement system of the FMCW radar based on virtual instruments. *Advanced Materials Research*, *171–172*, 337–341. https://doi.org/10.4028/www.scientific.net/AMR.171-172.337

Zhang, X., Shao, Z., Ren, J., Li, Y., & Jiang, J. (2018). DEVELOPMENT AND PRELIMINARY RESULTS OF SMALL-SIZE UAV-BORNE FMCW SAR. *International Geoscience and Remote Sensing Symposium (IGARSS)*, *2018-July*, 7825–7828. https://doi.org/10.1109/IGARSS.2018.8519235

Zhao Zeng-rong, & Qiu Yao-hui. (2014). *The Design of FMCW Radar Liquid Level Measuring System Based on FPGA*.

Zych, M. (n.d.). *Ground penetrating radar simulations of non-homogeneous soil with CST Studio Suite*.

CURRICULUM VITAE

Mohamed Sayed Abdelkhalek AFIFI

Education Information

PhD 2019-2025	Akdeniz University Institute of Science, Computer Engineering Department, Antalya
Master of Science (MSc) 2014-2018	Cairo University Electrical Power and Machines Engineering, Cairo
Bachelor (BSc) 2004-2009	Cairo University Electrical Power and Machines Engineering, Cairo

PROFESSIONAL AND ADMINISTRATIVE DUTIES

Global Industry Expert 2021-Continues	SCHNEIDER ELEKTRIK SAN VE TIC Global Connected Services Organization, İstanbul
Global Industry Expert 2013-2021	SCHNEIDER ELEKTRIK SAN VE TIC Global Connected Services Organization, Kahire, MISIR

WORKS

Articles published in international peer-reviewed journals.

1- AFIFI et al, " Performance Analysis of a Photovoltaics Module Placed Nearby Power Transmission Line " *International Journal of Sciences: Basic and Applied Research (IJSBAR)*

2- AFIFI et al, " Modeling of Detection of Water Contamination Located in Diesel Tanks Using Phase Change of FMCW Radar Signal "*International Journal of Sciences: Basic and Applied Research (IJSBA)*